



Università degli Studi di Padova

DIPARTIMENTO DI INGEGNERIA INDUSTRIALE

Corso di Laurea Magistrale in Ingegneria Elettrica

TESI DI LAUREA MAGISTRALE

AXIAL FLUX DEVICE FOR ELECTROMAGNETIC
CONVERSION/SUSPENSION APPLIED TO A FLYWHEEL SYSTEM

DISPOSITIVO A FLUSSO ASSIALE DI
CONVERSIONE/SOSPENSIONE ELETTROMAGNETICA PER
L'AZIONAMENTO DI UN VOLANO

Candidato:

Franco Bortot

Matricola 1034176

Relatore:

Prof. Andrea Tortella

Correlatore:

Prof. Mauro Andriollo

*Alla mia famiglia,
per il costante sostegno in questi anni di studio.*

Contents

Riassunto Esteso	i
Introduzione	i
Accumulo cinetico su grande scala	iii
Macchina sincrona lineare omopolare ed esempio applicativo	iv
Conclusioni	x
Abstract	1
1 Introduction	2
1.1 Overview	2
1.2 Grid Services	4
1.3 Hydraulic Storage	6
1.4 Compressed Air Energy Storage (CAES)	8
1.5 Uninterruptible Power Supply (UPS)	10
1.6 Cost Analysis	13
1.6.1 Flywheels as suppliers of Regulation Power	13
1.6.2 NaS Batteries	17
1.6.3 Generic Comparison	18
2 Flywheels	21
2.1 Flywheel Technology	21
2.2 Materials	24
2.3 Main Installations	27
3 Large Scale Kinetic Energy Storage (LSKES)	28
3.1 Acting Forces	28
3.2 Energy Density	29
4 Transverse Flux Homopolar Synchronous Machine	35
4.1 Overview	35
4.2 Flux Leakage	36

4.2.1	General Geometry	36
4.2.2	TFHSM Geometry	41
4.3	Analytical Design	46
5	Design Example	52
5.1	Overview	52
5.2	Materials	56
5.2.1	Magnetic Core	56
5.2.2	Permanent Magnets	57
5.3	Stator Module	60
5.3.1	Stator Layout Optimisation	62
5.4	Permanent Magnet and Slot Design	67
6	FE Analysis Verification	71
6.1	FEM Exterior Box Influence	71
6.2	No-load Results	74
6.2.1	Levitation Force dependence upon Angular Position	78
6.3	Stability	80
6.4	Cogging Torque	83
6.5	Machines Angular Shift	84
6.6	On-load results	89
6.6.1	Parameters Evaluation	89
6.6.2	Induced Voltage	90
6.6.3	Torque Calculation	92
	Conclusions	94
	References	96

Riassunto Esteso

Introduzione

Il lavoro di tesi qui svolto verte principalmente sull'accumulo di energia tramite volani, comprendendo dapprima una descrizione delle tecnologie presenti ed adottate principalmente per l'accumulo di energia su larga scala:

- Pompaggio idraulico;
- Stoccaggio di aria compressa (CAES);
- Batterie, fra le più comuni figurano: NaS, piombo acido, Li-ion;
- Volani.

Sebbene esistano molte altre soluzioni tecnologiche, il loro grado di maturità suggerisce di escluderle dal computo, perlomeno nell'ottica di un orizzonte temporale a breve-medio termine. Fra gli aspetti salienti emerge la difficoltà di comparazione fra le differenti tecnologie, dati i molteplici aspetti da considerare, come per esempio facilità di installazione, costo di installazione, efficienza nel ciclo carica/scarica, autoconsumi, velocità di risposta del sistema, costo di manutenzione, problemi relativi alla sicurezza.

I volani impiegati nelle applicazioni di energy storage sono tipicamente costruiti con fibre di carbonio che, nonostante la loro bassa densità, offrono resistenze a trazione fino a 2 GPa, quindi permettono alte velocità di rotazione del volano stesso. Essendo la quantità di energia immagazzinata (tab. I) legata linearmente con il momento d'inerzia e quadraticamente con la velocità rotazionale del volano, vi è interesse nella ricerca di materiali resistenti e contemporaneamente pesanti, sebbene ad ora i materiali più performanti siano le fibre di carbonio (resistenti ma relativamente leggere).

Accumulo cinetico su grande scala

L'aspetto principale che limita l'incremento di velocità rotazionale di un volano è rappresentato dal cedimento strutturale causato dagli sforzi centrifughi. All'aumentare della dimensione del volano, gli sforzi tangenziali atti a compensare l'effetto centrifugo tendono ad avere una componente radiale che diminuisce all'aumentare del raggio, come spiegato qualitativamente in fig. II.

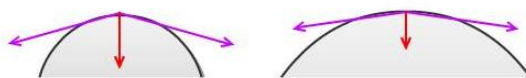


Figura II: Distribuzione degli sforzi tangenziali, all'aumentare del raggio.

La diretta conseguenza del fenomeno è che all'aumentare del raggio (per un determinato materiale), per non incorrere in rotture meccaniche, la velocità di rotazione deve diminuire. Sommando i due effetti si dimostra come la densità di energia nel materiale rimanga invariata. Una soluzione artificiale al problema consiste nell'introduzione di un circuito magnetico dedicato, atto a compensare la forza centrifuga. La figura III mostra una possibile configurazione del sistema: un tunnel a forma toroidale, con al suo interno del materiale rotante disposto in una serie di vagoni interconnessi, tenuto in levitazione e mosso dal circuito magnetico in alto (rosso), e contenuto radialmente dal circuito magnetico a sinistra (blu). Vi sarebbe inoltre un'importante riduzione nei consumi energetici dati dall'attrito viscoso qualora venissero adottate tecnologie per fornire un sufficiente livello di vuoto all'interno del tunnel.

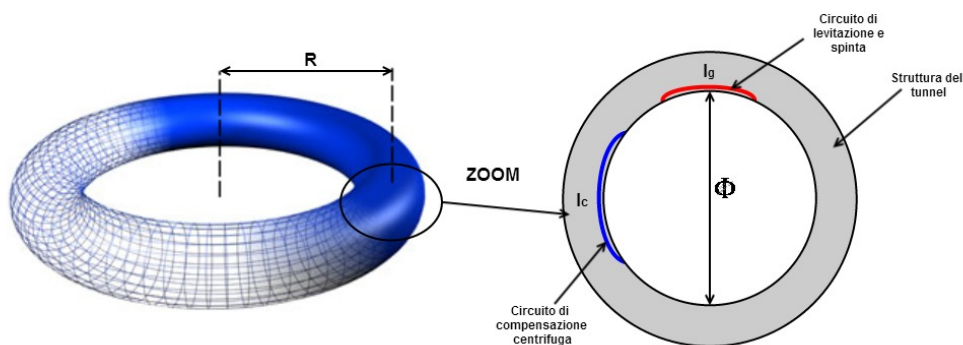


Figura III: Dettagli della soluzione proposta. A sinistra è presente una rappresentazione dei circuiti magnetici adottati.

In termini di densità energetica, valutazioni numeriche mostrano come un limite inferiore alla velocità possa essere fissato a 300 m/s, scegliendo quest'ultima come specifica di progetto. Data la velocità del materiale rotante, è possibile calcolare l'ammontare di pressione magnetica necessaria al contenimento centrifugo dei vagoni, e rapportarla alla superficie laterale disponibile del tunnel. Da ciò è possibile ottenere il valore d'induzione magnetica necessaria allo scopo e confrontarlo con valori normalmente presenti nelle macchine elettriche (0.5 - 1 T). A titolo esemplificativo, un esempio di progetto dove l'induzione magnetica è stata fissata ad 1 T e la velocità tangenziale a 300 m/s ha portato alle dimensioni del toro: $R = 3\text{km}$, $\Phi = 2\text{m}$, assumendo come materiale rotante acciaio con densità di 7800 kg/m^3 . In termini di costo specifico, il risultato più significativo è rappresentato dal costo per unità di energia immagazzinata, riguardo al solo materiale rotante. Infatti assumendo un costo specifico di 0.5 €/kg per l'acciaio, si ottengono 40 €/kWh . Il risultato appare interessante, perlomeno al livello di analisi adottato, in quanto in un'ottica di comparazione dei costi rispetto ad altre tecnologie permette un ampio margine economico per la costruzione di tutte le infrastrutture necessarie alla levitazione, il tunnel e i dispositivi per creare il vuoto. Come indice di confronto, le batterie piombo-acido hanno un costo per unità di energia stimabile in 120 €/kWh .

Alla luce dei potenziali benefici economici, rimangono tuttavia irrisolte una serie di sfide tecnologiche necessarie ad assicurare il corretto funzionamento della struttura, in primis la gestione attiva del traferro necessaria a provvedere la stabilità del materiale rotante ad una velocità così alta.

Macchina sincrona lineare omopolare ed esempio applicativo

Per l'azionamento di un volano è stata scelta una macchina sincrona lineare omopolare, con flusso trasverso prodotto da un magnete permanente. La geometria (fig. IV) permette di assolvere contestualmente due funzioni:

- Sospensione magnetica del volano, grazie alla forza attrattiva fra statore e rotore esercitata dal magnete permanente;
- Propulsione del rotore, grazie all'iniezione di un'opportuna terna di correnti trifase nell'avvolgimento di statore.

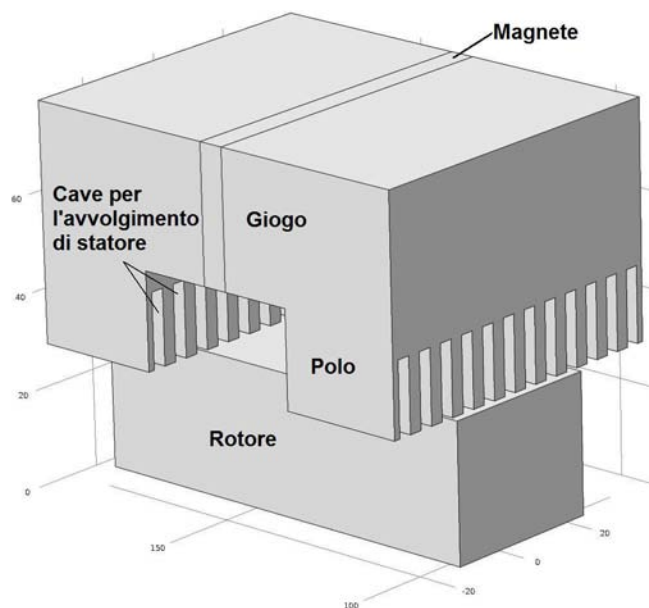


Figura IV: Geometria della macchina sincrona lineare omopolare, a flusso trasverso.

I vantaggi di tale configurazione possono essere riassunti in:

- Basse perdite rotoriche, dovute anche all'assenza di circuiti sul rotore stesso;
- Alto rendimento, tipico delle macchine sincrone;
- Modularità della geometria;
- Unica parte rotante composta da blocchetti di materiale ferromagnetico.

D'altro canto le macchine lineari soffrono di effetti di bordo, la configurazione omopolare prevede anche un basso sfruttamento del rame di statore, quindi un fattore di potenza ridotto. A causa dell'alta riluttanza del magnete i flussi di dispersione hanno un contributo non trascurabile, di conseguenza vari metodi sono stati adottati per contabilizzarne l'effetto. Data la tridimensionalità intrinseca della macchina, in sede di progetto si sono introdotte due sezioni bidimensionali semplificate implementate tramite codice agli elementi finiti. Esse hanno potuto fornire un'indicazione attendibile dell'importanza dei flussi di dispersione, in particolare riguardo alla porzione di flusso prodotto dal magnete che raggiunge il traferro. Sono quindi state implementate numerose simulazioni bidimensionali, al variare di coefficienti adimensionali rappresentativi della geometria, per

poi condensare i risultati tramite delle funzioni interpolanti. Nell'ottica di proporre una soluzione integrabile con prodotti esistenti, si è scelto di progettare un azionamento alternativo a quello attualmente implementato nei volani prodotti da Beacon Power di 4^a generazione. Tale sistema utilizza una macchina sincrona a flusso radiale, a magneti permanenti, in combinazione con cuscinetti magnetici ibridi (in parte costituiti da magneti, in parte da avvolgimenti controllati attivamente). Il tutto è mantenuto sotto condizioni di vuoto per ridurre le perdite energegiche prodotte dall'attrito viscoso.

La soluzione proposta (fig. V) consta invece di tre macchine principali, ognuna delle quali contenente una serie di macchine lineari sincrone omopolari, disposte su di una circonferenza. La parte ottagonale rossa rappresenta l'insieme degli statori, mentre i blocchetti magnetici di rotore sono calettati su di un'unica flangia e solidali col volano.

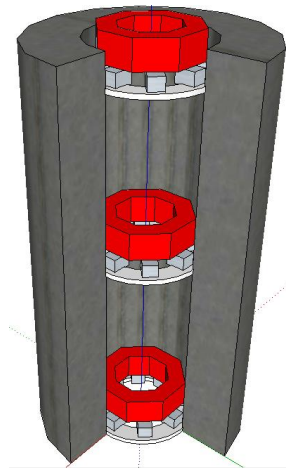


Figura V: Geometria dell'azionamento proposto.

Date le alte velocità di rotazione, per il circuito magnetico si è scelto un materiale in polvere (Soft Magnetic Composite), a cui viene impressa la geometria voluta tramite operazioni di stampaggio e riscaldamento. Fra le varie caratteristiche, rispetto ai lamierini, tali materiali permettono di contenere le perdite per isteresi e correnti parassite generate dalle alte frequenze delle grandezze in gioco. Un riassunto delle specifiche adottate per il progetto della macchina è contenuto in tab. II, dove si è assunto un ciclo di carica/scarica di 6 ore come riferimento.

Grandezza	Valore	Unità di misura
Forza di levitazione richiesta	10	kN
Velocità di rotazione minima	8000	rpm
Velocità di rotazione massima	16000	rpm
Numero di macchine	3	
Numero di statori per macchina	8	
Potenza richiesta	4.17	kW
Energia immagazzinata	25	kWh
Coppia in caso di velocità minima	5	Nm

Tabella II: Specifiche della macchina elettrica.

Essendo presenti vari gradi di libertà nella scelta della geometria di statore, si è adottato un approccio di ottimizzazione multi obiettivo che ha permesso di massimizzare l'area dei poli e contemporaneamente ridurre gli effetti di curvatura inevitabili dalla disposizione circonferenziale delle macchine. In fig. VI è rappresentato il risultato successivo all'ottimizzazione, una volta scelto il numero di statori per macchina $p=8$.

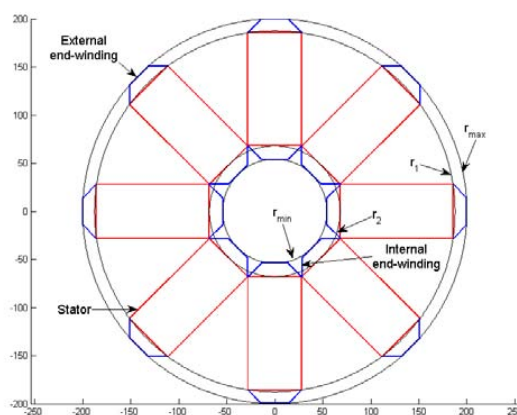


Figura VI: Vista dall'alto della disposizione statorica ottimizzata, nel caso di otto statori.

Come si può notare vi sono dei tratti angolari in cui un rotore, nel passare da uno statore al successivo, incontra una bassa superficie di accoppiamento con lo statore, portando ad un decremento delle performance medie. È stato quindi introdotto un coefficiente maggiorativo delle prestazioni basato sull'area media di accoppiamento fra statore e rotore (fig. VII).

I risultati dei principali studi parametrici sono riassunti nelle figure VIII - XI, dove si può notare un comportamento stabile della macchina

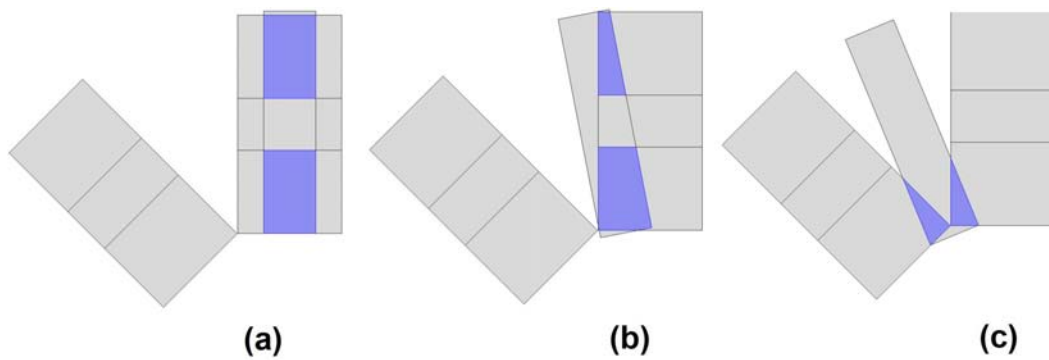


Figura VII: Vista dall'alto dell'area di accoppiamento, per differenti posizioni rotoriche.

per quanto riguarda sbilanciamenti lungo il piano ortogonale all'asse di rotazione (piano xy), mentre un controllo attivo del traferro è richiesto lungo l'asse verticale (asse z).

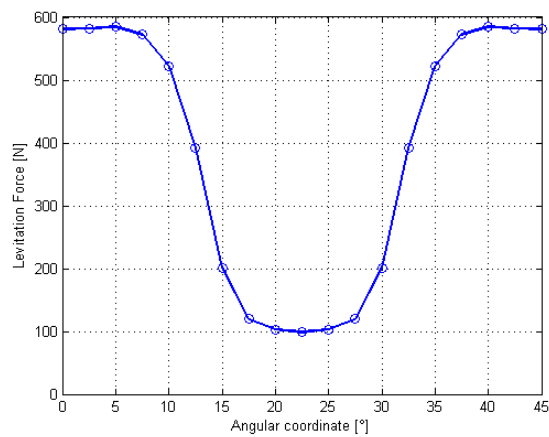


Figura VIII: Forza di levitazione al variare dell'angolo rotorico.

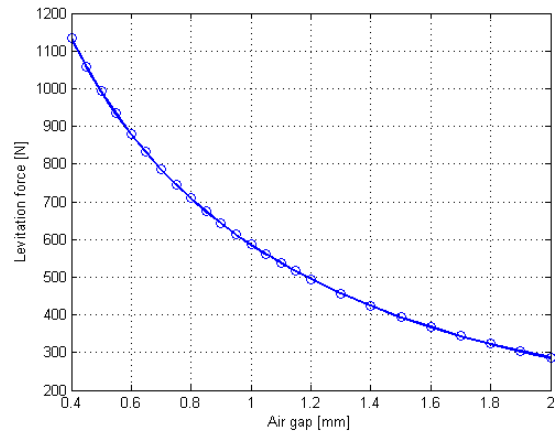


Figura IX: Forza di levitazione al variare del traferro.

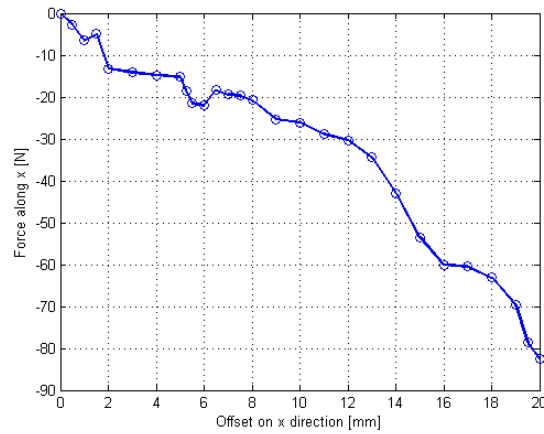


Figura X: Forza stabilizzante lungo x , in caso di decentrata. I valori si riferiscono ad un insieme di 8 statori e rotori.

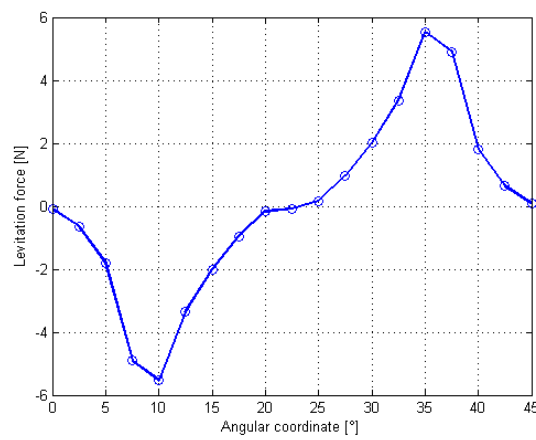


Figura XI: Coppia di impuntamento, al variare della posizione rotorica.

Riguardo ad un singolo rotore, i principali risultati numerici e una comparazione fra il metodo analitico adottato e il modello FEM 3D sono riassunti in tabella:

Grandezza	Metodo analitico	Metodo FEM 3D	Unità di misura
Forza di levitazione media	417	380	N
Coppia media	0.208	0.187	Nm
Flusso del magnete	1.73	1.65	mWb
Flusso al traferro	1.02	0.996	mWb

Tabella III: Comparazione fra i risultati dei due metodi considerati.

Come si può notare vi è in generale una tendenza del metodo analitico a fornire soluzioni che sovrastimano le performance, rispetto a quanto valutato più accuratamente tramite FEM. Va tuttavia specificato che il basso costo computazionale del metodo analitico lo rende preferibile in prima analisi, per poi correggere eventuali deviazioni rispetto alle specifiche tramite modifiche alla geometria e validazioni FEM.

Conclusioni

La macchina elettrica proposta è stata dimensionata e validata, riscontrando differenze fra stime analitiche e valutazioni FEM con errori contenuti all'interno del 15% per la maggior parte delle grandezze considerate. Il metodo proposto che comprende la valutazione di analisi FEM 2D semplificate ha mostrato la maggior congruenza con i risultati, rispetto ad altre metodologie esaminate (reti magnetiche). Le problematiche su cui focalizzare futuri studi comprendono la riduzione della coppia di cogging, la valutazione delle perdite per correnti parassite e isteresi magnetica, nonché un'analisi più approfondita dell'utilizzo del materiale magnetico, che può portare ad una geometria ad angoli smussati senza pregiudicarne le caratteristiche di permeabilità.

Abstract

In this work of thesis multiple aspect of energy storage technologies are discussed, focusing on kinetic energy storage by mean of flywheels. The first two chapters comprise a literature review, outlining state of the art technologies together with their major characteristics concerning costs, ease of siting, safety, efficiency, speed of response and maintenance issues.

The third chapter undertakes a feasibility analysis of a large scale kinetic energy storage (LSKES), showing cost advantages that may arise from an increased dimension of the system, together with technological challenges to be faced.

Finally, last chapters present a novel application of a transverse flux homopolar synchronous machine (TFHSM) on a flywheel energy storage system (FESS). Some of the characteristics of TFHSMs are well suited to the specifications required by an electric machine interfacing FESSs to the power grid. In particular, two functions may be embedded:

- accelerating/decelerating torque;
- upward levitation force, that would enable the flywheel to be completely magnetically suspended without the need of additional magnetic or mechanical bearings.

TFHSMs are already commercially employed, mainly in the case of low maintenance industrial movers or electric powered public transport. On the other hand flywheels are a proven technology that has been mainly used in the past for motion smoothing by mean of their inertia. However nowadays, thanks to the composite materials performance achievements, new applications in energy storage are becoming attractive. Despite their low density composite materials can bear mechanical stresses of approximately an order of magnitude higher than conventional metals, resulting in a theoretical stored energy density that is competitive with modern batteries.

Chapter 1

Introduction

1.1 Overview

In the past decade the interest for CO₂ emissions reduction and environmental issues in general had grown in importance, creating the spark that allowed renewable energy sources to enter the scene of global energy production. Concentrating on the electricity production, the only form of renewable energy that has been exploited on a large scale for many years is the hydroelectric one. Most of such power plants are composed by a dam that allows energy storage and thus power delivery regulation.

By way of contrast, emerging technologies such as wind turbines and photovoltaic are inherently intermittent and only partially predictable [1, 2, 3, 4]. As a consequence, if we assume an increase in power production over the years to come by intermittent renewable energy sources (IRESs), the grid stability will become of concern [5, 6].

There are basically two ways of facing the spread between the demanded and the produced power:

- Power modulation of both conventional power plants and renewable energy sources allowing for regulated generation;
- Energy storage, near the IRESs plants and close to the main centres of consumption as well.

The former solution is the simplest to implement, at least while adequate energy storage facilities aren't available. However, it raises operating issues for conventional plants, mainly due to the fact that they've been designed and built assuming a constant power output. As power output changes significantly and quickly, steam cycle components such as heat exchangers are thermally overstressed with respect to their rated operation.

An estimate of the life-expectancy reduction of power plants that could be caused by these stresses has been made by [7], even though it is clear that this is an important risk conventional power plants operators are implicitly bearing due to the energy free market and growing shares of IRESs. This, together with the efficiency reduction that occurs for power outputs lower than the nominal rating, opens new possibilities for energy storage on a large scale.

At the moment, the latter solution is worldwide led by hydraulic storage [8], that accounts for more than 100 GW of installed power and more than 99% of the market [9]. However some intrinsic aspects of the technology may be of limitation for certain purposes. For example, it cannot be installed on flat zones, where cities that need energy storage can be located. Wide extension power lines from mountains to cities can mitigate the problem, but only partially as they introduce losses, stability margin reduction and construction disapproval from interested population. Another limitation is the delivery of high power ancillary services, if required in locations where hydraulic storage is not feasible. Concerning this aspect, fig. 1 shows that not all the kinds of power plants are suitable for grid services requiring high speed of response, and even though hydro power plants have quicker response than other thermal ones, they still result to be excessively slow for some specific purposes. On a grid perspective, it must

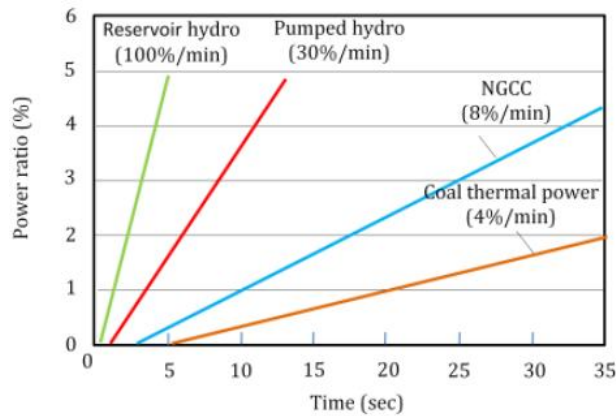


Figure 1: Comparison of the adjustable load rates of four power plants. [8]

be pointed out that according to Mazzocchi et al. [10], small dimension distributed electrical generators tend to lack in provision of spinning reserve, and this can be compensated only through appropriately programmed inverters connected to energy storage devices.

1.2 Grid Services

Energy storage has multiple functions that can be classified by mean of the average time involved in the function delivery. An overall representation

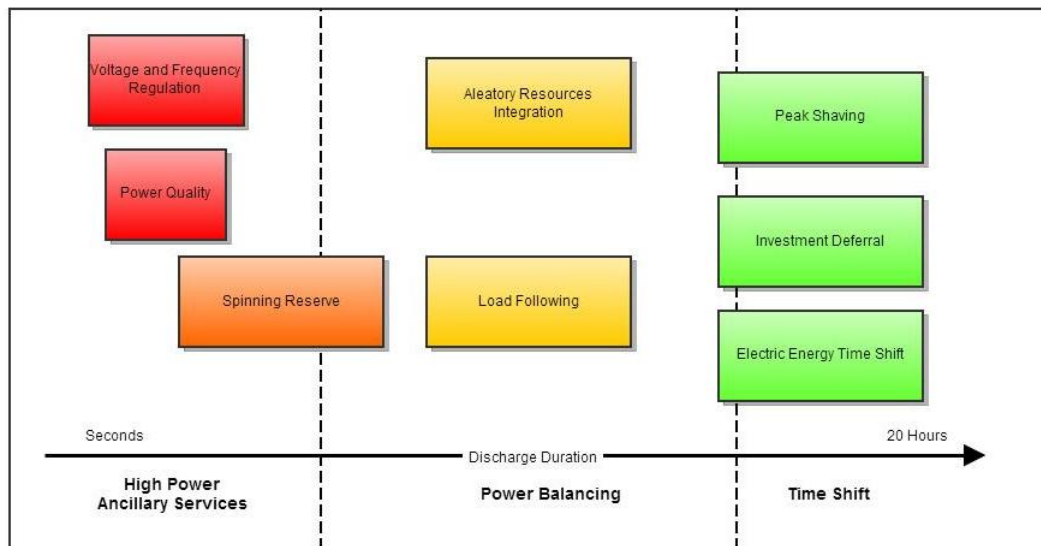


Figure 2: Classification of main applications of energy storage on a time basis. [10]

of the services that are required for a proper and optimized working grid are expressed by fig. 2, including services that are likely to be heavily augmented in the years to come, as the ones laying on the right side of the scheme. More precisely, a detailed description of each function comprises:

- **Time Shift** - Use of systems in order to delay the electric energy consumption. Its typical time span is 1 to 10 hours. It must be pointed out that thanks to the price difference of electricity from day to night, energy storage devices that can perform time shift may become attractive on a trading perspective (so called *Energy Time Shift*). This has the advantage of lowering peak prices that occurs whenever the demand is critical with respect to the supply. Another point of view may be the TSO's one, who may be interested in avoiding the construction of new lines or potentiation of existing ones, as one demand zone becomes critical in only some periods of the whole day. It is commonly defined as *Investment Deferral*;
- **Power Balancing** - Use of energy storage with the goal to face both the demand curve (which has generally low price elasticity, thus on

the TSO perspective it is non-modifiable and unknown a priori), and the aleatory production curve of IRESs. Sub-applications as *Load Following* allows a better use of conventional power plants, as the spread between demand curve and IRESs production curve becomes more predictable;

- **High Power Ancillary Services** - It generally requires a response time lower than a second, which is crucial for short term grid stability. Ancillary services are a wide family of grid capabilities that are in charge of managing grid mismatch. For example, *Spinning Reserve* is usually delivered by the power plant generators, with the goal of keeping stable values of frequency as soon as a power interruption occurs. Batteries and other devices connected to the grid through an inverter can help performing the task, with the advantageous possibility of installation directly on the critical zone. On the other side, *Power Quality* is gaining importance also due to the raising content of current harmonics generated by electronic devices.

The power regulations that every time are carried out in the grid, in order to constantly match demand and supply (including transmission losses), are divided into three sets. The reason behind the classification is related to the technology and infrastructure that performs it. For short term fluctua-

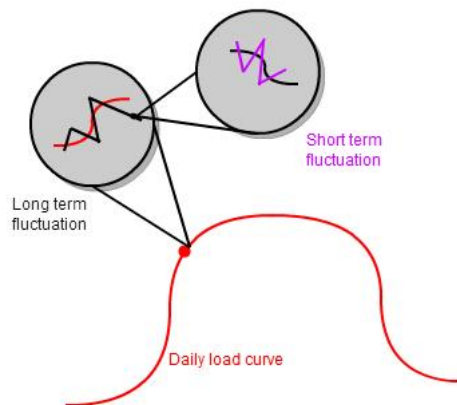


Figure 3: Components of a load curve. [8]

tions (up to some minutes), an automatic system also referred as primary regulation changes the power output in order to follow the request, but a variation in frequency occurs. For long term fluctuations (up to 30 minutes), secondary regulation has the duty to reset the grid frequency to the nominal value. Finally, the daily load curve is followed at most by mean

of an energy market called day-ahead market, where the demand for the day to come is forecasted together with IRESs contributions, and the energy supply is contracted among producers, big private consumers and publicly owned companies that aggregate small consumers. The traded energy contract has usually minimal duration of 1 hour.

1.3 Hydraulic Storage

Hydropower is one of the oldest ways to produce electricity, dating the first large scale applications at the end of 19th century. It can be seen in fig.

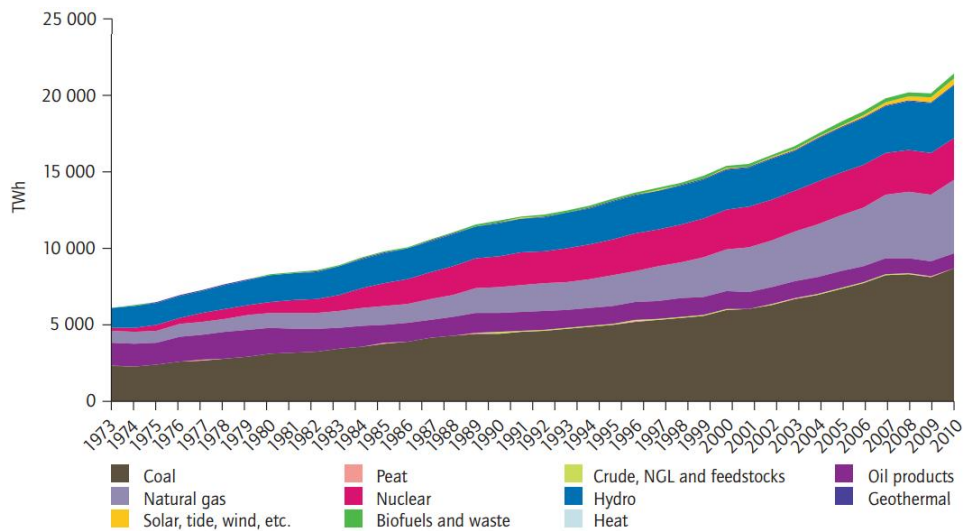


Figure 4: Global electricity generation by fuel, 1973-2010. [11]

4 that hydropower historically kept a slightly shrinking production share, with installations that grew less than proportionally to demand. Nevertheless, it still contributes to approx. 17% of global electricity production. However only a fraction of the total installed plants is capable of pumping, mainly because it requires additional investments or site features like a lower reservoir, ternary groups or reversible Francis turbines and electric equipment that performs variable speed operation. Despite its leader position in energy storage, it has some disadvantages that had limited new installations over the last decades, as seen in fig. 5, namely because of:

- **Environmental impact of reservoirs** - Concerns about phenomena as fragmentation of river ecosystems, reservoir sedimentation, river road and coastal erosion, changes in water temperature and oxygenation;

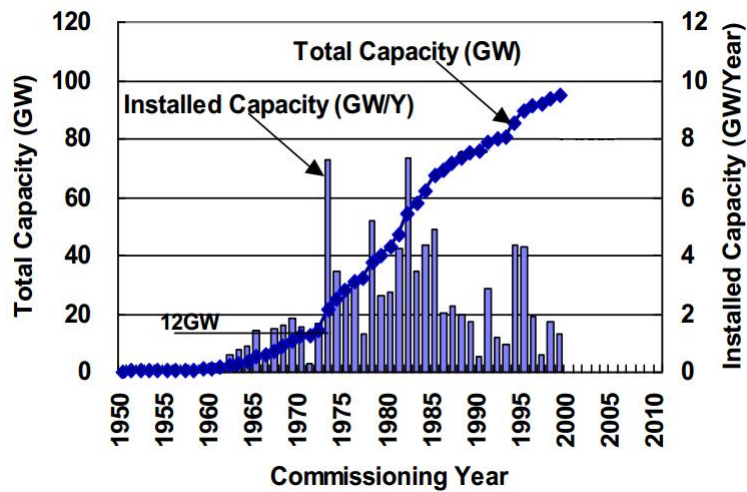


Figure 5: Pumped hydro trends. [8]

- **Risk** - Events in the past have already shown that disasters due to dam breakdown or landslide caused by geological instability and consequential overflow are possible. Because of this and the former point, social acceptance becomes crucial in successful projects, as in most large scale engineering constructions;
- **Suitable locations** - By the fact that installations increased in absolute terms, it is more difficult to find sites (technically referred as siting) that meet the requirements: geological stability, head (difference in water elevation between upper and lower reservoirs) and others of minor importance.

All the points are binding in different ways among various countries and continents, depending upon the amount already deployed of hydroelectric potential.

Costs are expected to be constant in the future, as the technology is completely mature: according to [8], a new installation would cost 2100 - 2600 €/kW, sub divided into dam (30%), channel (21%), generator (15%), civil engineering (9%) and balance of plant (25%).

Seawater applications may be an interesting solution where sufficiently steep shores are present [10], since they enable the construction of a single upper reservoir, exploiting the sea as lower reservoir. The 30 MW Yanbaru project in Okinawa (Japan) has been the first concept demonstration. Sea corrosion and its mitigation is estimated to raise plant costs of 15% [8] with respect of a benchmark freshwater plant.

1.4 Compressed Air Energy Storage (CAES)

Based on a reservoir of compressed air, CAES systems allow to store energy through compression and consequential (time deferred) expansion of air. There are mainly two classes of plants, fired CAES and unfired CAES. The distinction is due to the fact that during the compression phase, air increases its temperature, whereas during the expansion phase it tends to cool down, arising the problem of ice creation in the turbine. In order to cope with these aspects, heat can be stored during compression and then be given back to the air during expansion (diabatic CAES) or external heat may be provided by combustion of a fossil fuel, generally natural gas (diabatic, or fired, CAES). Most important layouts can be seen in fig. 6, where both diabatic and adiabatic configurations are featured.

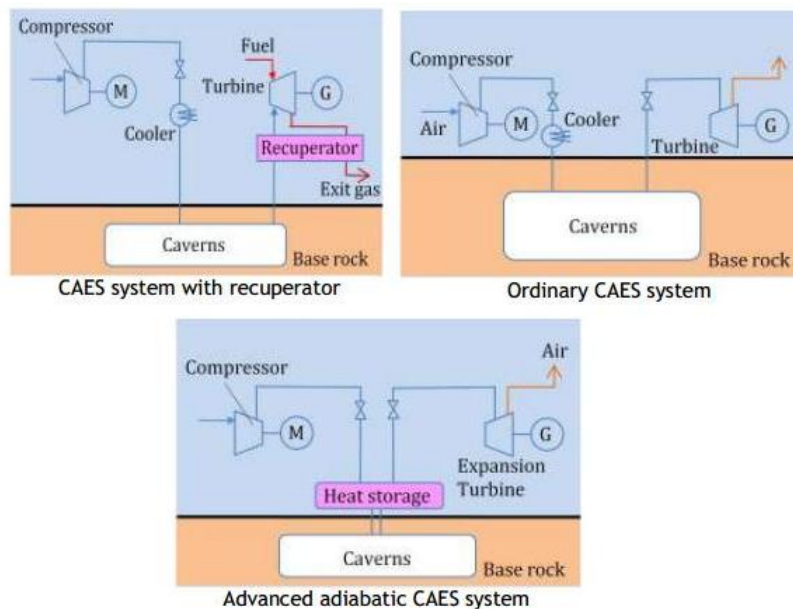


Figure 6: Different plant layouts. [8]

The most important installations are diabatic CAESs located in USA (McIntosh, Alabama, 110 MW) and Germany (Huntorf, 290 MW), both have been built decades ago (1991 and 1978 respectively) and rely on a cavern, operating at pressures in the range of 45 - 75 bar. Despite the low number of plants existing, reliability on the long term has been proved thanks to this two proof of concept sites [9].

A further distinction between aboveground and underground CAES refers to the way as air is stored. Underground CAES is the only one

that has been built on a large scale, up to now; aquifers and caverns are the preferred sites. Aboveground CAES attempts to free this technology from the adequate location constrain, opting for tanks (possibly supplied from other industries that have already reached maturity stage, such as Oil & Gas or technical gases). As a result, they can be installed wherever the grid requires energy storage, and generally permit also lower nominal power ratings (some MWs). Conversely, underground CAES shows cost advantages due to the tank avoidance.

Probably the most important drawback lays in the low efficiency, attaining an electrical efficiency (expressed as electric energy delivered over electric energy consumed) of 65% in case of adiabatic CAES and 75% in case of diabatic CAES coupled with CCGT. In terms of primary energy efficiency (electric energy delivered over total thermal energy consumed), adiabatic CAES reach up to 27% and diabatic CAES, in the best foreseeable layout as integrated with fossil fuel plants, 38% [9].

In the case of adiabatic CAES, the thermal energy storage becomes an issue, with various technologies available to meet this need. Mainly coming from the Concentrated Solar Power (CSP) sector, solutions range across water (up to 100°C, at ambient pressure), molten salts (150 - 550°C), diathermic oil (up to 400°C), blocks of concrete (up to 400°C).

Concerning costs, in case of diabatic CAES, a part of the variable cost component is directly linked with fuel price (generally natural gas), hence hardly predictable in the future. For an underground diabatic CAES, plant costs are estimated to be 1000 - 1250 €/kW, as far as 2200 €/kW for an aboveground adiabatic CAES. Life expectancy is projected to be comparable with pumped hydro plants (35 years), or in terms of operative cycles, higher than 13000 cycles. Already existing installations have empirically demonstrated the long-lasting performances of the technology.

1.5 Uninterruptible Power Supply (UPS)

Critical applications of electric energy such as data centres, banks and medical equipment require a continuous power delivery, despite a failure of the main grid. Moreover, sensible devices as the electronic ones must be fed with relatively high quality of power, i.e. a three phase voltage waveform close to the ideal isofrequency, iso-amplitude sinusoidal one. Figure 7 shows different sensibilities of electric devices to voltage drops.

Proper functioning of the appliances is reached through an approach that takes into account both devices sensibility and grid disturbances, because their combination allows an estimate of the yearly outages in the requested service. As it can be seen in fig. 8, most of the grid anomalies

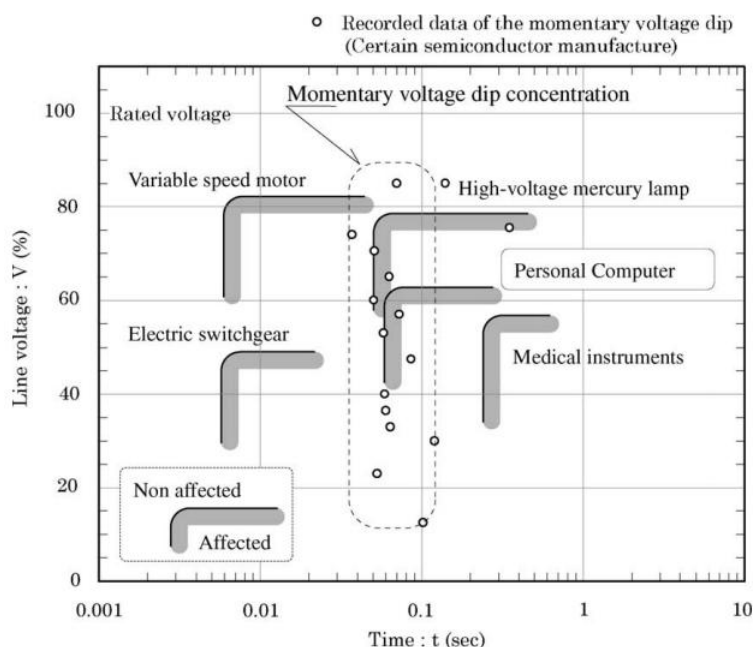


Figure 7: Electric devices affected areas by the momentary voltage drop. [12]

are concentrated in a range of few seconds, even if occasional long lasting interruptions would require a wider energy backup. Given the two charts it can be outlined the frequency of outages due to voltage drops, for a particular application: for example, if computers only must be fed by UPS, probably there is no such need to provide extremely quick response, at least with respect to others more sensible devices.

Power conditioning is a concept that is related to UPSs as most of the requirements by Power Quality can be delivered by a unique integrated system. An ideal UPS must face all the following issues at the same time:

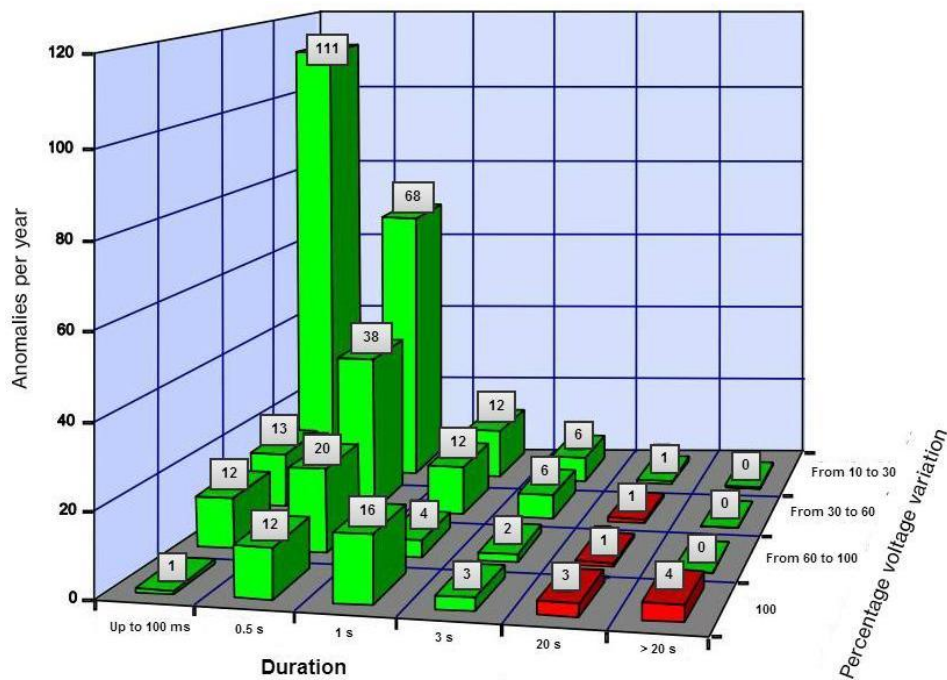


Figure 8: Statistics of anomalies on European MV grid. Source: UNIPEDE DISDI.

- Harmonics;
- Voltage spikes or sustained overvoltages;
- Voltage drops;
- Interruptions;
- Flicker;
- Imbalance between phases.

Manufacturers generally provide solutions that address many of the aforementioned points. The two major technologies used nowadays in the UPS field are batteries and flywheels (often referred as rotary UPSs). In addition, a distinction between online, line-interactive and stand-by configurations shall be made.

Stand-by layout is composed by a 2-ways switch that is, in normal operation mode, turned to feed the load through the mains. As soon as a fault is detected, the switch changes state and feeds the load through UPS. Switching time is generally contained under 25 ms.

On the other hand, line-interactive configuration adds an autotransformer between the grid and the switch, which allows to cope with continuous overvoltages or undervoltages, acting on the on load tap changer, instead of relying on the UPS.

Finally, online UPS allows a complete decoupling between grid and appliances. It is designed for being constantly in operation, converting the power from the grid to a DC bus (where the batteries or flywheel are connected) and then feeding the loads through an inverter. This is why it is also called double-conversion UPS. As a consequence, in case of an outage there is virtually no effect over the appliances, at the expenses of an increased initial investment (due to the higher number of components and their size, this kind of UPS is generally more expensive).

Concerning the two main energy storage technologies used in the UPS field, some characteristics of flywheels may result advantageous with respect to batteries, as well as others are penalizing. According to [34], pros of flywheels can be summarized as follows:

- No need of air conditioning in the energy storage room, nor temperature monitoring;
- No appreciable performance degradation over time;
- Expected life far higher;
- MTBF (Mean Time Between Failure) from 6 to 10 times higher;
- Higher crest factor (ratio between peak value over RMS value of current);
- High short circuit current, that enables sure intervention of protection devices (valid only for flywheels directly connected to the grid through an electrical machine);
- No influence of operating temperature over usable energy;
- Precision in the compute of available energy. When dealing with batteries, this estimate may be tricky and affected by many parameters.

Instead, drawbacks are:

- Need of diesel generator backup in order to face long lasting outages;
- Higher stand-by consumption;
- Noise and vibrations;
- Convenient only for high powers ratings.

1.6 Cost Analysis

This section aims to offer detailed cost comparison, even though a wide variety of factors is needed to be specified for each technology. Among all the energy storage solutions, flywheels and NaS batteries are examined more deeply than the others.

1.6.1 Flywheels as suppliers of Regulation Power

In order to evaluate costs and compare various technologies, some assumptions should be made. Since it is calculated the economic effort needed to provide a certain regulation power, a fixed amount of it has been chosen, comparing the NPV (Net Present Value) of the considered solutions [13]. By definition, the NPV consists of the sum of discounted cash flows involved in an investment: in this case it will account for plant costs, O&M costs (discounted at an appropriate discount rate, in order to obtain values that are present, instead of projected into the future) and any further cost related to the flywheel operation. Generally speaking, benefits of energy storage for regulation purposes can be summarised as follows, independently from the technology used to provide it:

- **Increase in peak and base load capability of the grid** - Assuming for simplicity a small grid consisting of a power plant, a line and a consumption centre, if energy storage is installed close to the latter there would be the possibility to use the line at a higher power rating all the time, as peaks are dispatched by the energy storage device;
- **Reduction of losses**, as regulation power contributes to power lines losses. This can be seen more clearly in the example figure 9, where a long term current component is shown, together with a summed zero-mean random signal to represent regulation current in the power line. By the fact that usually power lines operate at almost fixed voltage, a ripple in current means an equal ripple in power, given a constant power factor. In addition, the mean of the two waves is the same, thus overall the same amount of energy is dispatched. By squaring the RMS values of the two curves and integrating, a 3.6% higher figure is obtained in the case of long term + regulation component;
- **Reduced power line congestions**, as a consequence of the former points;
- **V-Q control**, thanks to the inverter capabilities (if the energy storage technology calls for it);

- **Contribution to 'Black Start' of conventional plants.** In case of a blackout, thermoelectric plants need external power to supply their auxiliary systems in the goal of bringing the grid back on-line, thus under this circumstances flywheel energy storage can effectively help the conventional plants to restart.

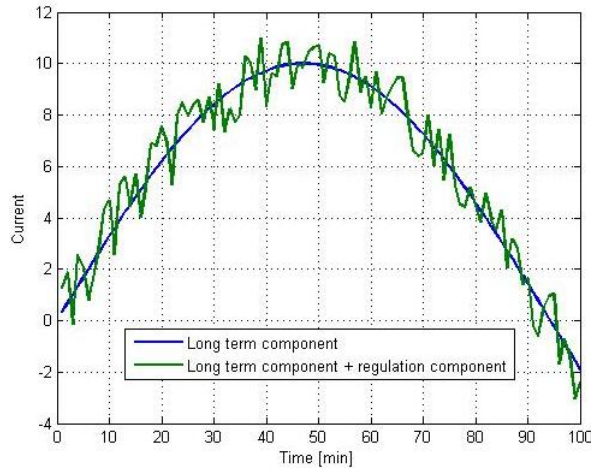


Figure 9: Long term component and regulation component.

A main distinction between energy applications and power applications is important, mainly because some technologies may result favorable for one use but too expensive for another one. For this purpose, [10] shows the suggestive table 1 describing the suitability of many technologies, depending over the grid service expected time duration. As flywheels appear to be conveniently viable only for short term applications (high power), this purposes are considered in the following treatise. Regulation life cycle costs have been calculated by [13], comprising the main alternative technologies. A particularity of this study is the inclusion of fossil fuel plants (that do not perform energy storage): it makes sense by the fact that under some assumptions such technologies may result with comparable costs with respect to storage. This is an important aspect of the overall energy storage issue: on a merely cost point of view, sometimes it is cheaper to produce the peak power through peaker plants (that generally have low initial plant costs but high operation and maintenance costs) than exploiting the reserve provided by energy storage. This condition only holds in particular cases, e.g. if the storage technology has particularly high costs and no CO₂ tax is charged, like today in the USA. Considering only a subset of the technologies mentioned before, under the hypotheses listed in tables 2 and 3, the study results are presented.

Technology	Time Shift	Power Balancing	Power Ancillary Services
Hydraulic CAES	✓	?	X
Sodium-Sulfur batteries	✓	✓	?
Sodium-Nickel chloride batteries	✓	✓	?
Li-ion batteries	✓	✓	✓
Ni-Cd batteries	✓	✓	✓
Ni-MH batteries	✓	✓	?
Pb acid batteries	✓	✓	?
Flow batteries	✓	✓	?
Flywheels	X	?	✓
SMESs	X	X	✓
Supercapacitors	X	X	✓

Table 1: Energy storage technologies and their best use. X represents unsuitability, ✓ represents suitability, ? represents uncertainty. [10]

In addition, it has been hypothesized a complete substitution of the lead acid batteries every 7 years. No forecast over electric energy and fuel price trend nor increase in maintenance costs has been made, assuming as valid the figures evaluated for the first year of study. Concerning the batteries, a roundtrip efficiency of 90.25% (95% per semi-cycle) has been assumed, together with a 20% DOD (Depth Of Discharge) nominal cycle. An advantage that could lower the cost related to inverter-based technologies is represented by their fast response time. More specifically, the authors of [13] outline how often happens that the traditional regulation (performed through power plants electric generators) shows to be excessively slow, resulting in regulation power that is against the current demand. For example, an injection of power even though the demand increased some minutes ago, but now has shrank. As a consequence, they introduce an X factor in order to account for the upgraded capabilities that flywheels and batteries would lead. Even if it has still to be deeply investigated, a estimate is $X = 2$, i.e. at installed power parity, inverted-based technologies deliver twice the service.

Item	Expression/Value
Regulation power	20 MW
Number of cycles per year	8760
Evaluation time frame	30 years
Yearly Maintenance	Lead acid: 2% of installation cost Flywheels: 11.6 USD/kW + 1.2 MWh/(MW*day) of losses Fossil fuel plants: +0.5% of regular maintenance
Increased fuel consumption allocated to regulation	Fossil fuel plants only: 2.7% - 3.7%
CO ₂ tax	17 USD/ton

Table 2: Main assumptions included in [13]. First part.

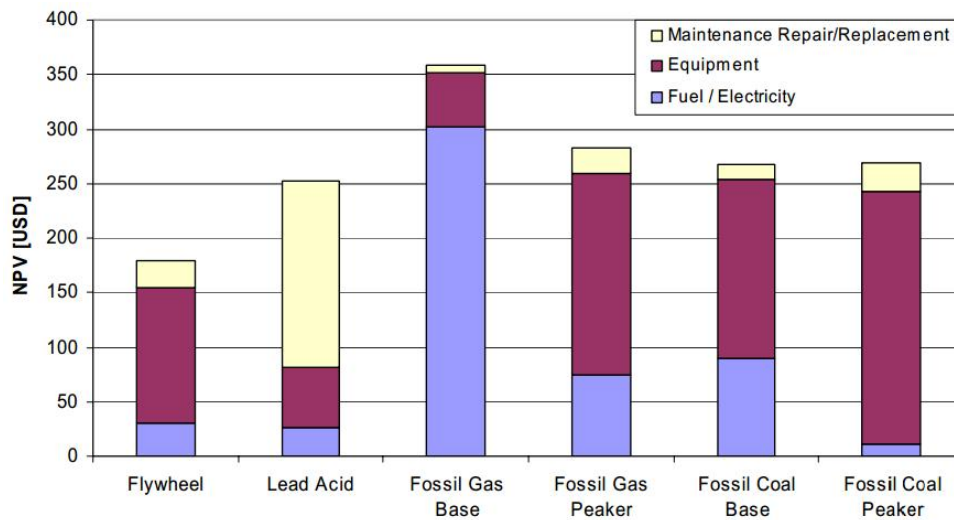


Figure 10: NPV hourly cost comparison. [13]

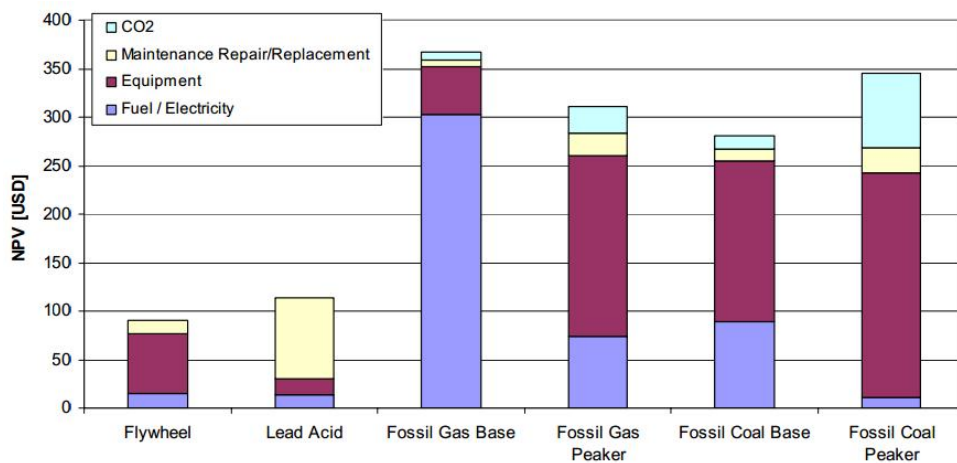


Figure 11: NPV hourly cost comparison including CO₂ and an X factor equal to 2. [13]

Item	Expression/Value
Discount rate on cash flow	7.5%
Electricity cost, station power	50 USD/MWh
Electricity cost, transaction power	70 USD/MWh
Regulation revenue	52.5 USD/MW per service hour
Rating for base fossil plants	400 MW
Rating for peaker fossil plants	75 MW
Plant Cost	Lead acid: 150 USD/kWh + 165 USD/kW of power electronics Flywheels 1630 USD/kW Coal base load: 2000 USD/kW Coal peaker: 1000 USD/kW Gas base load: 600 USD/kW Gas peaker: 800 USD/kW
Availability reduction due to regulation	Fossil fuel plants only: 6%

Table 3: Main assumptions included in [13]. Second part.

Both the charts outline important cost indexes, together with description of contribution to overall cost by maintenance, equipment, energy and CO₂, where considered. Flywheels appear to be convenient in the long term, mainly due to the low duration of lead acid batteries and the high initial cost of flywheels. In the case of this study, fossil fuel plants have proven to be not economically advantageous, in particular if the X factor is considered and a carbon tax is foreseen in the years to come. In addition, a strong hypothesis over the yearly amount of cycles (one cycle per hour, 24 hours a day, 7 days a week) is one of the factor that helps the most to show flywheels advantages.

1.6.2 NaS Batteries

A technology that is currently becoming attractive on a point of view of grid energy storage is represented by Sodium Sulfur (NaS) batteries. Even if their general application has a wider time horizon than high power ancillary services, they have good overload capabilities (up to 6x the continuous rating), fast response and forecasts of substantial cost reduction in the future. According to [36], their cost is 350 USD/kWh and 2000 USD/kW. On an energy density perspective, they can achieve 150 - 240 Wh/kg and 150 - 230 W/kg of power density and perform up to 5000 cycles (at *DOD* < 100%).

Some security concerns arose after the 2011 fire incident in Tsukuba. Indeed, one of the major drawbacks consists in the high operating temperature (300°C - 350°C), that is necessary in order to keep the elements liquid. As a result, proper thermal insulation is required, but generally no additional heating system is required, once the battery is running, thanks to the heat generated by the charge-discharge process itself. Fire hazard is related to the molten sodium that spontaneously burn if in contact with air or humidity.

1.6.3 Generic Comparison

This part has the goal of a comprehensive, even if not deeply detailed description of the main aspects of the energy storage technology. Moreover, often figures are displayed only in form of tables or inserted in text, thus limiting a comparison among all the aspects. It should be clear that up to now there is no clear winner in this market, some technologies may perform better than others only in specific tasks, and research (and the pace it will take) will eventually show the best options.

In the following charts the author took data from the cited literature, performed an empirical mean operation (where data were homogeneous) and integrated with subjective impressions if figures were missing. Even though a range of values associated to each parameter would be more descriptive, often it is hard to aggregate data from different studies, as they comply with different assumptions. Furthermore, a single number is easier to represent and gives a more immediate feeling of the proportions when performing visual comparisons.

	€/kW	€/kWh	Ease of siting	Time response	Stand-by losses / self-discharge	Efficiency 10 = 100%	N. of cycles
Underground Diabatic CAES	1250	156	5	4	1	6.5	20000
Pumped Hydro	2100	263	2	4	1	7.5	20000
Flywheels	1254	5015	8	9	10	9.2	20000
NaS Batteries	1538	269	7	9	5	9	3500
Li-Ion Batteries	410	650	10	9	5	9	4000
Lead-Acid Batteries	143	100	10	9	6	8	1000

Table 4: Study assumptions

The radar plot depicted in fig. 12 is obtained scaling all the values contained in table 4 on a range of 0 to 10. In other words, the worst performing technology, for a specific index, has assigned value of zero. In this sense, it may be referred as relative.

Some other aspects may be better seen through a scaling on absolute values, as in fig. 13. For example, efficiency ranges from 65% to 92%,

and the first graph implicitly hides this aspect. Caution should be used while considering some axes (the stand-by losses axis, for example), as they are directed conversely than others: the lower, the better. Some sharp

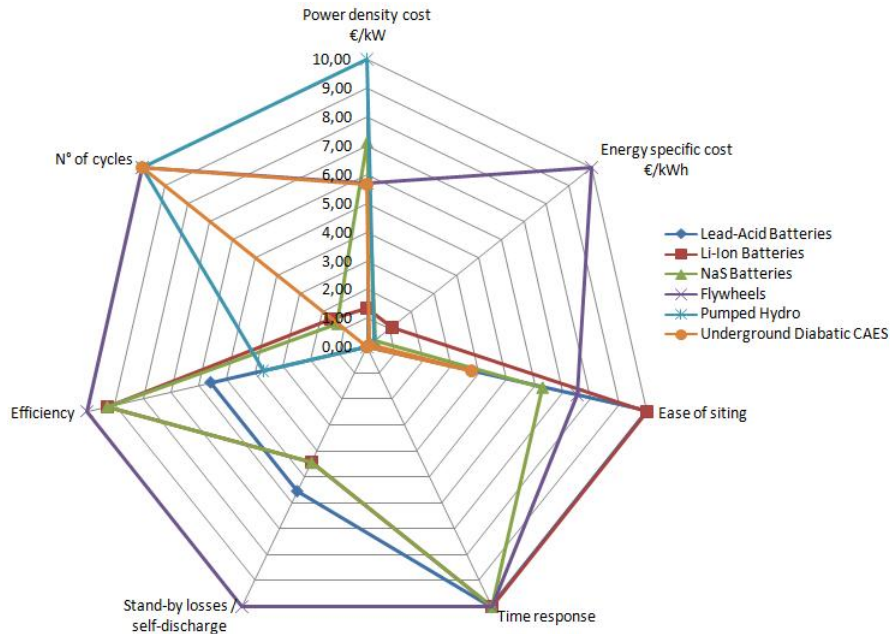


Figure 12: Radar plot in relative terms.

differences among the considered technologies are worth to be pointed out: Flywheels have an energy specific cost that is an order of magnitude higher than other technologies. As a consequence, only high power, low energy applications or duties where it is required a lot of cycles per year and fast response simultaneously can be envisaged as convenient for flywheels.

CAES shows low energy density cost, as well as long lasting availability, but is penalized in efficiency and siting, together with slow response with respect to technologies that use inverters.

Overall, it's not easily understandable where the best performing solution lays, whereas single applications can be considered with the goal to rank a preferred technology for each of them.

A Levelized Energy Cost (LEC) approach can help reducing the number of variables to consider, but still requires assumptions concerning the evaluation time frame, required return on investment, discount rate and more specific hypotheses for each technology, resulting in a partial view of the big picture.

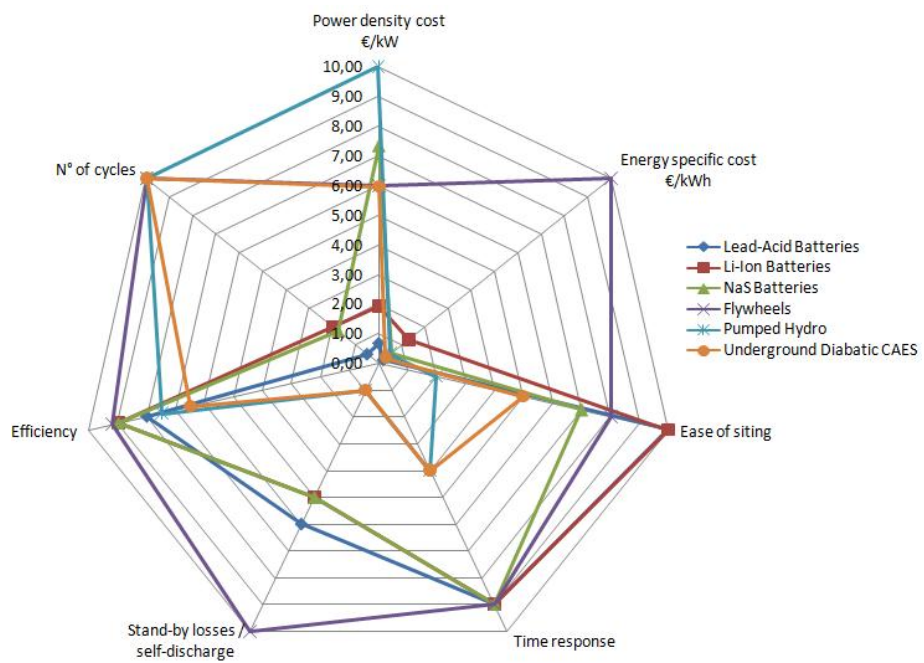


Figure 13: Radar plot in absolute terms.

Chapter 2

Flywheels

2.1 Flywheel Technology

The theory behind flywheels is well known and consolidated and no quantum leap improvement is expected in the near future. Rather material advance (together with the progress in power electronics) is the factor that allowed the development of commercial flywheels with a focus on energy storage, instead of mechanical load smoothing as it used to be until some decades ago.

The operational principle can be explained recalling the theory used for thick walled pressure vessels [14], i.e. the study of a solid body under axisymmetrical geometry and stress conditions. The stresses are calculated through:

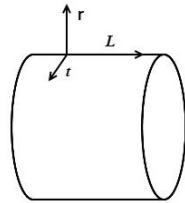


Figure 14: System of cylindrical coordinates, located on a general point out of the rotation axis.

$$\begin{cases} \sigma_r(\rho) = A - \frac{B}{\rho^2} - C\rho^2 + \frac{\nu}{1-\nu}\sigma_l \\ \sigma_t(\rho) = A + \frac{B}{\rho^2} - D\rho^2 + \frac{\nu}{1-\nu}\sigma_l \end{cases} \quad (2.1)$$

where

$$C = \frac{3+\nu}{8}\sigma_0 \quad D = \frac{1+3\nu}{8}\sigma_0 \quad \sigma_0 = \rho_{mat}\omega^2 r_{ext}^2 \quad (2.2)$$

Symbol	Expression - value	Unit of measure	Comments
σ_r	-	N/mm^2	Radial stress
σ_t	-	N/mm^2	Hoop stress
ν	0.3	-	Poisson's coefficient
ρ	$\frac{r}{r_{ext}}$	-	Adimensional radius
A, B, C, D	-	-	Constants to be calculated
σ_l	0	N/mm^2	Longitudinal stress
ρ_{mat}	-	kg/m^3	Material density
ω	-	rad/s	Angular velocity

Table 5: Symbol definition

Notice that σ_l is null only for the particular case of flywheels, as it accounts for possible forces that would act on the axis direction.

Considering a yield criterion, the Von Mises equivalent tensile stress is calculated through:

$$\sigma_{VM} = \sqrt{\sigma_1^2 + \sigma_2^2 + \sigma_3^2 - (\sigma_1\sigma_2 + \sigma_2\sigma_3 + \sigma_1\sigma_3)} \quad (2.3)$$

where subscripts 1, 2 and 3 are representing the three main stresses directions. In our specific instance, they coincide with r, t, l unit vectors defined in fig. 14.

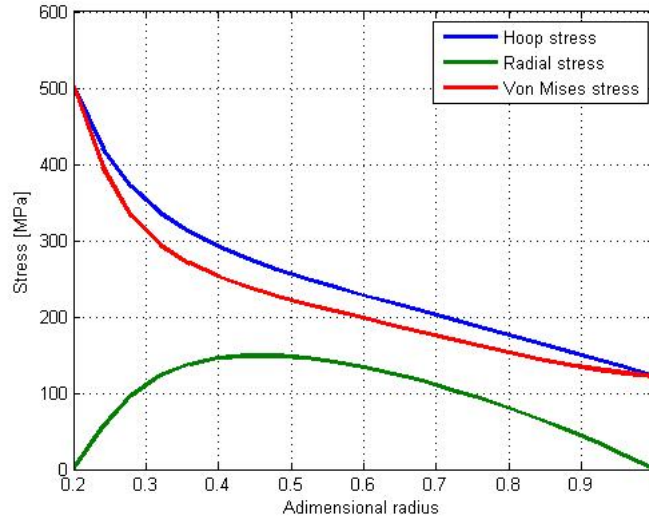


Figure 15: Stresses along the adimensional radius for a spinning flywheel

In turn, once the system of equations is solved through the imposition of 2.2 on 2.1 and additional conditions concerning the inner and outer

surface, typical behaviors of σ_r and σ_t , together with the Von Mises stress are shown in fig. 15.

The Guest stress in our specific case is coincident with σ_t , because the lowest principal component is always equal to zero.

Even if counterintuitive, the flywheel part that is more likely to break is the interior surface. This is confirmed by both yield criteria adopted. The approach is valid only for solid bodies, whereas composite material flywheels are made by a sequence of wound carbon sheets. In order to use the aforementioned method, it must be verified that the solid hypothesis still holds, together with a control of the differences that anisotropic behavior of composites may introduce.

In order to gain higher predictive power, viscoelastic and creep models need to be implemented [15], but a proper investigation of the phenomena is beyond the content of this thesis.

Fatigue must be explored in depth as well since the typical expected life of FESSs is 20 years, resulting in tens of thousands of cycles, hence exactly where the yield strength is subject to degradation:

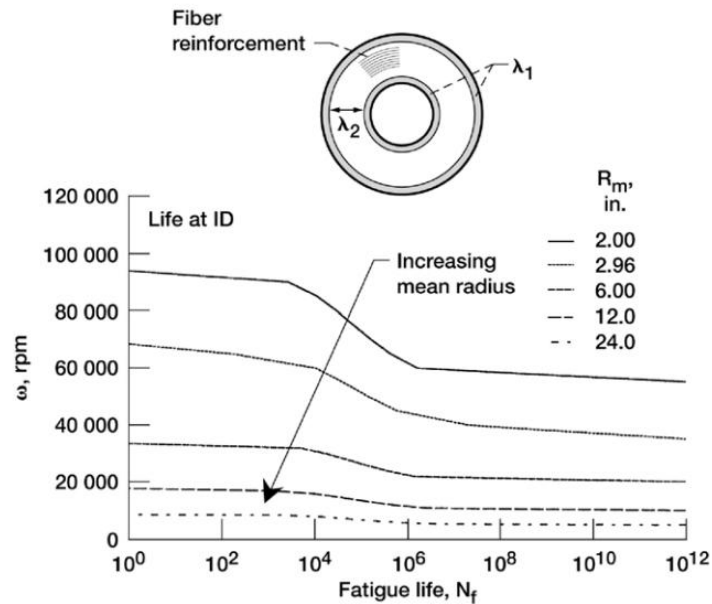


Figure 16: Generalized speed versus cycles curve indicating the onset of fatigue initiation cracks at the inner radius of the composite core. [15]

Fig. 16 represents the stress that leads to failure in the inner diameter (ID), as a function of the number of fatigue cycles applied and the flywheel mean radius. More precisely, the maximum rotating speed is calculated,

which corresponds to a stress that would lead to flywheel failure.

2.2 Materials

As mentioned before, modern flywheels are made by composite materials. Despite their low density, carbon fibers can yield extraordinary loads over a direction. Many authors outlined theoretical energy densities for composites, with a precautionary approach it is reported the one proposed by [16], even if others show higher figures [17]. Neglecting for a moment the weight of motor/generator, shaft, bearings and housing, such densities are advantageous with respect of common batteries Li-ion (110-160 Wh/kg), Ni-MH (60-120 Wh/kg), Pb (30-50 Wh/kg) [18].

Material	Density [$\frac{kg}{m^3}$]	Tensile strength [MPa]	Max energy density [$\frac{kWh}{kg}$]	Cost [$\frac{€}{kg}$]
4340 Steel	7700	1520	0.05	1
<i>Composites</i>				
E-glass	2000	100	0.014	11.0
S2-glass	1920	1470	0.21	24.6
Carbon T1000	1520	1950	0.35	101.8
Carbon AS4C	1510	1650	0.30	31.3

Table 6: Material properties of composites. [17]

The theoretical reason behind composites choice can be explained in a few equations: assuming as a reference figure 17,

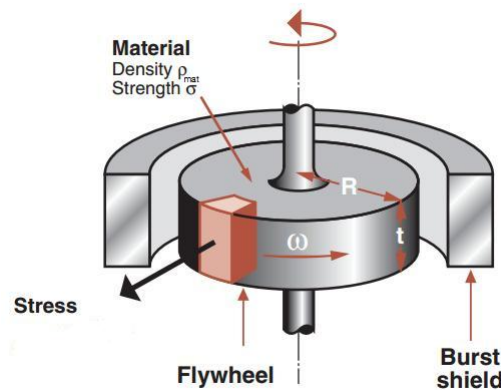


Figure 17: Flywheel schematic drawing.

the amount of energy stored in a spinning body is

$$E = \frac{1}{2}J\omega^2 \quad (2.4)$$

where J is the moment of inertia and ω is the angular speed. In case of a disk, J is given by

$$J = \frac{\pi}{4}\rho_{mat}R^4t\omega^2$$

and in turn the flywheel mass results

$$m = \pi\rho_{mat}R^2t \quad (2.5)$$

joining 2.5 and 2.4 together leads to

$$\frac{E}{m} = \frac{1}{4}R^2\omega^2 \quad (2.6)$$

as featured by [19], if ν is close to 0.3, maximum stress can be approximated as

$$\sigma = \frac{1}{2}\rho_{mat}R^2\omega^2$$

that finally allows to combine the last two equations and state

$$\frac{E}{m} = \frac{1}{2} \left(\frac{\sigma_{lim}}{\rho_{mat}} \right) \quad (2.7)$$

where σ_{lim} represents a precautionary strength for the material.

In order to identify the geometry maximizing the energy density for a given material property (i.e. R and σ are design variables), a graphic approach on the $\rho_{mat} - \sigma_{lim}$ plane depicted in fig. 18 can be adopted. M1 represents an indifference boundary for what concerns energy-to-weight ratio, even if lowest density materials must be discarded because they would lead to excessively low energy-to-volume ratios.

As a result satisfying choices are in the upper part of the plane, that now justify why composites are selected for flywheel applications, despite their relatively low density. Ceramics are discarded due to their low toughness.

On the other hand M2 is an indifference boundary for fixed density, useful once the geometry is not a design variable and the stresses are not of concern (relatively low speeds).

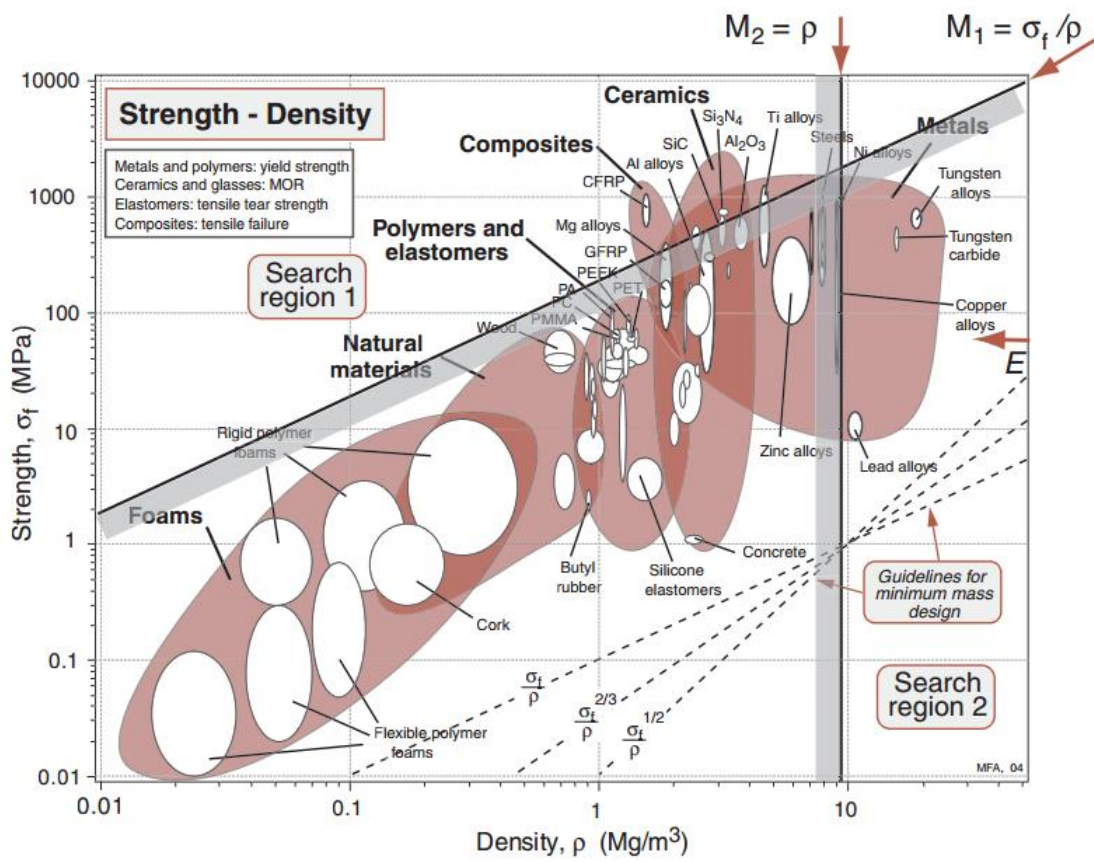


Figure 18: Choice among various macro-regions of material. [19]

2.3 Main Installations

Throughout the world many successful installations proved the flywheel feasibility, as well as duration on the long term. Nevertheless, they often consisted of experimental projects, thus without a clear basis where to evaluate costs and learning rates that would come from mass production. Recently, Beacon Power built a frequency regulation facility in Stephen-

Manufacturers	Countries	Specifications
Satcon	USA	2.2 MVA x 12 sec
Hitec	Netherlands	2 MVA x 10 sec
Piller	Germany	1.1 MVA x 15 sec
Caterpillar/Active Power	USA	240 kW x 14 sec
Pentadyne	USA	120 kW x 20 sec
Trinity	USA	100 kW x 15 sec
Beacon Power	USA	2kW x 3 hours 100 kW x 15 min 250 kw x 25 sec 250 kW x 6 min

Table 7: Main products worldwide up to 2009. [8]

town, NY that has 20 MW of rated power and 5 MWh of stored energy. This result is one of the most remarkable achievements done in the sector up to now, together with the ROTES project of the Okinawa Electric Power Company, provided by Toshiba in 1985. The latter consists of a slightly different approach: the flywheel is coupled on the power plant generator axis, hence operating in a really strict speed range (600 rpm \pm 15 rpm). It is made of 6 single disks, each of 6.6 m diameter and 0.4 m height and a weight of 107 ton. During the discharge process (30 sec), it can deliver up to 160 MW.

Chapter 3

Large Scale Kinetic Energy Storage (LSKES)

The aim of this chapter is to identify key advantages that may arise from a large scale flywheel energy storage. Concretely, as in most of engineering applications, large dimensions generally implies increased overall efficiency, as well as higher payback of fixed costs. Some preliminary cost analysis is also performed, in order to show the potential feasibility of the concept.

3.1 Acting Forces

The centrifugal force exerted on a body that spins on a circular path is given by

$$F_c = m\omega^2 r = m \frac{v^2}{r} \quad (3.1)$$

On the other side, the energy carried by a moving body is

$$E = \frac{1}{2}mv^2$$

Imposing a constant centrifugal force, set a priori according to stress analysis, it can be shown that

$$\text{const} = \frac{m}{r} \frac{2E}{m} \implies E \propto r$$

Apparently the equation implies that the higher the radius, the higher the amount of energy stored, at mass parity. Unfortunately, for flywheels

this does not happen due to the force distribution that opposes centrifugal stress: as depicted in fig. 19, the higher the radius, the lower the normal component (red) of tangential force (magenta). The magenta arrows represent the hoop stress acting on the material, and they are intentionally drawn of same magnitude among the two flywheels, with the purpose to show that pushing to the limit of infinite the radius would result in zero normal force. Similar and more detailed proof of that can also be carried out through the equations stated in section 2.1. A consequence of the afore-



Figure 19: Force distribution as a function of radius.

mentioned behaviour is that for a given material but geometry to design, as radius increase the rotating speed must decrease. Overall, the amount of energy stored per mass unit is the same.

This is the starting point of the idea explained in the following pages. The concept is straightforward: if a large radius is adopted, the centrifugal forces are lower, but as mentioned before, relying to the material strength in order to compensate them is pointless. On the other hand, if external forces could be applied, that can result in increased speed limits and proportional energy densities (actually, proportional according to square of the speed). That is why we are concentrating on a large scale (big radius).

3.2 Energy Density

Generally speaking, a rigid piece of material rotating at speed ω , has the energy already defined by equation 3.1, that is worth to see on table 8 of speed values and associated energy densities. It is clear that the energy

Speed [m/s]	30	90	150	300	500	700	900	1100
Speed [km/h]	108	324	540	1080	1800	2520	3240	3960
Energy [Wh/kg]	0.12	1.12	3.12	12.5	34.7	68.1	112.5	168

Table 8: Energy density as a function of speed.

density starts to be interesting only for high speeds, thus let's set 300 m/s as a lower boundary of interest. A geometric solution to the statements made

before can be the one depicted in fig. 20: an underground tunnel kept at low pressure with a torus shape, containing material rotating and magnetically suspended. The rotating part can be represented by a long, closed sequence of train waggons. As described by fig. 20b, the upper red part of the tunnel would be exerting levitation force and thrust force, whereas the internal blue part would provide the force necessary to compensate the centrifugal one. With the aim of validating the system feasibility, from geometrical

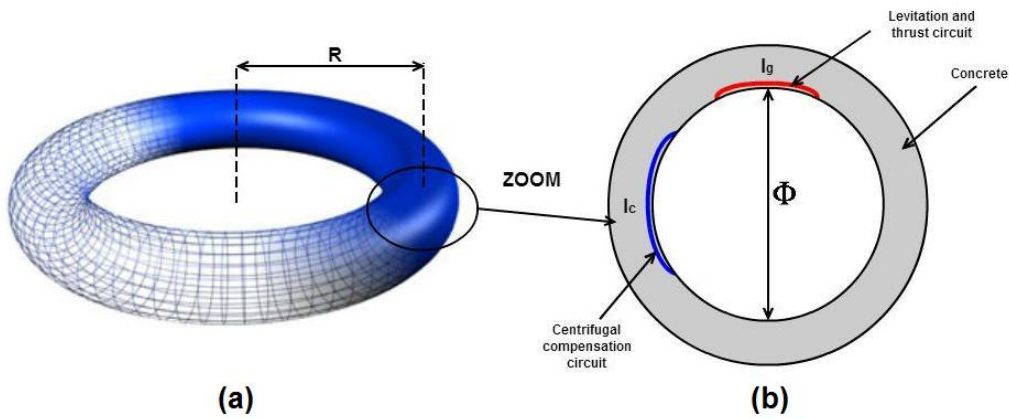


Figure 20: Hypothetical LSKES layout. (a): tunnel view. (b): tunnel cross section.

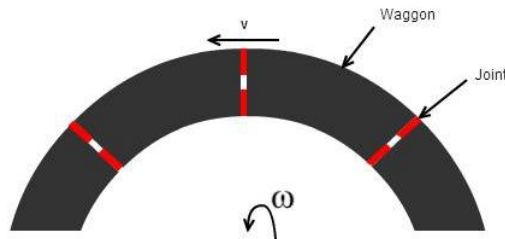


Figure 21: Tunnel section as seen from above.

specifications one can derive the air gap magnetic flux densities required, and compare them with usual values seen in electrical machines (0.5 - 1 T). The magnetic force exerted between two plates of surface A in a magnetic field can be expressed as:

$$F = \frac{1}{2\mu_0} \int B^2 dA \quad (3.2)$$

The torus volume is expressed by mean of the radial perimeter and the cross-section area:

$$V = A_t P_r \quad A_t = \pi \frac{\Phi^2}{4} \quad P_r = 2\pi R \quad (3.3)$$

The total spinning mass is

$$M = V \rho_{mat} \quad (3.4)$$

and the gravitational force that levitation must contrast:

$$F_g = Mg \quad g = 9.81 \left[\frac{m}{s^2} \right] \quad (3.5)$$

In terms of force per unit of radial perimeter

$$F_g^s = \frac{F_g}{P_r} \left[\frac{N}{m} \right] \quad (3.6)$$

Defining the cross-section perimeter as

$$P_t = \pi \Phi \quad (3.7)$$

and a coefficient that express the fraction of P_t used for levitation-thrust purposes (see figure 20):

$$l_g = K_g P_t \quad (3.8)$$

it's now possible to evaluate the flux density magnitude necessary for levitation

$$B_g = \sqrt{\frac{F_g^s 2\mu_0}{l_g}} \quad (3.9)$$

On a similar path, it can be calculated the flux density requested for centrifugal compensation. The arithmetic sum of centrifugal forces is expressed by

$$F_c = M \frac{v^2}{R} \quad (3.10)$$

per unit of radial perimeter

$$F_c^s = \frac{F_c}{P_r} \left[\frac{N}{m} \right] \quad (3.11)$$

Defining a second coefficient representing the perimeter utilisation for centripetal purposes

$$l_c = K_c P_t \quad (3.12)$$

Finally the magnetic flux density is

$$B_c = \sqrt{\frac{F_c^s 2\mu_0}{l_c}} \quad (3.13)$$

These results are valid if l_c and l_g are much smaller than Φ . Only under this assumption the magnetic forces can be considered to have a single direction, i.e. curvature effects are negligible. If it should not be the case, a rectangular cross-section can be adopted to ensure validity of the previous equations. An important factor is given by

$$K_f = \frac{F_c^s}{F_g^s} \quad (3.14)$$

only if K_f is close enough to 1, it can be reasonably thought even without a structural analysis that the waggon structure would bear the centrifugal (applied uniformly among the body) and centripetal (applied as a pressure in the internal torus surface) stresses. As an example, let's consider the

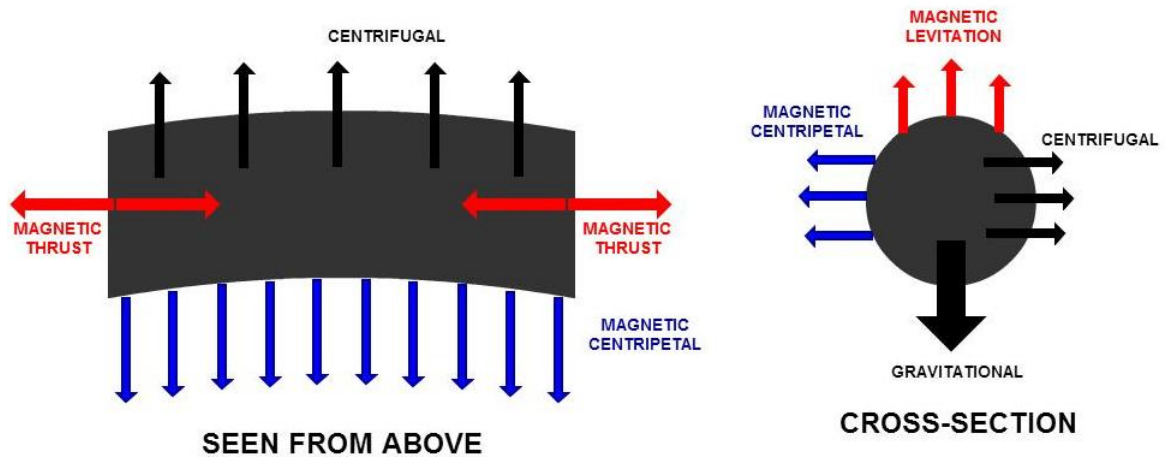


Figure 22: Acting forces on a waggon.

outputs from the spreadsheet that implements these equations. In addition we define t_d as the minimum time needed to discharge the LSKES and E as the total stored energy. The rotating material is assumed as steel, with a specific cost of 0.5 €/kg. Furthermore, C_{St} is the steel cost component per unit of stored energy.

The maximum power output would be of 1.45 GW, whereas K_f is 3.06. By the fact that the energy density is only a function of speed, in turn C_{St} is a speed function as well, and has value 40 €/kWh. Considering the price

Variable	R	Φ	v	ρ_{mat}	K_c	K_g	t_d
Unit of measure	[m]	[m]	$\frac{m}{s}$	$\frac{kg}{m^3}$	-	-	[h]
Value	3000	2	300	7800	0.1	0.3	4

Table 9: Sample data for a LSKES system.

Variable	P_r	M	F_c^s	F_g^s	K_f	B_c	B_g	E
Unit of measure	[m]	[ton]	$\frac{kN}{m}$	$\frac{kN}{m}$		[T]	[T]	[GWh]
Value	18840	461400	735	240	3.06	1	0.98	5.8

Table 10: Main characteristics of LSKES system obtained by the sample data.

advantage versus other technologies, the cheapest batteries as lead-acid (without the power electronics required to connect them to the grid) cost roughly 120 €/kWh [13], this allows at least 80 €/kWh of budget for tunnel and electrical machines construction.

Increasing the speed would be really convenient, as displayed in the following table:

Speed [m/s]	300	350	400	450	500	550	600
$C_{St} \left[\frac{\text{€}}{\text{kWh}} \right]$	40	29.3	22.5	17.8	14.4	11.9	10

Table 11: Steel specific cost as a function of the inverse of squared speed.

For what concerns drawbacks and limitations, large values of Φ are not feasible due to the fact that P_t grows linearly with Φ , but V and M grow quadratically with Φ , and the magnetic levitation and centripetal forces are proportional to P_t . In the focus of increased speeds, for conventional values of B_c such as 1 T, centripetal forces applicable are limited by geometric constraints on l_c . Imposing that for given Φ, B_c, l_c the centrifugal stress per unit of radial length F_c^s is kept constant, as v increases, R must grow with the square of v. Also high speeds can be an issue, even though levitation trains already reached 161 m/s [20] in ambient pressure conditions. Given the relatively low airgaps expected between waggons and the levitation and centripetal circuits, in the order of 10 mm, precision in tunnel manufacturing should be of concern.

Moreover, soil stability and earthquake-proof design must be kept into account, both for security and social acceptance aspects. Regarding energy losses and expected self-discharge ratios, at this point of analysis is impossible to quantify them with satisfactory approximation, even though they are expected to be much lower (in relative terms) than conventional dimen-

sion flywheels, due to scale efficiency. In conclusion, in order to consider LSKES as a way to energy storage, a set of technological challenges are yet not proven to be feasible nor reliable. Nevertheless a simplified cost analysis suggest there would be room for economic savings, in relationship with the main substitute technology as batteries. Further steps in this direction shall try to evaluate costs of the tunnel, as well as vacuum technologies and the electric machines. Once all the major cost components are defined, an optimisation procedure can be the right way to find best solutions, since the amount of design parameters appears to be too wide for a step-by-step manual optimal search.

Chapter 4

Transverse Flux Homopolar Synchronous Machine

4.1 Overview

Linear machines offer a set of peculiar characteristics that are desirable if a force orthogonal to the rotor motion is required or if machine modularity is advisable. By way of contrast, linear machines show undesirable aspects with respect to radial flux rotating machines such as border effects, generally lower power factor and the need of an air gap magnitude control. Depending on design choices many layouts of linear synchronous machines (LSM) can be obtained, as featured by Boldea [21] in fig. 23. Our interest is concentrated over homopolar, transverse flux, permanent magnet, flat single side machines (TFHSM). The reasons behind this choice can be summarized as follows:

- The only moving part is composed by tracks of ferromagnetic material;
- Low rotor losses, as the rotor winding is absent;
- Low energetic losses if only levitation is required;
- Modern permanent magnets allow a cost effective replacement of the field windings;
- High efficiency, typical of synchronous machines;
- High levitation force.

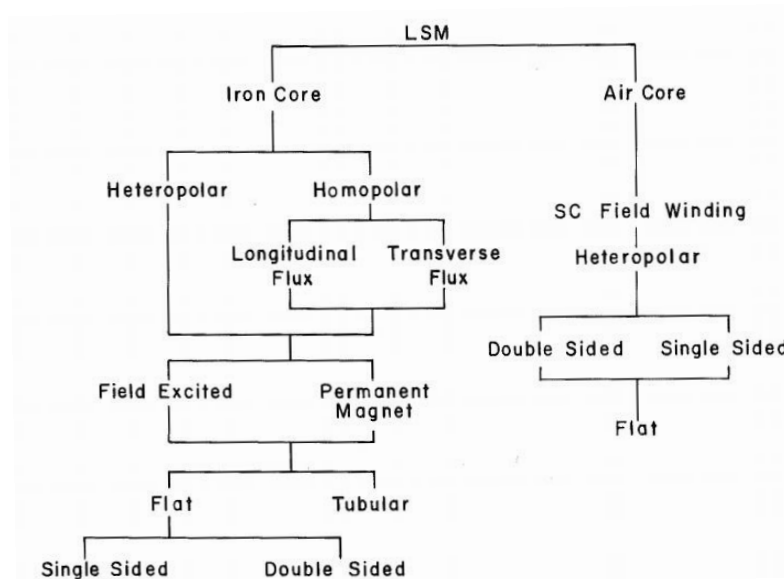


Figure 23: Various types of LSM, according to [21].

Moreover, superconductors have been avoided because of their high costs, and double sided geometry is discarded for the purpose of levitation: apart from forces that could arise from instabilities, such configuration does not produce any force in the direction orthogonal to the rotor moving direction.

Homopolar synchronous machines are employed in electric powered public transportation systems, exploiting the levitation force produced in order to reduce or eliminate the need of mechanical systems necessary to bear gravitational force of the structure to be moved. The concept project Swissmetro also considered such kind of machines as a viable solution to levitate and drive the under vacuum trains up to 500 km/h.

Another application concerns the industrial movement of objects, especially if the moving path has not a considerable length. LSM can provide interesting features because of they high reliability, low maintenance costs, and low pollution of the surrounding environment (particularly important within the food and process industry).

4.2 Flux Leakage

4.2.1 General Geometry

In contrast with current excited magnetic circuits, permanent magnets have low permeability with respect to ferromagnetic cores, resulting in flux

dispersions that are not passing through the air gap. For the sake of clarity, let us first analyze a simple magnetic circuit (fig. 24) consisting of a magnet, an iron yoke and an air gap: it would be interesting the development of a

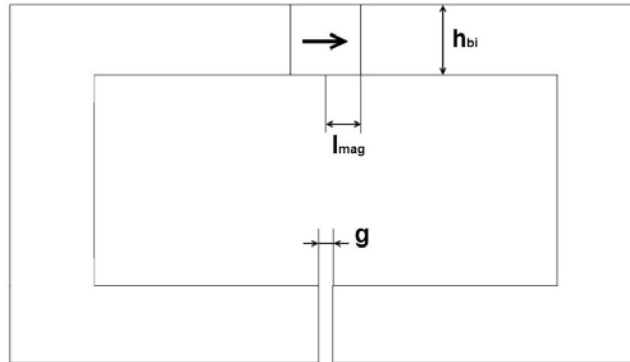


Figure 24: Generic magnetic circuit.

model predicting the amount of flux that reaches the air gap, with respect to the one generated by the magnet. In a first approximation, the iron magnetic permeability is assumed to be very high (relative permeability set to 100000). Two approaches have been investigated: FEM analysis (FEA) and reluctance equivalent circuit. As sketched in fig. 25, a wide extension

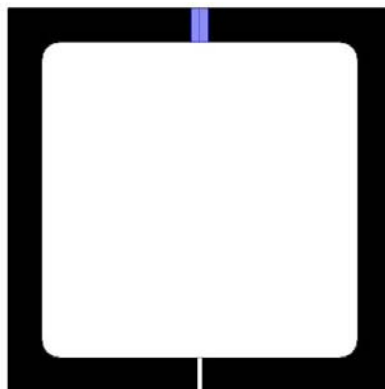


Figure 25: FEM model: in blue the two halves of magnet, in black the iron yoke.

of the iron has been adopted in order to gain generality: otherwise there would be the risk of missing some dispersion line due to the yoke edge curvature. In this way all the flux leakages located around the magnet or air gap have the possibility of evolve naturally toward the surrounding air, without constraints set by the iron yoke necessity to form a closed loop.

Several simulations have been carried out, for different values of the per unit coefficients:

$$K_1 = \frac{g}{h_{bi}} \quad K_2 = \frac{l_{mag}}{h_{bi}}$$

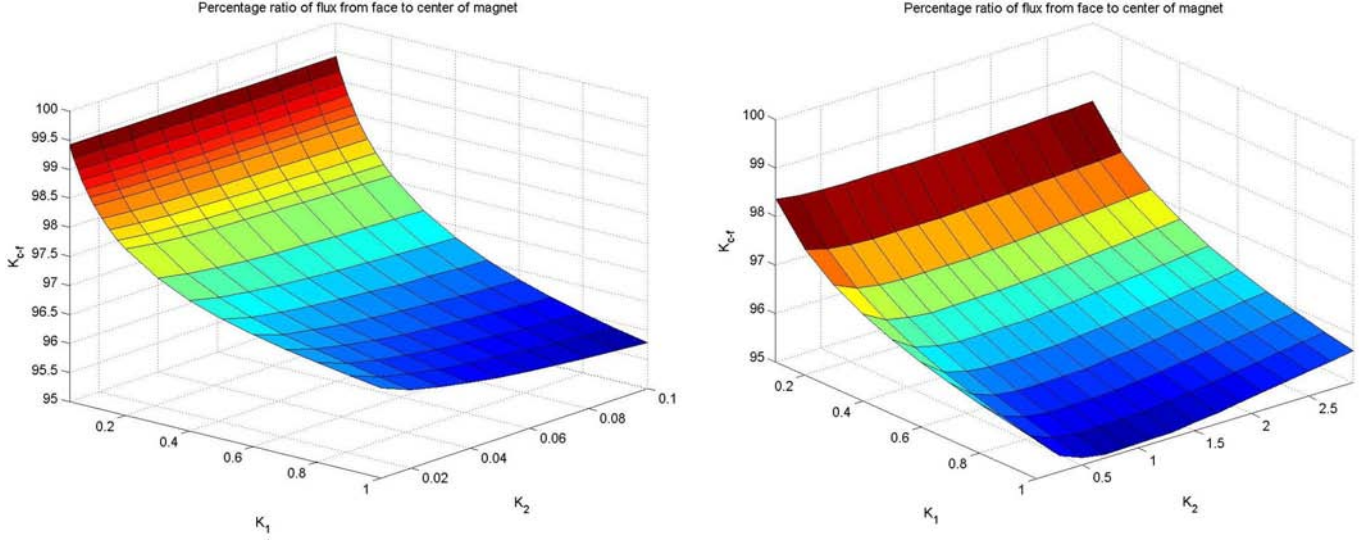


Figure 26: Percentage of flux from center to face of magnet, for different values of K_2 .

As it can be seen in fig. 26, among all the considered values of K_1 and K_2 , the ratio between fluxes on magnet face and magnet center K_{c-f} is not far from unity (100% in percentage terms). Consequently it is found no substantial flux dispersion from the magnet center to the magnet face, that leads to assume no dispersion on the lateral magnet face without losing generality. On the contrary, lines of flux that are leaving the iron yoke from the lateral surfaces are the ones responsible for the mismatch of flux from the magnet to the air gap.

The magnetic circuit approach requires a wider theoretical explanation, as depicted in the schematic figures 27 and 28. No line of flux is assumed as leaving the magnet from its lateral surface, whereas flux pipes of width $h_{bi}/3$ and circular shape are hypothesized. Formulating the problem per unit of depth and reducing the analysis to half geometry, the reluctances have expression:

$$R_g^A = \frac{\frac{\pi}{2} \left(\frac{g}{2} + \frac{h_{bi}}{6} \right)}{\mu_0 \frac{h_{bi}}{3}} \quad R_g^B = \frac{\frac{\pi}{2} \left(\frac{g}{2} + \frac{h_{bi}}{3} + \frac{h_{bi}}{6} \right)}{\mu_0 \frac{h_{bi}}{3}} \quad R_g^C = \frac{\frac{\pi}{2} \left(\frac{g}{2} + \frac{2h_{bi}}{3} + \frac{h_{bi}}{6} \right)}{\mu_0 \frac{h_{bi}}{3}} \quad (4.1)$$

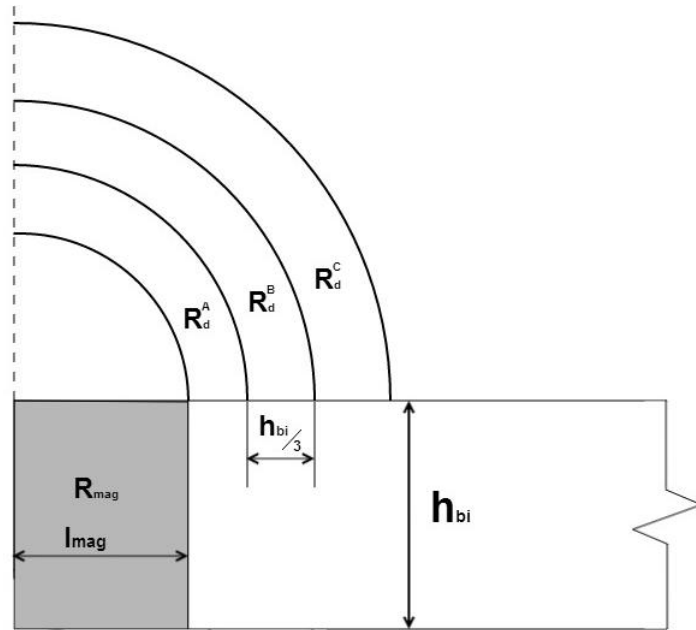


Figure 27: Half magnet and its associated flux dispersion pipes.

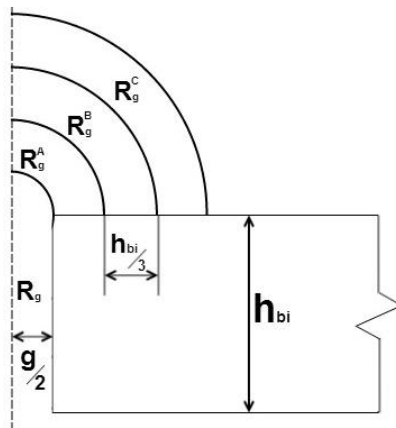


Figure 28: Half air gap and its associated flux dispersion pipes.

$$R_d^A = \frac{\frac{\pi}{2} l_{mag} (1 + \frac{1}{6})}{\mu_0 \frac{l_{mag}}{3}} = \frac{7\pi}{4\mu_0} \quad R_d^B = \frac{9\pi}{4\mu_0} \quad R_d^C = \frac{11\pi}{4\mu_0} \quad (4.2)$$

The iron yoke is assumed to have negligible reluctance, thus the other quantities to be defined are the magnet reluctance (where the recoil line

relative permeability is approximated to one) and the air gap reluctance:

$$R_g = \frac{g}{2\mu_0 h_{bi}} \quad R_{mag} = \frac{l_{mag}}{\mu_0 h_{bi}} \quad (4.3)$$

A comparison between the two methods can be made in terms of the flux amount reaching the air gap, for a given magnet flux. It is introduced calling K_{m-g} the ratio between the two of them. As featured in fig. 29,

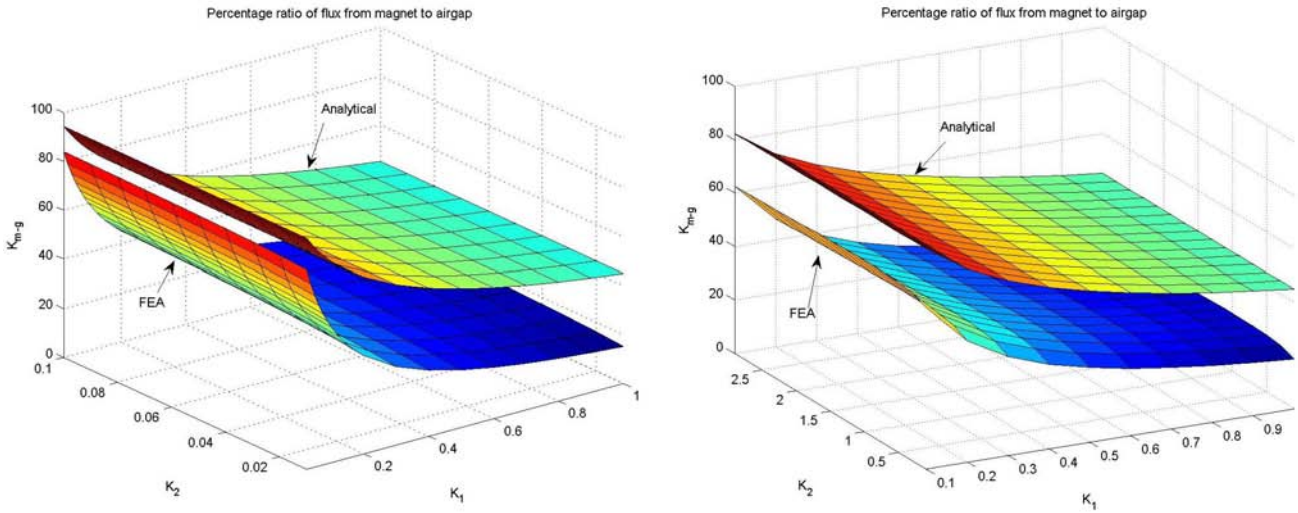


Figure 29: Percentage of flux from magnet to air gap, for different lengths of magnet and different approaches: Analytical and FEA.

however the dependence on the per unit parameters is satisfactorily reproduced by the analytical method, it leads to a remarkable overestimation of the flux percentage that would reach the air gap. Extending the number of reluctances that account for flux dispersion (i.e. defining R_g^D, R_g^E, \dots and R_d^D, R_d^E, \dots according to the procedure followed before) has shown to add no significant contribution in the matching between analytical and FEA models.

In a practical design approach 2D FEA simulations are not significantly time consuming for the computers available nowadays, ensuring at the same time a general evaluation of complex flux leakage phenomena. Thus the results can be used for different geometries, thanks to the dimensionless parameter formulation. This two combined factors allows an effective use of the method even in optimisation procedures.

4.2.2 TFHSM Geometry

In the case of a linear homopolar synchronous motor (fig. 30), the geometry is intrinsically three-dimensional, thus the adopted modeling strategy comprises a set of two 2D simulations, that describes the geometry in its two main planes: the transversal and the azimuthal sections represented respectively in fig. 31 and 32.

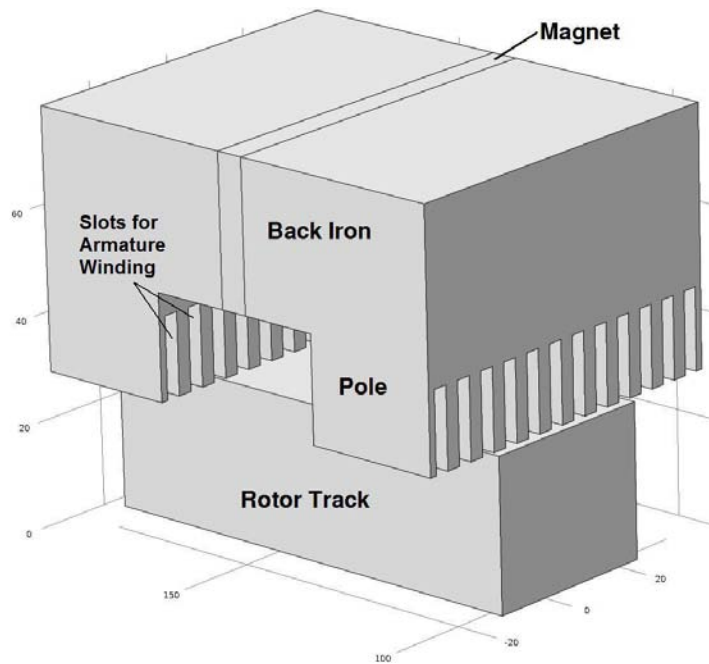


Figure 30: TFHSM 3D geometry.

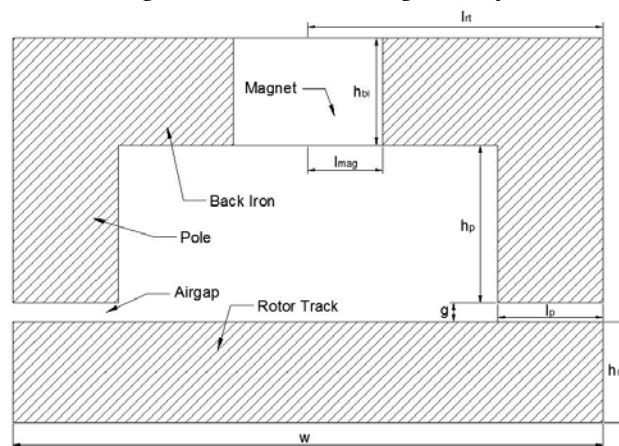


Figure 31: TFHSM transversal section.

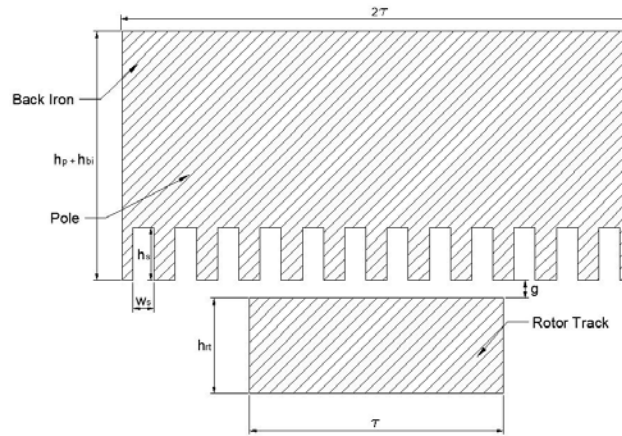


Figure 32: TFHSM azimuthal section.

Concerning slots, the armature winding has a peculiarity depicted in fig. 33: a crossing of the end winding connections on the window between poles is necessary to ensure the proper sign match between magnetomotive forces produced by magnet and armature. The drawback it implies relates to a relatively poor utilization of the armature copper, as the length of end winding connections is relevant with respect to the poles length, leading to a low power factor.

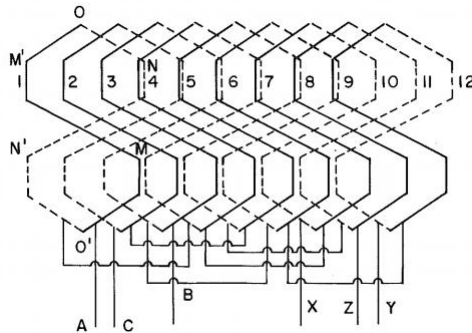


Figure 33: View from above of the winding connections. [21]

On a first approximation and in order to lower the number of parameters throughout the preliminary design, stator slots are not considered at this stage. Concerning the first section represented in fig.34a, only half of the geometry is simulated, relying on an homogeneous Neumann condition on the left vertical border. On the contrary, a Dirichlet condition is applied to the boundaries of the air surrounding the magnetic objects.

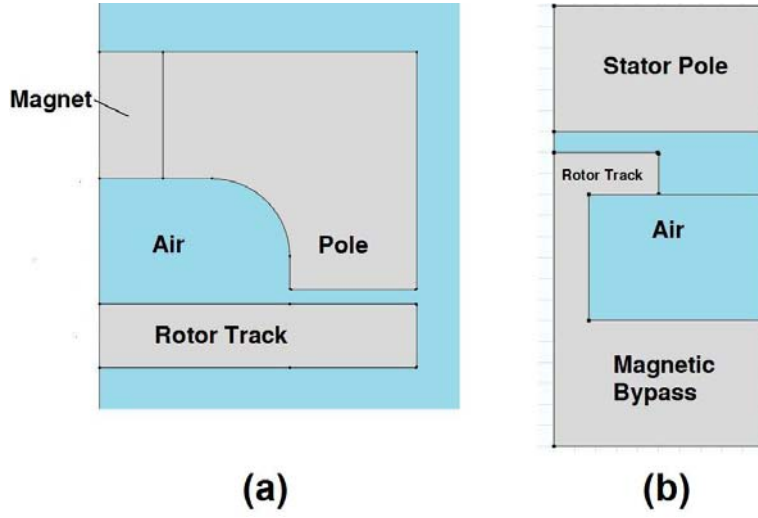


Figure 34: TFHSM FEA transversal and azimuthal section.

For the second section (fig. 34b), a magnetic bypass is necessary to ensure the correct path of magnetic flux density lines. Boundary conditions applied here are: on the top and bottom of the geometry different magnetic scalar potentials, whereas on the lateral sides a Dirichlet condition holds. In order to gain generality, both the simulations have been done using a constant, high magnetic permeability in the iron parts, thus freeing from the necessity to perform the calculations each time that a new material is adopted, at the expenses of a slightly inaccurate solution, especially if saturation has a non negligible effect. For symmetry reasons only half of the rotor track and stator are considered in fig. 34b. A parametric sweep is performed: according to the sizes introduced in figures 31 and 32, for the transversal section two parameters are defined

$$K_{t1} = \frac{g}{l_p} \quad K_{t2} = \frac{l_{mag}}{l_p}$$

and only one parameter for the azimuthal section

$$K_a = \frac{g}{\tau}$$

Both the sections are described in fig. 35, where the magnitude and direction of magnetic flux density is plotted along the geometries.

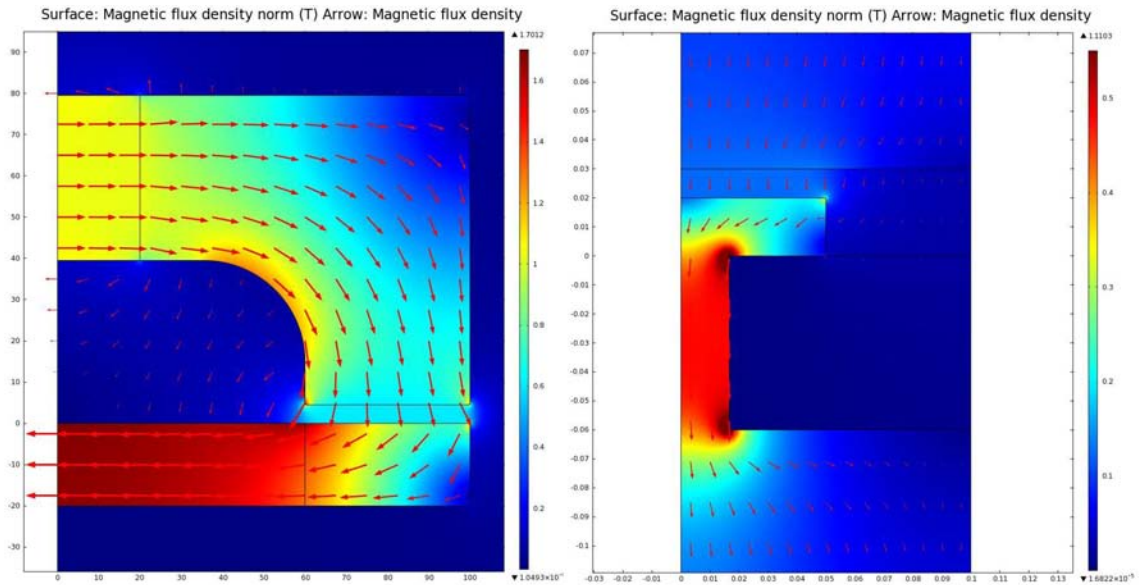


Figure 35: FEA plot of magnetic flux density.

The results in terms of flux percentages are plotted in a similar way with respect of what has been done previously for the general geometry, i.e. the percentage of flux that from the magnet reaches the air gap is considered. For the azimuthal section it is obtained:

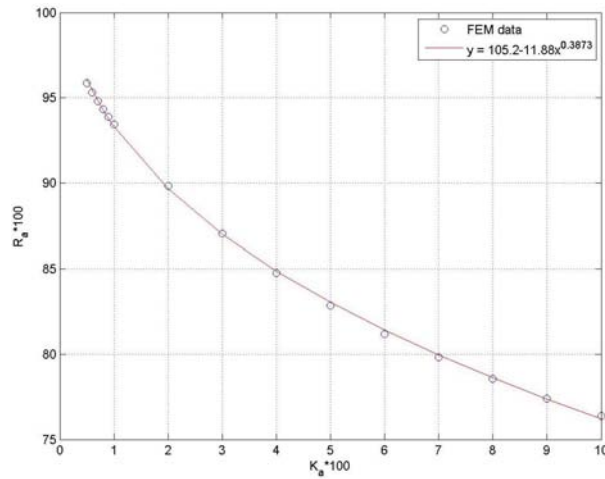


Figure 36: FEA results and numerical fit for the azimuthal section.

The ratio between the air gap flux and the magnet one is expressed by a numerical fit functions as:

$$R_a(K_a) \cdot 100 = 105.2 - 11.88(K_a \cdot 100)^{0.3873} \quad (4.4)$$

On the other hand, the transversal section simulation leads to a surface of results, given its dependency over two dimensionless parameters.

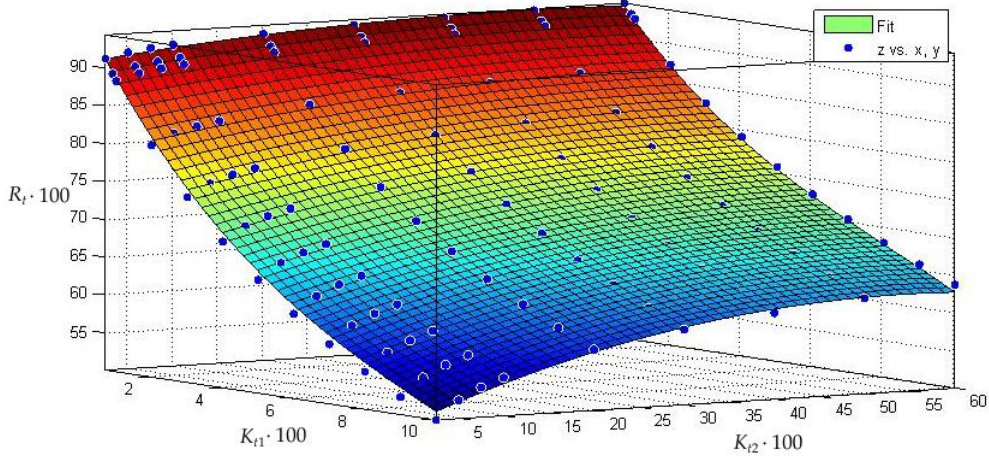


Figure 37: FEA data points and numerical fit for the transversal section.

in fig. 37 the blue dots represent FEA data, whereas the surface reproduces the numerical fit. The analytical expression obtained is, introducing R_t in a similar fashion of what done for the azimuthal section:

$$R_t(K_{t1}, K_{t2}) \cdot 100 = p_{00} + p_{10}K_{t1} + p_{01}K_{t2} + p_{20}K_{t1}^2 + \quad (4.5)$$

$$+ p_{11}K_{t1}K_{t2} + p_{02}K_{t2}^2 + p_{30}K_{t1}^3 + p_{21}K_{t1}^2K_{t2} + p_{12}K_{t1}K_{t2}^2$$

where K_{t1} and K_{t2} have to be inserted in percentage terms and the fitting parameters are expressed into table 12:

p_{00}	p_{10}	p_{01}	p_{20}	p_{11}	p_{30}	p_{02}	p_{21}	p_{12}
96.64	-8.938	0.1005	0.6406	0.05675	-0.0212	-0.00124	-0.001974	-0.0003089

Table 12: Fit parameters.

The fit goodness is expressed by an RMSE of 0.5212 and an R-square of 0.9985. Combining the two fits, it is possible to predict the air gap flux, given the flux produced by the permanent magnet Φ_{mag} and the per unit parameter values that describe the geometry by:

$$K_{\Phi} = R_t(K_{t1}, K_{t2})R_a(K_a) \quad (4.6)$$

$$\Phi_g = \Phi_{mag}K_{\Phi} \quad (4.7)$$

As it will be seen, K_ϕ will play a crucial role in the overall machine design, for both levitation aspects and torque production, because of the thrust force dependency upon the flux density magnitude in the air gap.

4.3 Analytical Design

The analytical procedure necessary for the design of a TFHSM is described in [21], where minor adjustments have been introduced in order to deal with the permanent magnets. Recalling the dimensions introduced in figures 31 and 32, and defining the new variables:

- $L_a = 2l_p$
- $K_w =$ winding factor
- $v =$ velocity of the rotor track
- $W_1 =$ number of turns per phase of the armature winding
- $F_t =$ thrust force
- $F_l =$ levitation force
- $p =$ number of pole pairs

Called B_{g0} the magnetic induction in the air gap, in the case of track presence, its value in the example figure 38 would be of 0.84 T. Performing the Fourier series decomposition of the flux density spatial distribution, the fundamental peak value is given by:

$$B_{g1} = 0.45 \frac{2}{\pi} B_{g0} \quad (4.8)$$

Then, the induced voltage in a phase of the three-phase armature winding with layout described in fig. 33 is expressed by

$$E_1 = \frac{4\sqrt{2}}{\pi} 0.45 K_w W_1 B_g v L_a \quad (4.9)$$

and the power balance

$$P = F_t v = 3E_1 I_1 \cos(\gamma) \quad (4.10)$$

where γ is the angle between the phasorial representation of E_1 and I_1 , the latter being the current through a phase of the armature winding. Hence,

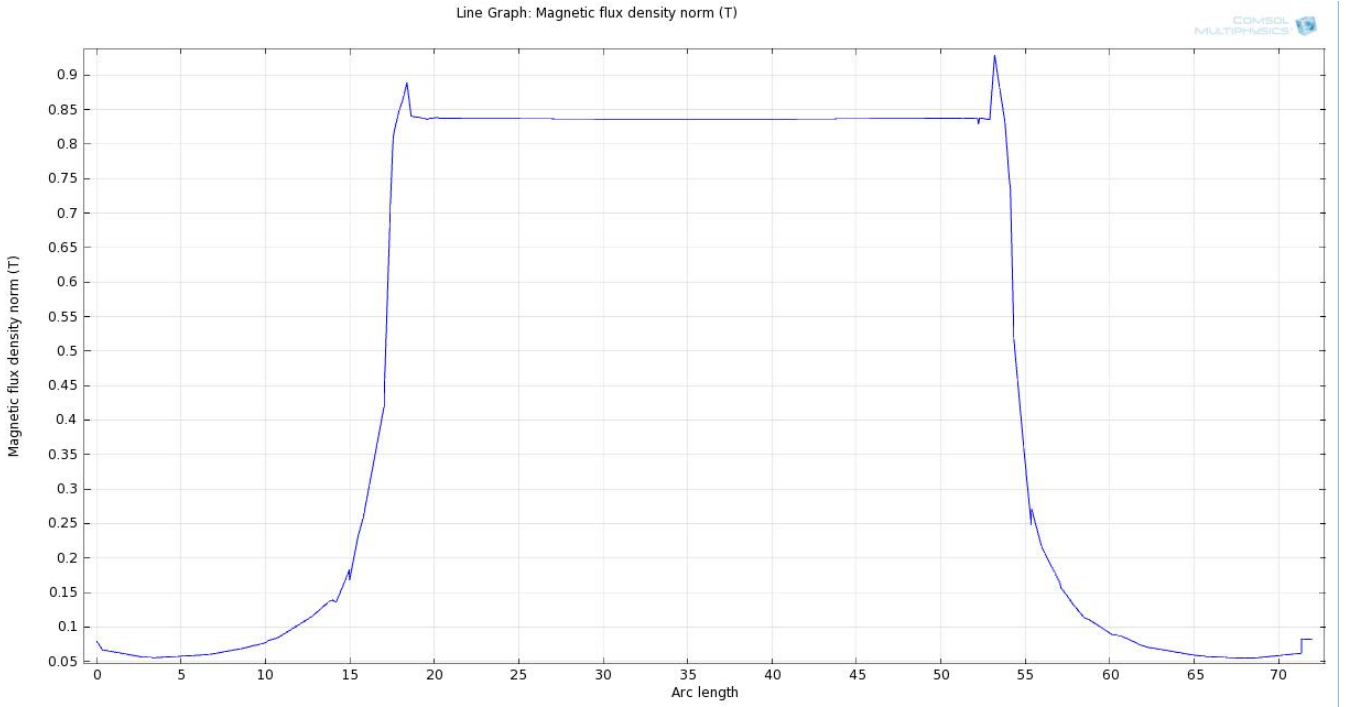


Figure 38: FEM calculation of the magnetic flux density among a line in the air gap, in case of stator slot absence.

the number of ampere-turns necessary to obtain the specified thrust force is determined:

$$W_1 I_1 = \frac{F_t \pi}{12 \sqrt{2} 0.45 L_a K_w B_{g0} \cos(\gamma)} \quad (4.11)$$

Then, introducing J_a as the rated current density in the armature and K_{fill} as the slot filling factor (usual values are $0.4 \div 0.55$), the slot area is calculated through

$$A_s = \frac{W_1 I_1}{p q J_a K_{fill}} \quad (4.12)$$

Moreover, the tooth pitch can be calculated from the pole pitch τ and q , the number of slots per pole and phase:

$$\tau_t = \frac{\tau}{3q} \quad (4.13)$$

Then, because of constructive reasons it is assumed as known the slot width, beginning the design process with an initial value set by the minimum feasible slot size:

$$h_s = \frac{A_s}{w_s} \quad (4.14)$$

finally the tooth width has value

$$w_t = \tau_t - w_s \quad (4.15)$$

On a first design stage of the magnetic circuit, the slots influence is not considered, hence the magnetic field distribution along the air gap if the track is present can be assumed as constant and represented by a single value B_g and a flux Φ_g . After the analytical magnetic design is completed, corrections by mean of FEA interpolations will be introduced in order to face the slot effect.

Regarding the space necessary to house the end winding, assuming a 45° angle for the end connections, the window length is then equal to τ (fig. 39).

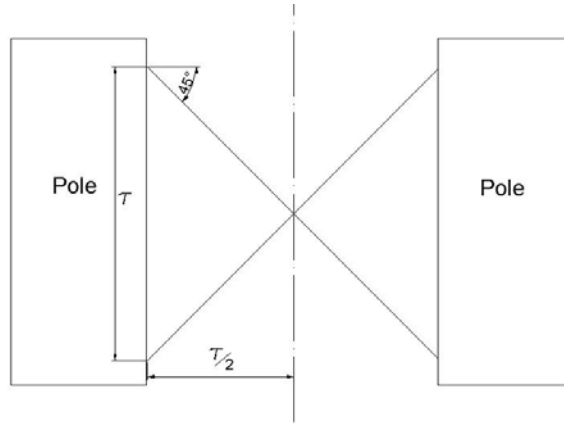


Figure 39: View from above of the window between the poles.

The pole height can be designed according to an increasing factor with respect to the slot height

$$h_p = 2.5h_s \quad (4.16)$$

Finally, the magnet needs to be optimised in order to achieve the maximum levitating force per mass (or volume) of magnet. Applying the Ampere-Maxwell's law to the transversal section of the geometry, in the case of no armature current:

$$\nabla \times \mathbf{H} = \mathbf{J} + \frac{\partial \mathbf{D}}{\partial t} \quad \text{in our case} \quad \frac{\partial \mathbf{D}}{\partial t} = 0 \quad \mathbf{J} = 0 \quad (4.17)$$

thus, on an integral form:

$$\oint \mathbf{H} \cdot d\mathbf{l} = \mathbf{H}_m l_{mag} + \mathbf{H}_g g = 0 \quad (4.18)$$

remembering the constitutive equation for a permanent magnet

$$\mathbf{B}_m = \mathbf{B}_0 + \mu_0 \mu_r \mathbf{H}_m \quad (4.19)$$

with

$$\mathbf{B}_0 = \text{remanent flux density vector} \quad \mu_r = \text{recoil line permeability}$$

and that for the air gap, which is linear

$$\mathbf{B}_g = \mu_0 \mathbf{H}_g \quad (4.20)$$

adding the null divergence of \mathbf{B} :

$$\oint \mathbf{B} \cdot d\mathbf{A} = 0 \quad (4.21)$$

and considering the approach followed in sections 4.2.2 and 4.2.1, the flux produced by the magnet and its portion that actually reaches the air gap are put in relation

$$\Phi_{mag} = 2\tau h_{bi} B_m \quad \Phi_g = l_p \tau B_g \quad \Phi_g = \Phi_{mag} K_\Phi \quad (4.22)$$

In addition a further leakage must be kept into account, namely the one located on the lateral surfaces of azimuthal section, figure 34b shows that no flux line is assumed as leaving the lateral sides. The reason behind this decision lays in the expected arrangement of multiple TFHSMs, on a circular path described in the following chapter (skip to fig. 43 at page 55 for a deeper insight). It is not known at this design stage the exact displacement of one stator with respect to the other, hence it is impossible to effectively simulate the flux leakages that would occur. In order to cope with this uncertainty, an additional factor K_l is introduced

$$\Phi_{mag} = \Phi_{mag} K_\Phi K_l \quad (4.23)$$

where an estimate of its value will be performed, based on 3D FEA.

Concentrating over K_Φ , its value is dependent upon the geometry: this leads to the development of an iterative procedure described in fig. 40.

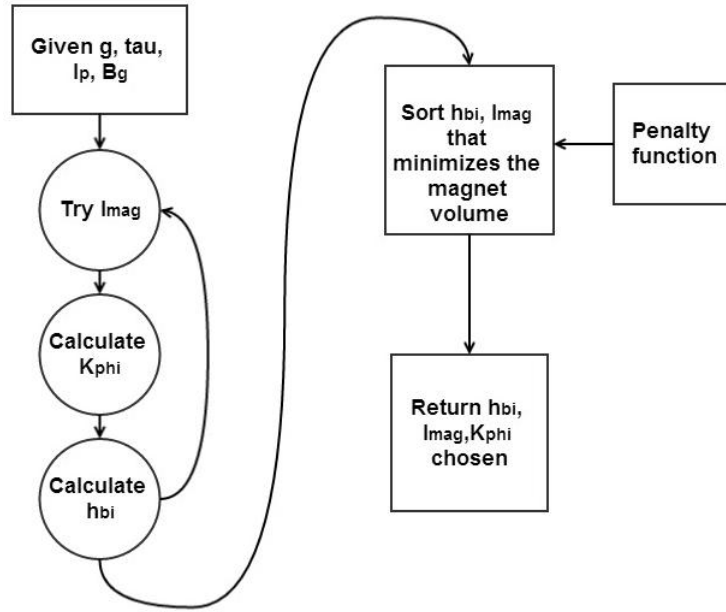


Figure 40: Flowchart of the magnet design.

Often the point that minimizes the magnet volume, for a given flux in the air gap, leads to a magnet with aspect ratio

$$M_{ratio} = \frac{l_{mag}}{h_{bi}} \quad (4.24)$$

too low, hence a lower limit in M_{ratio} is introduced and an automated decision process is achieved by mean of a penalty function that downgrades the objective function likelihood (in this case, artificially increases the magnet volume) in order to show the solutions that don't violate the constraint as preferable. In the specific instance, hard limit penalty functions are adopted, hence the limit is with no exception respected. The rotor track height can be assumed as

$$h_{rt} = h_{bi} \quad (4.25)$$

This choice ensures magnetic flux densities of limited magnitude inside the rotor track. An other criterion that lead to comparable results arise from the superposition of an average flux density within the track, given the air gap flux.

The slot presence effect, in analytical terms, is usually kept into account by mean of the Carter's factor [22], which assumes a cosinusoidal behavior of the magnetic induction along the air gap, with $h_s \gg w_s$:

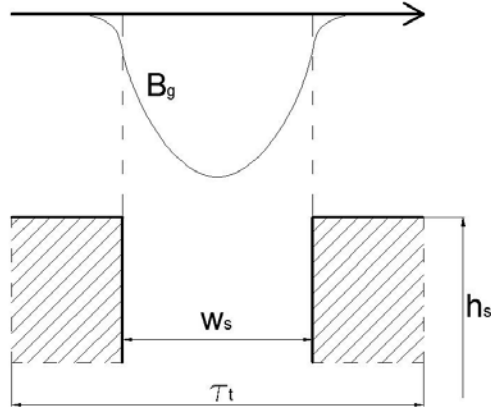


Figure 41: Cosinusoidal distribution of B along the air gap.

introducing an auxiliary coefficient

$$K_g = \frac{4}{\pi} \left[\frac{w_s}{2g} \arctan\left(\frac{w_s}{2g}\right) - \ln \sqrt{1 + \left(\frac{w_s}{2g}\right)^2} \right] \quad (4.26)$$

the Carter factor has expression

$$K_c = \frac{\tau_t}{\tau_t - K_g g} > 1 \quad (4.27)$$

by definition, the equivalent air gap that accounts for the slot effect is given by

$$g_{eq} = g K_c \quad (4.28)$$

In other words, all the previous equations concerning the magnetic aspects are still valid, but g_{eq} is replaced by g . The FEA are therefore carried out considering the equivalent increased air gap, leading to an account of increased air gap reluctance due to slot presence.

The levitation force is therefore calculated by mean of

$$F_l = \frac{1}{2\mu_0} (2l_p \tau) B_g^2 \quad (4.29)$$

Chapter 5

Design Example

5.1 Overview

As they are one of the benchmark products in the field, Beacon Power Flywheels have been analysed and a new electrical machine design is proposed. There exist two main versions, according to the predominant purpose that the flywheel is expected to serve (fig. 42b):

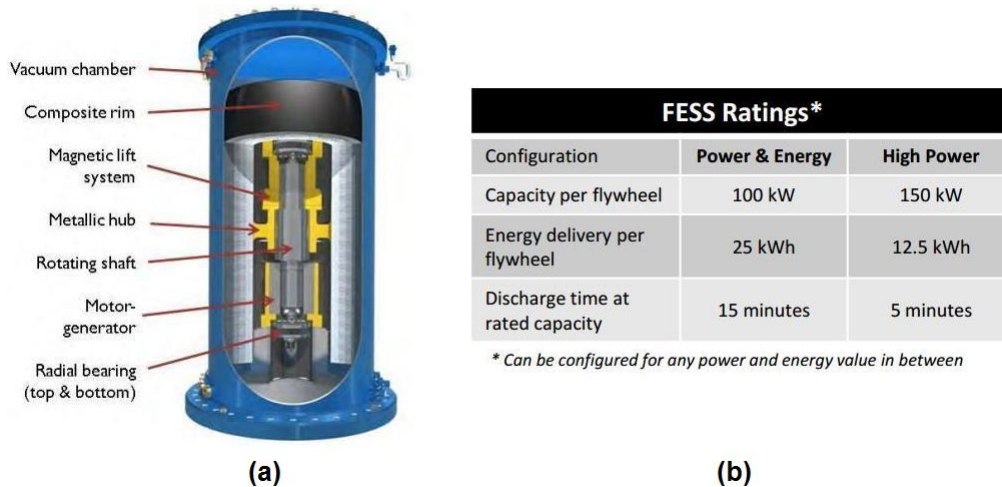


Figure 42: Beacon Power's Generation 4 Flywheel schematics and major specifications. [23]

The carbon fiber flywheel is driven by a permanent magnet radial flux synchronous machine (which provides round trip efficiency of 85%), and is kept under low pressure (<1 mtorr) thanks to the surrounding vacuum-sealed container. Magnetic bearings mix permanent magnets and current-

driven coils (hybrid magnetic bearings) in the goal of flywheel suspension. Hourly standby losses accounts for 0.03 MWh per MW installed, hence a 25kWh / 100kW configuration would completely self discharge within 8.3 hours. According to manufacturer specifications, this technology is expected to deliver 20 years of service with little or no maintenance.

Their major purpose consists in grid frequency regulation, hence the modular structure depicted in 42a is usually installed in a large array, scaling up to tens of MWs. The electronic power module has volume of ca. 1.5 m³ and is housed in dedicated containers, whereas the flywheels are usually installed below ground level, surrounded by a concrete protective housing.

In this work of thesis the power & energy configuration is analysed, with 25kWh of storing capacity. Moreover, the carbon fiber flywheel has the sizes and operating speeds specified in table 13, that estimating a density for the carbon fiber of 1.5 ÷ 2.5 kg/dm³ would result in a weight of 800 ÷ 1330 Kg. For simplicity, it is chosen a density of 1.92 kg/dm³, requiring a levitation force equal to 10 kN, therefore corresponding to a mass equal to 1020 kg to be suspended.

Parameter	Value
Inner diameter	45.7 cm
Outer diameter	81.3 cm
Height	150 cm
Volume	0.53 m ³
Min. rotating speed	8000 rpm
Max. rotating speed	16000 rpm

Table 13: Carbon fiber flywheel dimensions and operating speeds.

A sharp difference in the expected use of the flywheel is however introduced: the goal of the present work consists in trying to design an electrical machine that would have sufficiently low losses to allows FESSs to enter the market of longer term energy storage, in the range of hours. As many batteries are evaluated among a cycle of 6 hours, the same is adopted as a reference for the design. Assuming a successful layout is found and even if operating under low pressure conditions, drag losses are still to be checked, as their share with respect to total stand-by losses will increase significantly because of the expected reduction of electric machine losses. The evaluation of such aerodynamic phenomena is not simple and beyond the scope of this work, and will be one of the issues to be faced in further work. As a reference, [24] performed an electrical machine and magnetic

bearing design improvement on a carbon fiber flywheel (external maximum tip speed of 550 m/s) expected to provide power for a 3-hours cycle. In his specific case windage losses accounted for 6.7% in the benchmark case and 20.4% in the target result.

The output rated power is then easily obtained by mean of

$$P = \frac{E}{t_{cycle}} = \frac{25 \text{ kWh}}{6 \text{ h}} = 4.17 \text{ kW} \quad (5.1)$$

Independently from the electrical machine configuration, maximum torque is required when attaining the lower speed limit, at constant power output:

$$T = \frac{P}{\Omega_{min}} = \frac{4.17 \cdot 10^3}{8000 \frac{2\pi}{60}} \simeq 5 \text{ Nm} \quad (5.2)$$

on the other hand, the lower torque limit required to deliver full power at maximum operating speed is of 2.5 Nm.

In order to maximize the volume exploitation of the overall structure, there is interest in embedding the electrical machines inside the central hole of the carbon fiber cylindrical flywheel. As depicted in the figures 43 and 44, the idea proposed consists of three machines, each of them composed by a subset of TFHSM, positioned in a circular path. In the case presented, the example figure is obtained assuming 8 sub-machines for each of the three main ones. The required number of machines, denoted by n_m , will be selected after some preliminary 3D FEM simulations, used to evaluate the electromagnetic performance and the machine capability to meet the levitation and accelerating/decelerating torque requirements.

Even if it is not strictly appropriate to talk about pole pairs in an homopolar machine, let us still define p as the number of rotor tracks, that is related to the operating frequency of the electrical voltages and currents of the machine by mean of the angular speed n , expressed in rpm and the equation

$$f = \frac{pn}{60} \quad (5.3)$$

The choice of p must result from a compromise between an effective use of the active surface (high p value is preferable) on one hand and the limitation of the core losses (almost dependent on the frequency squared) on the other one. Table 14 reports the associated operating frequency linearly depending upon p .

Another crucial design variable is the air gap length. For the magnetic purposes, the lower the better, but mechanical aspects generally set a lower

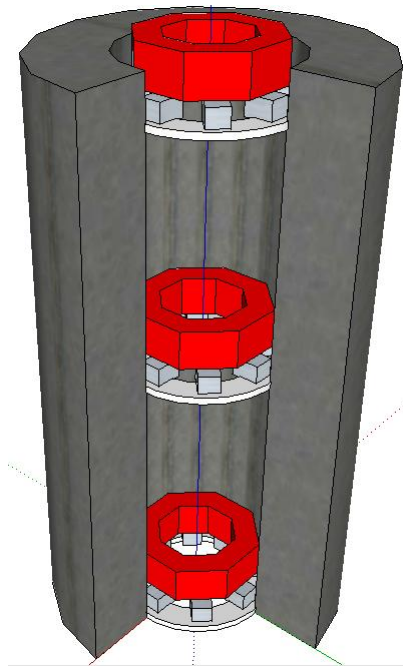


Figure 43: Proposed layout with three machines.

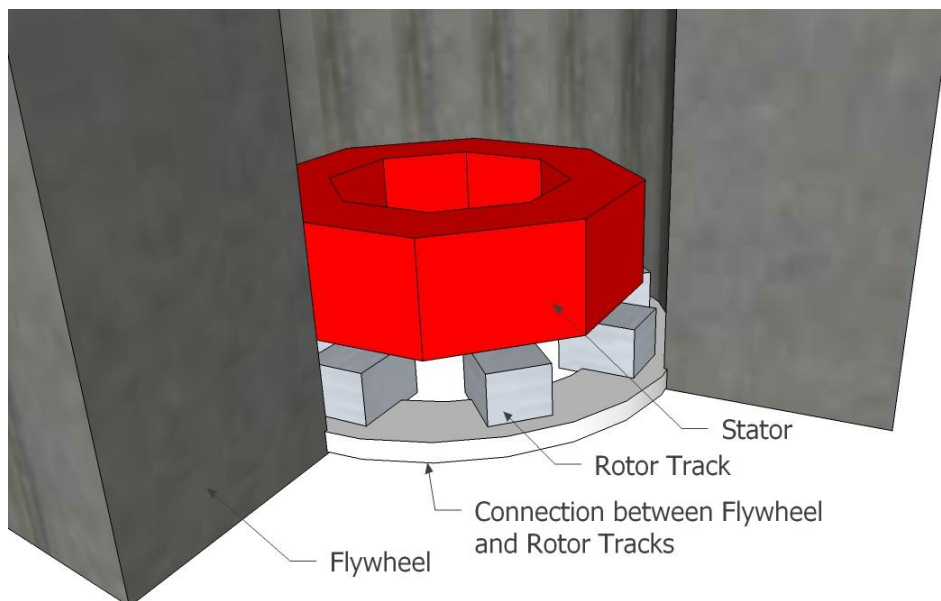


Figure 44: Details of the proposed layout.

bound to its value. An acceptable value proposed also in the literature

Number of pole pairs	Frequency range [Hz]
p = 4	533 ÷ 1067
p = 5	667 ÷ 1330
p = 6	800 ÷ 1600
p = 8	1067 ÷ 2133
p = 10	1333 ÷ 2667
p = 12	1600 ÷ 3200

Table 14: Operating frequency as a function of the number of rotor tracks.

[25, 26] is chosen to be

$$g = 1mm$$

considering the assumption as not excessive demanding: other working prototypes already deal with higher loads, similar rotational speeds and lower air gaps.

5.2 Materials

5.2.1 Magnetic Core

The magnetic core of the machine as well as the permanent magnet offer various material solutions, with relative strengths and weaknesses according to the major objective of the design procedure. Considerations upon the geometry of the core and the operating frequency, together with concerns over hysteresis and eddy current power losses, leads to the choice Soft Magnetic Composites: powders containing ferromagnetic particles used to manufacture also complex geometries by means of pre-formed molds. The process consists of two main stages: in a first compaction the powder is inserted in the shape through the Powder Metallurgy method. Afterwards, a heat-treatment allows the lubricants contained in the powder to evaporate and to obtain a partial relief of the stresses accumulated during the compaction.

The commercial product considered in this example is called Somaloy 700 3P, produced by Höganäs, and has the magnetic characteristics depicted in fig. 45 and 46:

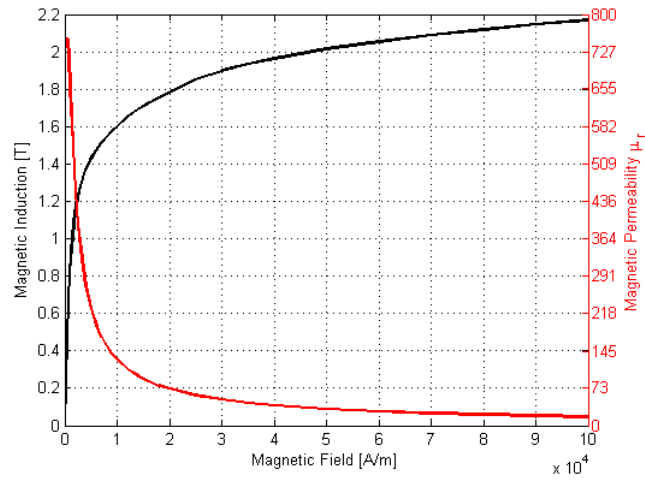


Figure 45: SMC B-H curve and its relative permeability.

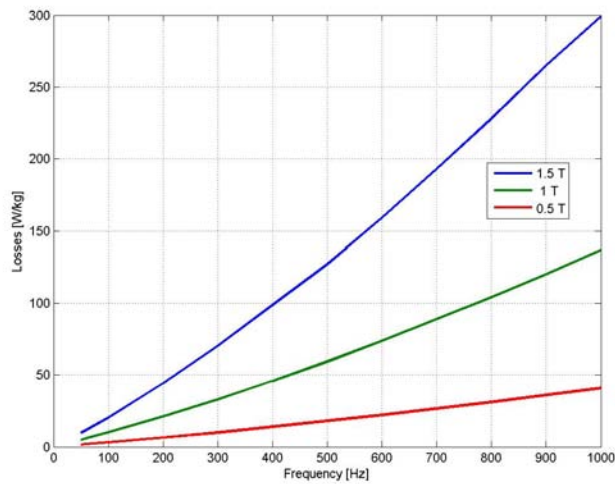


Figure 46: SMC losses as a function of frequency and magnetic flux density magnitude.

For a first design stage this material is selected, however other similar SMC powders with particularly low losses can be adopted, if it will be found that 700 3P cannot deliver the desired performances.

5.2.2 Permanent Magnets

Pushed by the need of increasing efficiency, designers of many types of electrical machines nowadays rely on permanent magnets as an alterna-

tive to electromagnets for magnetizing the machine. Among the most widespread, brushless DC and AC motors are state of art in many electric drives applications. This have been possible thanks to the progress made in the permanent magnet performances, mainly due to new materials such as NdFeB and SmC. Figure 47 offers a wide range of different magnets, together with their B-H curve, energy product hyperbole and permeance coefficient related to different magnetic circuits that can be connected to them. The introduction of some points of major interest in the chart is

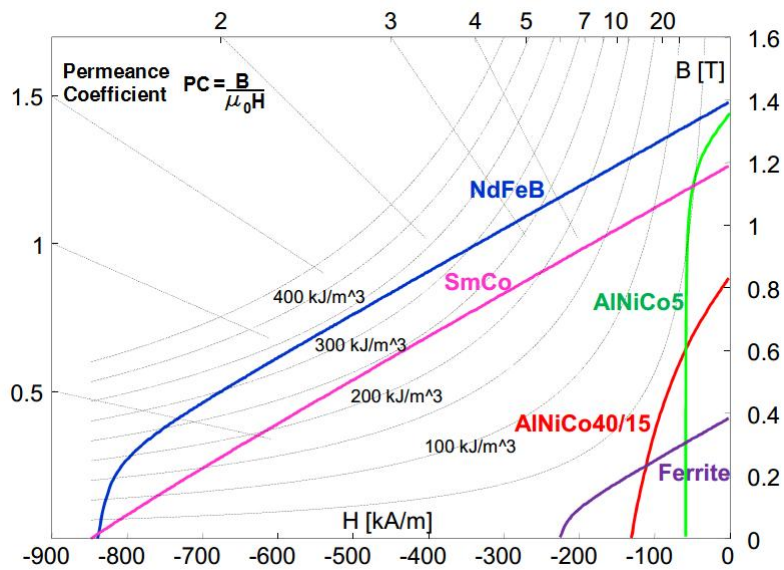


Figure 47: Typical B-H curve for different permanent magnets.

needed: B_r is referred as residual magnetization and is the value of B when the curve intersects the vertical axis (i.e $H = 0$). On the other hand, H_c is the coercitive field needed to annul B , in graphical terms it is the point that intersects the horizontal axis. According to [27, 28, 29, 30], the main characteristics of permanent magnets that can be foreseen as viable for the example specific application can be summarized as follows:

1. Neodymium Iron Boron

- (a) Highest B_r and energy product among all the magnetic materials;
- (b) Low temperature and oxidation resistance (nickel, zinc or polymer coatings are added). Problematic machining due to the Neodymium toxicity, and risk of injuries for the operators if handled magnets have considerable size;

- (c) Fabricated through direct particles sinterization (sintered magnets) or by mean of polymers or resins that cover the particles (bonded magnets). The latter have lower performances but are simpler to machine.

2. Samarium Cobalt

- (a) Most common compositions: Sm_1Co_5 e $\text{Sm}_2\text{Co}_{17}$;
- (b) Very expensive, but the cost is compensated by high possible operating temperatures, corrosion resistance and linear B - H characteristic;
- (c) Obtained through sinterization (sintered magnets) or by polymeric coating, which is also necessary in order to build large magnetized structures (bonded magnets), but lower temperature limits are a drawback (120°) of the second solution.

Magnet Material	Cost	Max. Energy Product [MGOe]	Coercitive field [kOe]	Max. Working Temperature [°C]	Machinability	Corrosion Resistance
Nd-Fe-B (sintered)	65%	Up to 50	Up to 30	180 -200	Fair	Poor
Nd-Fe-B (bonded)	50%	Up to 10	Up to 11	150	Good	Poor
Sm-Co (sintered)	100%	Up to 30	Up to 25	350	Difficult	Excellent
Sm-Co (bonded)	85%	Up to 12	Up to 10	150	Fair	Excellent
Alnico	30%	Up to 10	Up to 2	550	Difficult	Fair
Hard Ferrite	5%	Up to 4	Up to 3	300	Fair	Excellent
Flexible Ferrite	2%	Up to 2	Up to 3	100	Excellent	Good

Table 15: Resume of principal magnet characteristics [31, 32]. Conversion references: $1 G = 1e-4 T$. $1 Oe = 79.58 A/m$.

On a first design stage, NdFeB magnets are chosen because of their performances: dimensional constrains are relevant in the application considered, thus it is advisable to start with performing materials and check the machine feasibility, then eventually consider the use of more economic magnets.

Magnets in general suffer a performance degradation as temperature increases, but introducing this effect in a FEM software requires a coupled solution of the magnetic and thermal problem, hence a higher computational cost. As a consequence, it is assumed as known the magnet operating temperature, then the reduced performance can be calculated. In the specific case of NdFeB, residual magnetization is downgraded from 1.4T to 1.2T.

Parameter	Expression
Material	NdFeB
B_r	1.2 [T]
μ_r	1.1

Table 16: Assumptions concerning the permanent magnet.

5.3 Stator Module

The solution outlined consist in a set of rectilinear stators, arranged on a circular path:

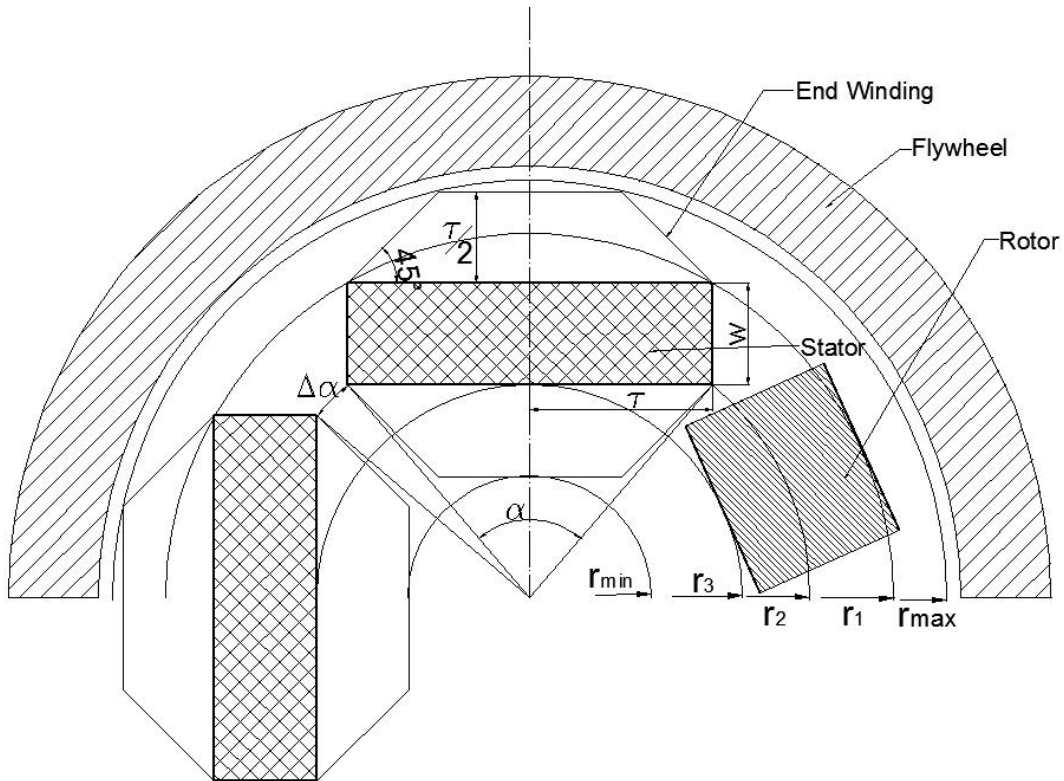


Figure 48: Hypothetical layout in the case of $p = 4$.

The rotor track is considerably larger than the stator, in order to avoid excessive flux concentrations as the track approaches the stator. Indeed, it has radial dimension of $r_1 - r_3$, when the stator has depth $w < r_1 - r_3$. Each of the stators has no periodicity, hence each module covers only a pole pair, thus p represents the number of stators, as well as the number of rotor tracks.

Recalling the variable defined in section 5.1, the total number of linear stators is then $p \cdot n_m$.

As described before the number of pole pairs p is linear to the operating frequency, but has also influence on a set of effects that are generally difficult to compare and then it is hard to operate in search of an optimal solution. A qualitative assessment is contained in table 17.

Issue	high p	low p
Curvature effects	↘	↗
Frequency ripple of levitation force	↗	↘
Frequency	↗	↘
End-winding length	↘	↗
Mean active surface	↗	↘
Lateral flux leakages	↗	↘
Stand-by losses	↗	↘

Table 17: Summary of the machine aspects mostly influenced by the decision of pole pairs.

In turn, a trade off has to be found in light of all the effects listed in the table. Once p is chosen, τ and w are the variables to concentrate on, trying to maximize the area covered by the stators and avoiding unfeasible configurations due to interference. The main constraints and aspects to take into account are:

- Due to the presence of the end winding connections under the central window (assumed for simplicity as occupying τ , see fig. 39) that limits the area available for the poles, it is convenient increasing w with respect to τ ;
- Given the maximum radius set to $r_{max} = 200 \text{ mm}$, a wide enough gap is ensured between rotating and fixed parts. This would lead 28.5 mm of security margin between the outer end windings and the flywheel inner surface;
- If w increases excessively with respect to τ there is a poorer utilization of the area, leaving more unused space between two single stators of the sub-machines.

A factor of utilisation is defined as the ratio of the active areas associated to the stators (thus subtracting the fraction accounting for the window between poles) divided by the annular area defined by r_1 and r_2 :

$$K_u = \frac{p w 2\tau - 2p\tau^2}{\pi(r_1^2 - r_2^2)} \quad (5.4)$$

The utilisation factor is important when dealing with stator layout tuning, as it directly impacts which magnitude of flux density is required in the air gap in order to satisfy levitation requirements.

A mean radius is also introduced, which is useful in torque-to-force conversions:

$$r_m = \frac{r_1 + r_2}{2} \quad (5.5)$$

After the decision of p , τ and w , other hypothesis concerning the winding exploitation are needed, together with all the material specifications and air gap assumption.

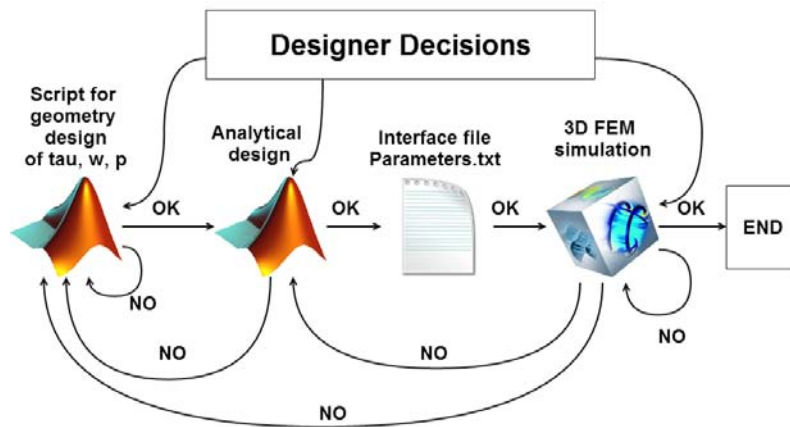


Figure 49: Design Flowchart.

Figure 49 describes the overall design procedure, from the analytical design to the 3D FEM control and final validation. The creation of a .txt file allowed to easily couple the two software, namely Matlab and Comsol Multiphysics.

5.3.1 Stator Layout Optimisation

The stator layout design can be seen as an optimisation problem, subject to constraints regarding the need to ensure no interference between adjacent sub-stators, together with specifications over the number of pole pairs. The outputs of major interest are K_u and the active area, referred also as objective functions. After a wide parametric sweep, the best solutions (i.e. configurations that maximizes an objective function, for a given r_{min}) are selected, for different values of p . Figures 50 and 51 show how both objectives have a unique maximum, where solutions with lower r_{min} than the one leading to the function maximum are discarded.

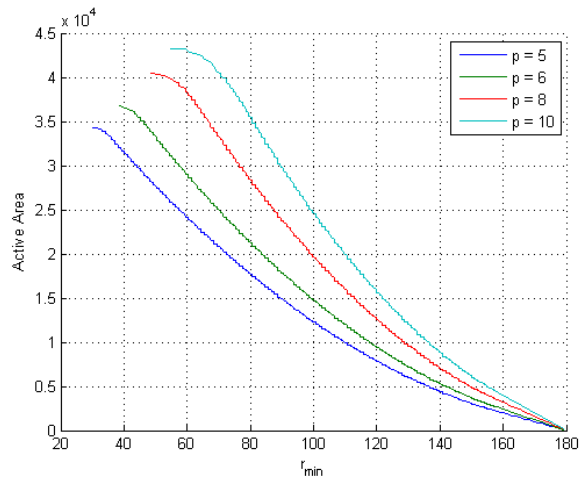


Figure 50: Active Area as a function of the inner minimum radius.

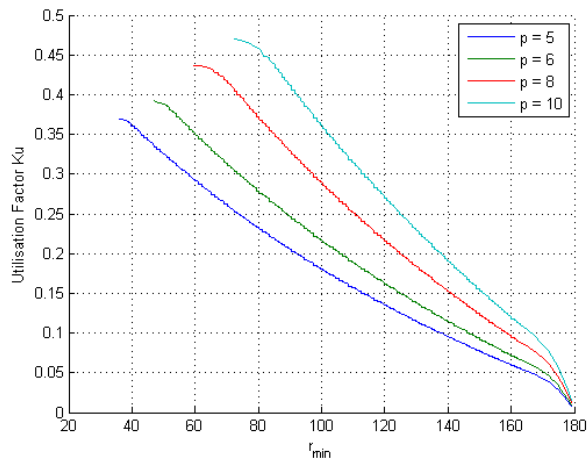


Figure 51: Utilisation Factor as a function of the inner minimum radius.

It should be pointed out that there is no guarantee that a solution that maximizes the active area, for a given r_{min} , is the same that maximizes K_u . For that reason, a sound evaluation should include the two objective functions within the same chart.

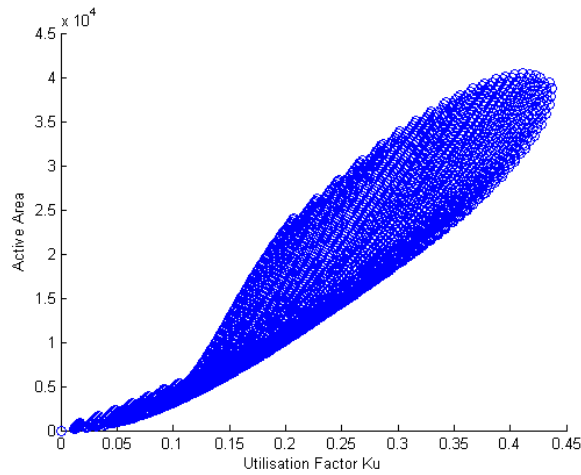


Figure 52: Active Area vs Utilisation Factor in the case of $p = 8$.

Considering a multi-objective optimisation approach, the Pareto frontier of fig. 52 is represented by the few solutions laying in the upper right part of the plot, the only ones that are not Pareto dominated by others. For different number of pole pairs p , it is obtained:

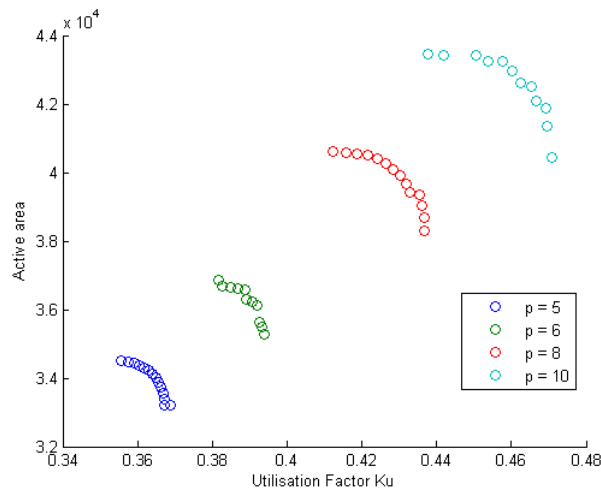


Figure 53: Pareto frontier in the case of different number of pole pairs.

Increasing the number of pole pairs has beneficial effects both on the active area and the utilisation factor, as fig. 53 shows, but it has to be considered a trade-off point of view in the choice of p , because of losses constraints. In our design example, let us choose $p = 8$, and one of the solutions laying in the middle of the associated red Pareto frontier. As a

consequence, Active Area has value of $4.01 \cdot 10^4 \text{ mm}^2$ and a K_u of 0.429. Geometrical sizes providing these outputs correspond to $\tau = 28\text{mm}$ and $w = 117.5\text{mm}$. A view from above of the optimized geometry is hereby presented:

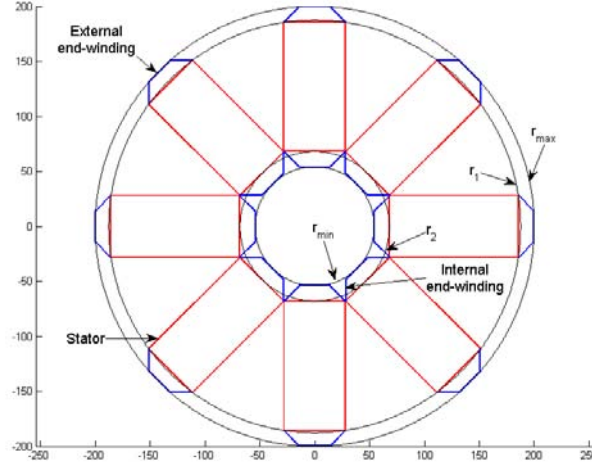


Figure 54: Matlab optimisation output of stator layout in case of $p = 8$.

After this process has been carried out, the stator main dimensions are given, and the design of the permanent magnet and the slots are the following steps to be undertaken, according to torque and levitation requirements.

Due to the geometry arrangement, during the track rotation the area that couples stator and rotor track varies, diminishing to its minimum in occasion of the middle position (22.5° with respect to stator, as in fig. 55c). Hence the machine average performances can be achieved only by the requirement of an increasing factor in levitation and thrust force exerted in case of perfect alignment between stator and track, defined as:

$$K_m = \frac{2l_p \tau}{A_m} \quad (5.6)$$

where A_m represents the area coupling stator and rotor track, averaged throughout the track rotation and $2l_p \tau$ is its maximum value attainable. Figure 55 highlights in blue the evolution of the aforementioned area, numerically represented in fig. 56.

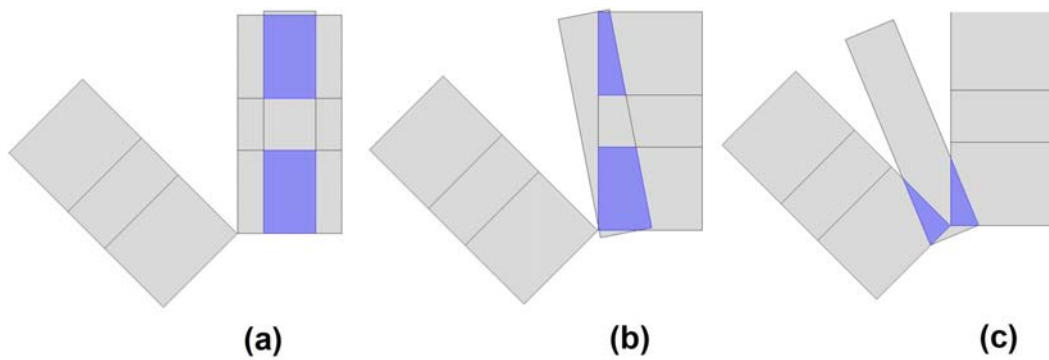


Figure 55: Different rotor positions and the associated coupling area.

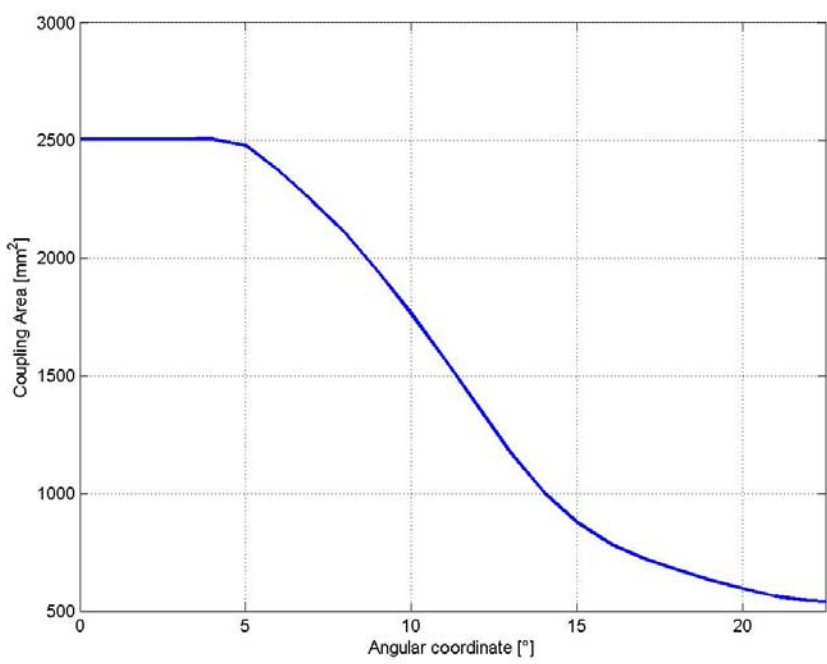


Figure 56: Angular trend of the coupling area, from zero to 22.5° of track rotation.

For the chosen geometry K_m has value 1.603, hence machine performances are increased of 60.3% with respect to average, in case of perfect alignment as in fig. 55a.

5.4 Permanent Magnet and Slot Design

Concerning the flux leakages estimation, as pointed out previously (see figure 34b) no lateral flux dispersion lines were assumed across the azimuthal section. As this is not the case, additional leakage must be considered and coefficient K_l in equation 4.23 is assumed to be:

$$K_l = 0.85 \quad (5.7)$$

The 15% flux reduction introduced has been set after performing FEM 3D simulations that outlined values from 10 to 15%, for a geometry that is reasonable, i.e. sufficiently closer to the optimised one. It is intuitive that this share of flux leakages are proportional to the extent of w with respect to 2τ .

Concretely, a Matlab script has been developed which requires as input a set of data, ranging from stator dimensions, across magnet properties, to machine requirements:

- Levitation force $F_l = 10kN/n_{mp} = 417N$;
- Thrust force F_t , or the required torque: $T = F_t \cdot r_m/n_{mp} = 0.208Nm$;
- Stator depth $w = 117.5mm$;
- Pole pitch $\tau = 28mm$;
- Number of machines $n_m = 3$;
- Number of pole pairs $p = 8$;
- Air gap $g = 1mm$;
- Average coupling area coefficient $K_m = 1.603$;
- Number of slots per pole and phase $q = 1$;
- Rated current density in armature winding $J_a = 4.5 \frac{A}{mm^2}$;
- Filling factor of armature slot $K_{fill} = 0.55$;
- Armature slot width $w_s = 1.5mm$;
- Ratio between slot height and pole height $\frac{h_p}{h_s} = 2.5$;
- Magnet residual magnetization $B_r = 1.2T$;

- Magnet recoil line permeability $\mu_r = 1.1$;
- Minimum magnet aspect ratio $M_{ratio}^{min} = 0.1$;
- Rotor track height h_{rt} , such that an average magnetic flux density of 0.8 T is achieved in the central, vertical cross section of track.
- Electric angle between induced emf and current, in case of nominal torque produced: $\gamma = 5^\circ$;

Acquired that specifications, after an iterative process (because of the geometric influence over flux leakages) it is calculated the amount of Ampere-turns required for torque purposes and the magnet volume, as a function of its aspect ratio. Figure 57 shows as the correct choice of magnet sizes can lead to a substantial decrease in the overall volume.

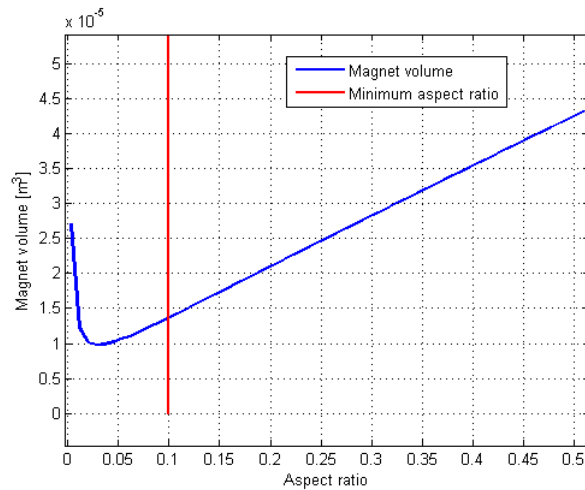


Figure 57: Magnet aspect ratio optimisation.

The automated procedure in this case has chosen a $M_{ratio} = 0.1$, as the point of minimum magnet volume violates the aspect ratio constraint. Another aspect to be considered when dealing with low M_{ratio} is the implied increase of back iron height h_{bi} , thus requiring a wide amount of SMC material and partially vanishing the magnet cost reduction. An adequate economic optimisation will require detailed cost specification of the two materials, and it is beyond the scope of the treatise.

Slot presence is kept into account throughout the design: g_{eq} in place of g is used in the evaluation of per unit parameters K_{t1} and K_a . In this way additional leakages caused by the slots are evaluated, even if not on a detailed approach as a FEM one.

The geometric dimensions obtained are synthesized in table 18, rounded if necessary.

r_1	r_2	r_3	r_4	r_m	r_{max}	r_{min}	τ_t	w_s
187.6	73.5	68	55.8	130.6	200	54	9.3	1.5
w_t	h_s	h_p	l_{mag}	h_{bi}	l_p	w	τ	g
7.8	3.9	9.8	3.3	33.4	44.8	117.5	28	1

Table 18: Summary of the optimisation output. All dimensions are in millimeters.

Also other variables are of interest, as the ones in tab. 20:

K_c	$W_1 I_1$	Φ_{mag}	Φ_g	$K_l \cdot K_\Phi$	B_g
-	[A]	[mWb]	[mWb]	-	[T]
1.037	14.5	1.73	1.02	0.592	0.816

Table 19: Electrical, magnetic and dimensionless variables calculated.

The slot layout is then manually modified because of its low section, which implies the use of only a few wire turns (fig. 58). It is chosen a copper diameter of 1 mm, hence 1.094 mm taking into account also the insulation coating. The wire has conductive cross section of 0.7854 mm² and $r_1=21.76 \text{ m}\Omega/\text{m}$ of resistance per unit of length.

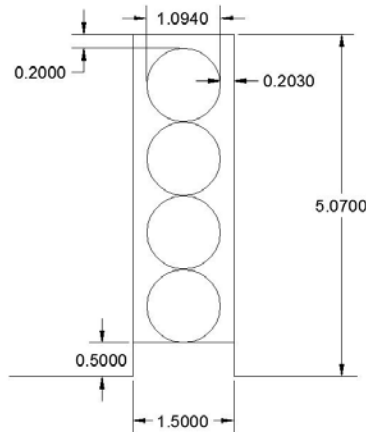


Figure 58: Proposed slot, insulation and copper wire sizes.

As a consequence, four turns would lead to a slot copper section of 3.14 mm² and 4.62 A/mm² of current density. Moreover, insulation paper from wire to slot of 0.15 mm thickness and 0.5 mm of free space for the slot wedge are introduced.

w_s [mm]	h_s [mm]	J_a [$\frac{A}{mm^2}$]	K_{fill} -	A_s [mm ²]
1.5	5	4.62	0.419	7.5

Table 20: Updated slot parameters.

The parametric model built into the FEM software is the following:

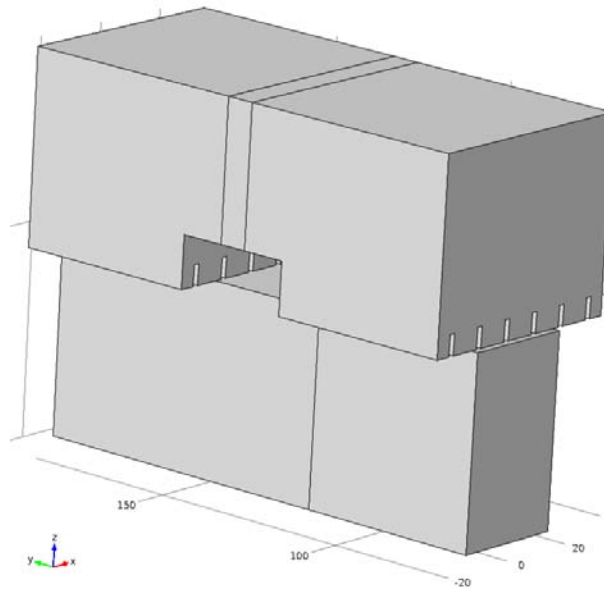


Figure 59: Rendering of the optimised geometry.

The rotor track height $h_{rt} = 45.7mm$ has been designed superimposing an average magnetic induction of $0.8T$, in order to keep reasonable values of losses. Notice that the track itself is divided into two parts, that has been made only to achieve an easier evaluation of the flux reaching the air gap.

Chapter 6

FE Analysis Verification

The chapter includes a comprehensive validation of the outputs proposed by the analytical model, by mean of 3D FEA techniques, outlining the level of agreement between the two and describing the major results found.

6.1 FEM Exterior Box Influence

A non trivial problem when dealing with 3D FEM simulations is represented by the trade off in the choice of an adequate external box dimension, where to apply boundary conditions. As in our case the flux share that is closed through air is considerable, probably there will be the need of an extensive amount of elements describing the air surrounding the machine (fig. 60). The major drawback is represented by increased computational times, as well as the risk of simulation failure due to insufficient RAM memory.

The commercial software adopted is Comsol Multiphysics, in particular the AC/DC set of physics have been used. A detailed meshing of the single domains has been carried out, in order to exploit at its best the computing capabilities of the machine, and avoid unnecessary excessive meshing where not needed. particular impact over the total number of elements is led by the *maximum element growth rate* set in the air domain: it rules the maximum ratio between dimensions of adjacent elements, for example a growth rate close to one would force the mesh to "grow" slowly from a region where small elements are present toward the exterior box. As no currents are considered up to now, a formulation with a scalar magnetic potential is advisable and then adopted, because it divides by three the RAM requirement with respect of a solution with full magnetic vector potential.

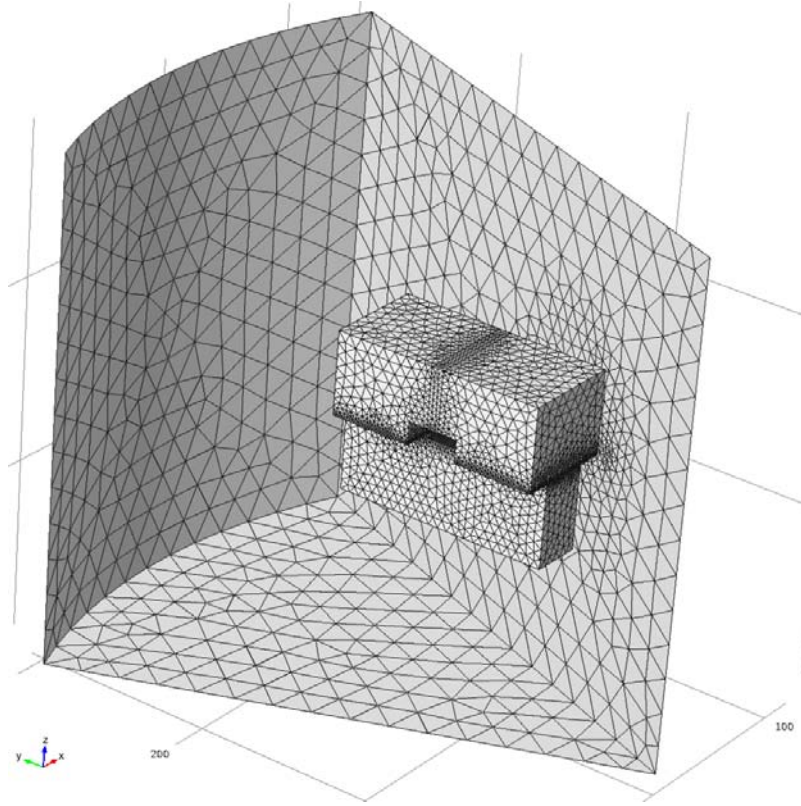


Figure 60: Meshing of the domains.

In order to evaluate the effect of the exterior box, a parametric variation of its dimensions is performed and a crucial performance index, the levitation force, is measured. Electromagnetic forces magnitude are particularly sensible to the solution, as they depend on B^2 . Due to the geometry configuration, only 1/8 of the machine is studied, relying on periodic boundary conditions on the exterior box lateral surfaces. Computational detail of the simulation involves around 300k elements and 350k dof (degrees of freedom) solved, where the shape functions are Lagrangian of second order, as the software default. The variation of the box size is obtained through a K_{box} coefficient that multiplies its two editable sizes: height and extension toward the external radius. A range from 0.8 to 2 is introduced, graphically visible in fig. 61. As the outside box dimension increases, it is expected a reduction in the levitation force, because the leakage flux lines are less constrained to close on a path adjacent to the magnetic core. An asymptote is evident in fig. 62, hence considered the trade off between computational cost and results accuracy, it is chosen $K_{box} = 1.4$ as valid for the future simulations.

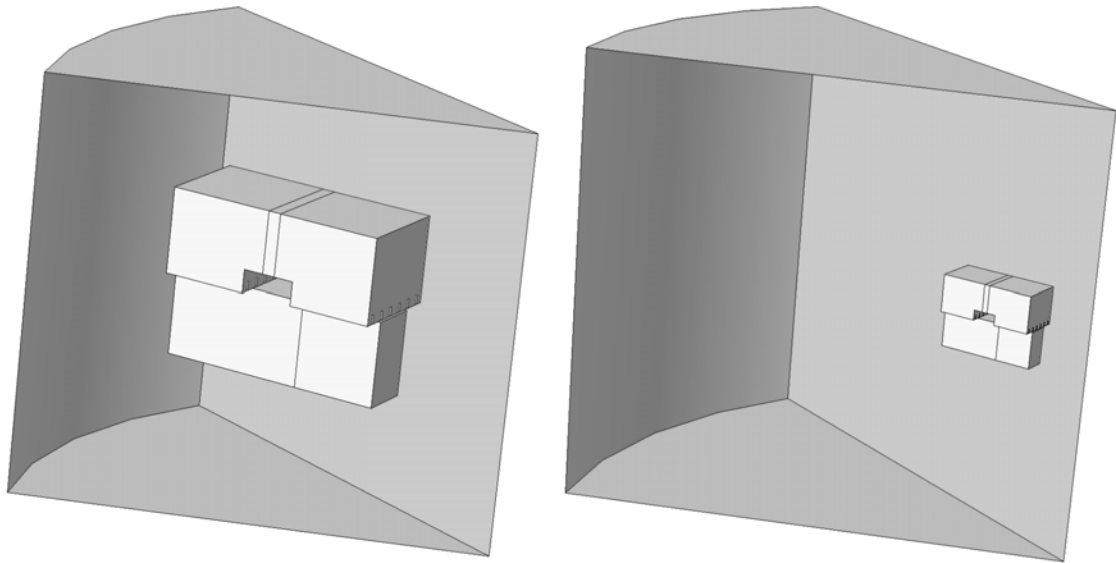


Figure 61: Box dimensions variation amplitude, from $K_{box}=0.8$ to $K_{box}=2$.

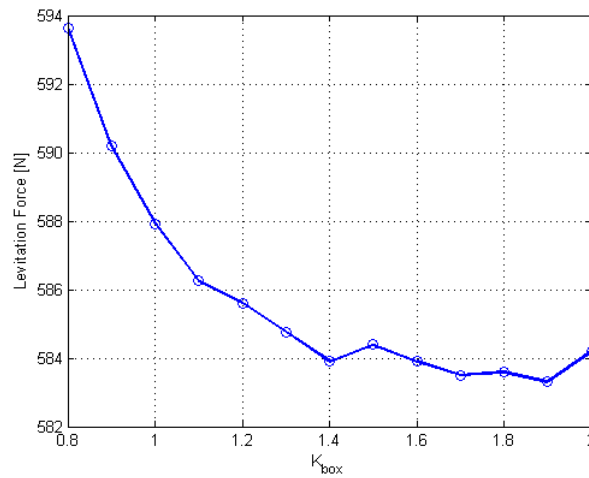


Figure 62: External box influence over the quality of results.

Given the calculated levitation force of 584 N, it is lower than the expected: for each stator, in case of perfect alignment with rotor, the force that has to be exerted is

$$F_l = \frac{F_l \cdot K_m}{n_m p} = 668N \quad (6.1)$$

which means a lack of 12.5% with respect to the expected one. Multiple

factors can be held responsible of this difference and will be investigated in the following pages, however the analytical method provides a satisfying starting point, allowing to rely on FEM 3D simulations only for successive refinements.

6.2 No-load Results

The configuration without armature current is analyzed, comparing the results led by the simulation against the expected values derived from the analytical model.

	Φ_{mag} [mWb]	Φ_g [mWb]	F_l [N]	Φ_g/Φ_{mag} -	B_g [T]
FEA 3D	1.65	0.996	584	0.603	0.795
Analytical	1.73	1.02	668	0.59	0.816
Difference	-4.6%	-2.4%	-12.6%	+2.2%	-2.6%

Table 21: Comparison between outputs of the two methods. B_g in the FEA computation is achieved by averaging only the z component of flux density.

The table shows some interesting aspects: first of all the magnet flux is lower than expected, thus the real magnetic circuit encountered by magnetic flux lines has higher reluctance than the estimated one. As in the analytical model the magnetic core reluctance has been neglected, this was an expectable result, especially because of the relatively low magnetic permeability of SMC materials with respect to iron cores. A second aspect found out is the minor dispersion of magnetic flux lines, compared to what estimated through analytical methods. Deeper investigation concerning flux leakages is required in order to determine where the two models differ.

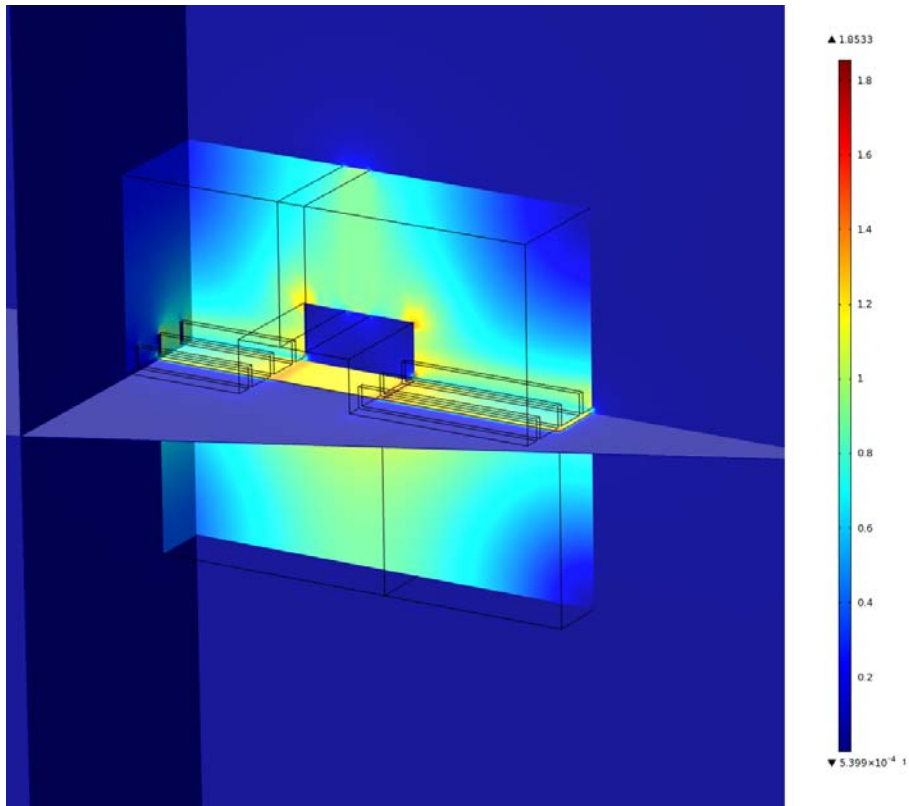


Figure 63: 3D sections for the no-load situation. Color map is calibrated according to the magnetic flux density magnitude.

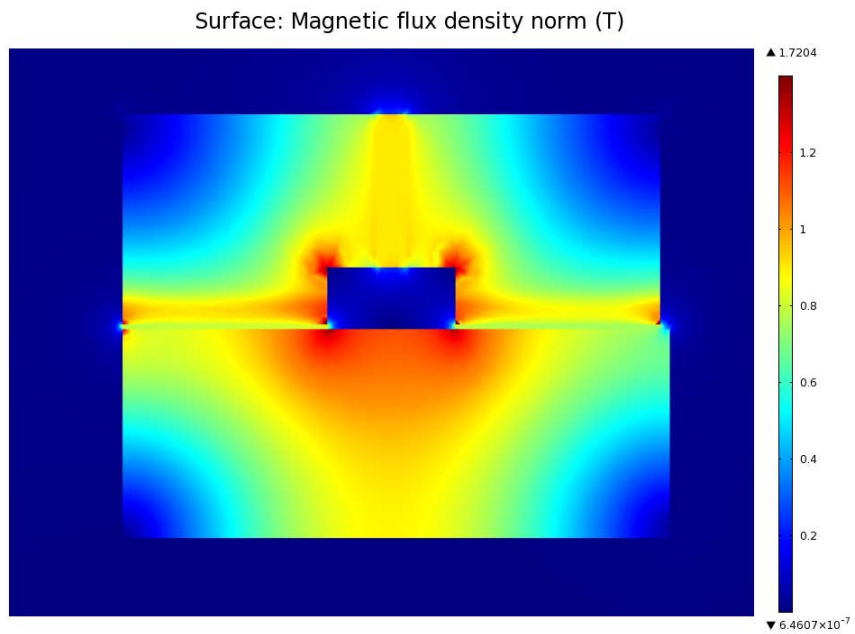


Figure 64: Transversal section display of magnetic flux density magnitude.

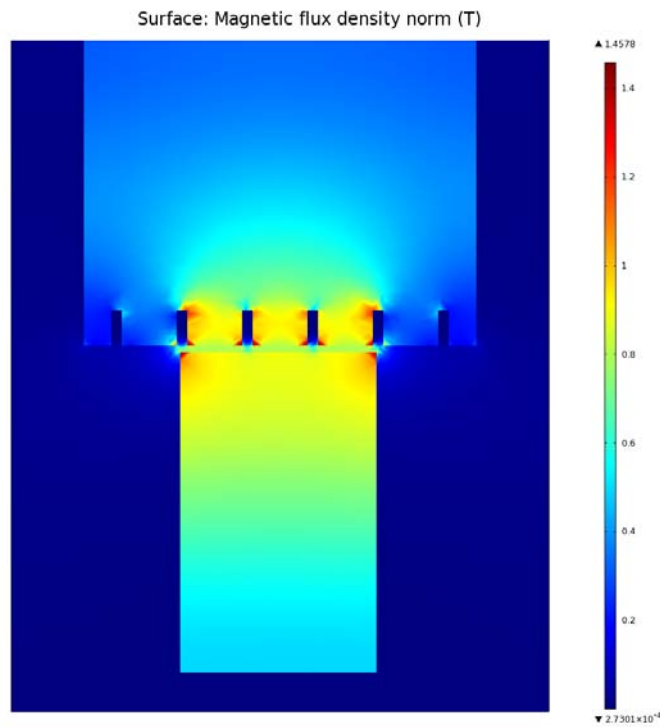


Figure 65: Azimuthal section display of magnetic flux density magnitude.

Relative permeability maps are important in the evaluation of SMC saturation along the geometry. As in fig. 67 and 66, apart from curvature edges and stator teeth the overall grade of material saturation is quite low, given the maximum relative permeability of $\mu_r \approx 800$:

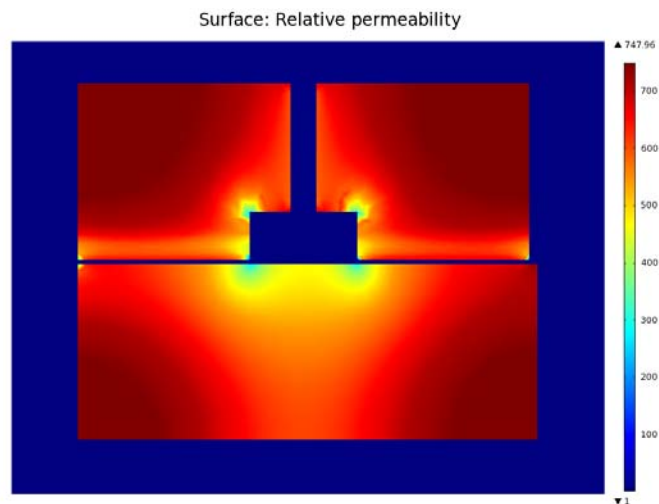


Figure 66: Transversal section display of relative permeability.

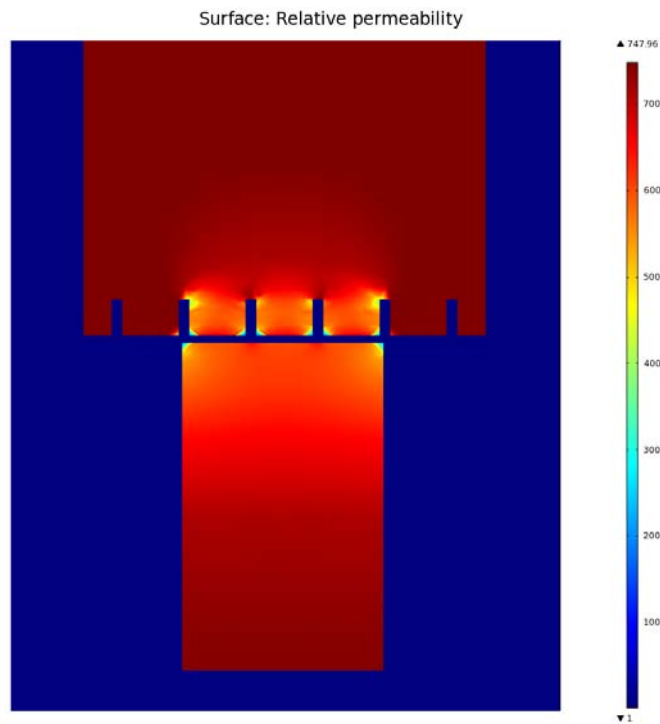


Figure 67: Azimuthal section display of relative permeability.

Another interesting plot consist of the investigation of flux dispersions, operating a flux computation of the magnetic flux density, for every surface of the geometry.

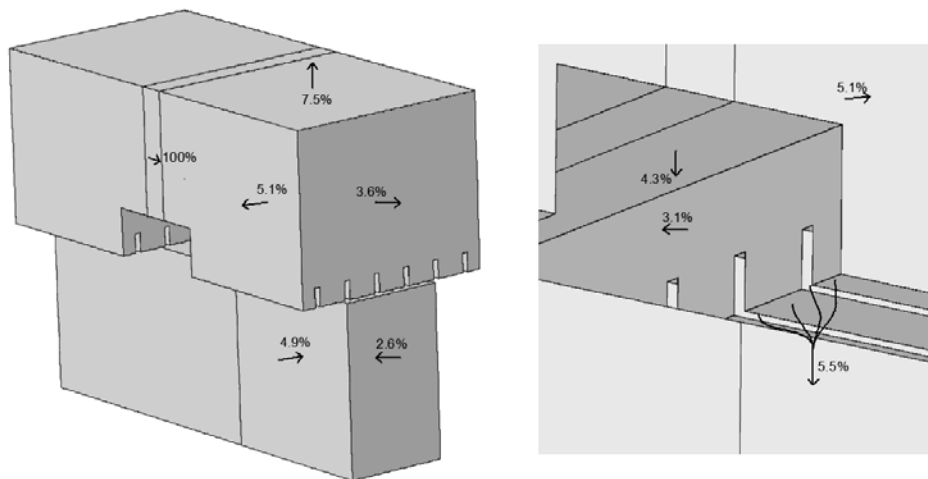


Figure 68: Percentages of flux dispersion. On the right, a zoom on the window between poles.

Assuming as 100% the flux produced by the magnet, it has been investigated the flux leakage distribution through different sections. The various contributions are evidenced in fig. 68, where it can be noticed how the assumption of $K_l = 0.85$ has demonstrated to be too conservative: indeed the flux leakage on the stator lateral face has percentage value of 5.1%, hence 10.2% considering the both sides.

6.2.1 Levitation Force dependence upon Angular Position

This section aims to evaluate how the levitation force varies as the flywheel spins, and whether the hypothesis of reaching a desired average levitation force thanks to the chosen performances increment of K_m is sound or not. A detailed simulation, involving the solution of a set of 1.25 M dof simulations on an 8 GB RAM machine, allowed to properly represent the multiple stators and tracks presence. In this way, the track located in the center doesn't suffer significant border effects led by the stators on the external positions:

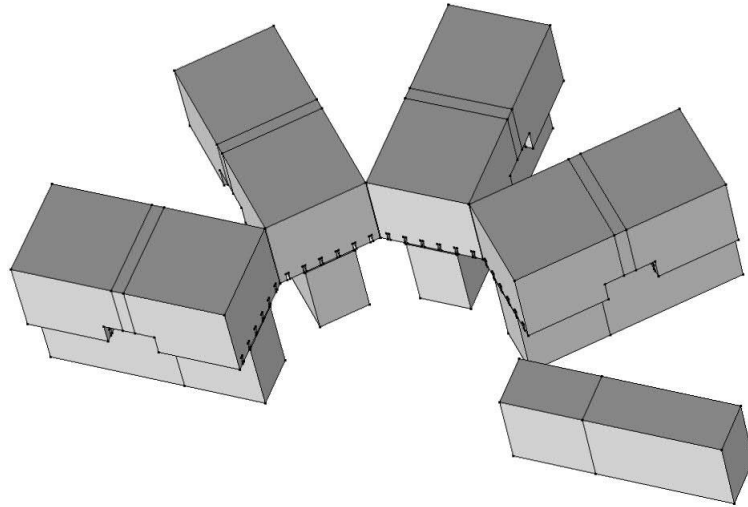


Figure 69: Layout comprising a wider extension of the geometry.

The average force is lower than expected, namely 380 N in place of

$$\bar{F}_l = \frac{10kN}{n_m p} = 417N \quad (6.2)$$

It is noticed a flux concentration in case of small air gap area (see fig. 71) during the crossing of a track from one stator to the following, hence

relatively high values of B are implied, and high force values as well, quadratically related to the flux density.

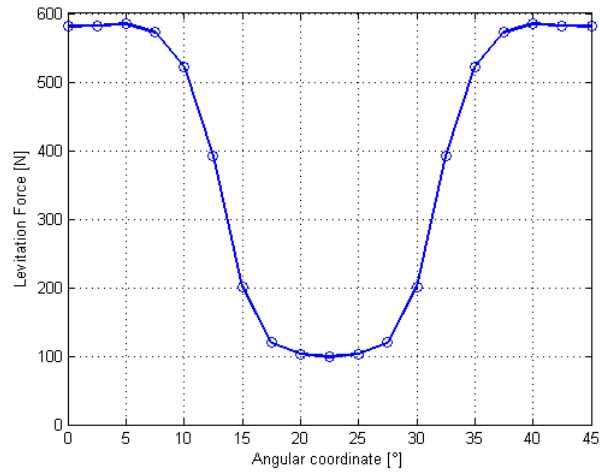


Figure 70: Levitation force dependence over rotor position, in the case of multiple adjacent stators.

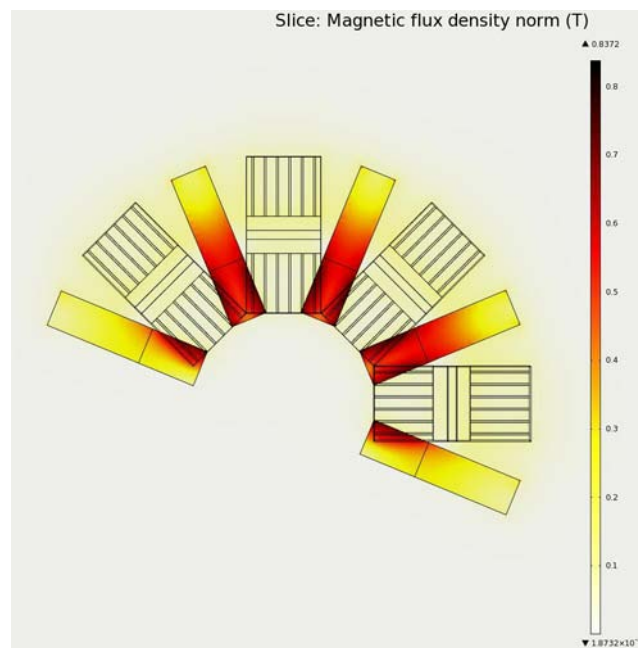


Figure 71: Magnetic flux density concentration in the machine inner part as the rotor tracks pass from a stator to the following one. The section plane height is chosen in order to show a rotor track cross section.

In order to evaluate the flux concentration contribution to the average levitation force, it has been normalized on a 0 to 100 basis the angular evolution of coupling area and levitation force, as in fig. 72.

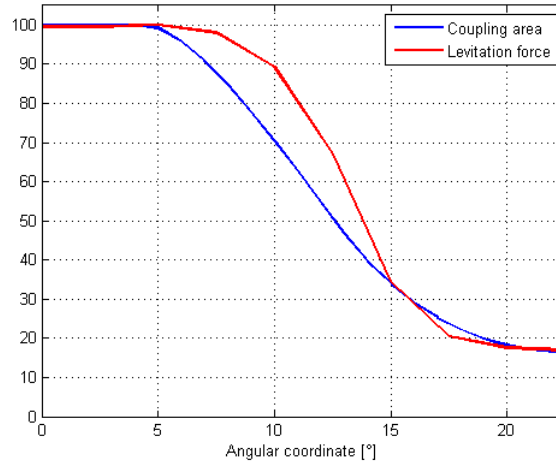


Figure 72: Normalized levitation force and coupling area dependence over rotor position.

On average terms it is noticed how the flux concentration increases the magnetic flux density within the coupling area air gap, implying a levitation force which is higher than the one predictable assuming a constant air gap flux density as the rotor shifts.

6.3 Stability

Dynamic control of the levitation is crucial for the machine proper functioning. Depending on the geometry, magnetic levitation devices have some directions on which they show intrinsic stability, whereas on others they don't and in turn they need feedback based controls in order to keep the desired position. Given the geometry analyzed in fig. 73, it is possible to simulate slight deviations of the rotor with respect to the perfectly centered position and see the electromagnetic forces involved. The stability along z can be easily evaluated by mean of a single stator, relying on periodic boundary conditions.

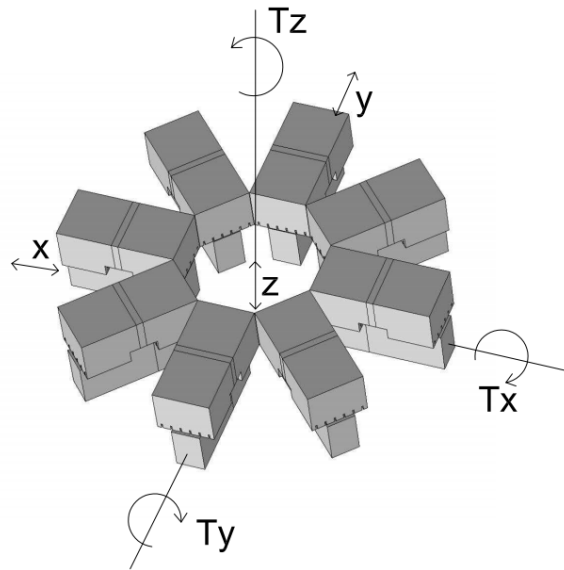


Figure 73: Complete geometry, with axes and torque reference system.

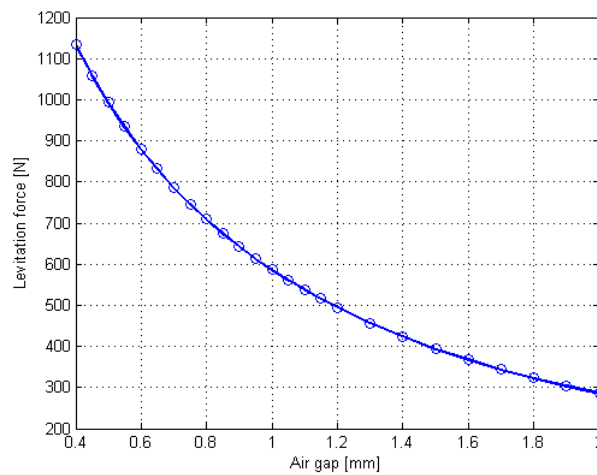


Figure 74: Levitation force as a function of air gap deviations. Positive deviations imply air gap reductions.

In our case, a control over the air gap magnitude (z direction) is needed, as fig. 74 shows: different air gap magnitudes are evaluated, in the case of rotor track aligned with the stator.

For the purpose of stability evaluation along x, a whole machine is considered, rather than a single rotor track. Hence the term rotor will refer to the set of rotor tracks expected to be rigidly connected one another.

Lateral (x and y directions) stability is ensured by the minimum magnetic energy point achieved by the rotor tracks if located under the poles:

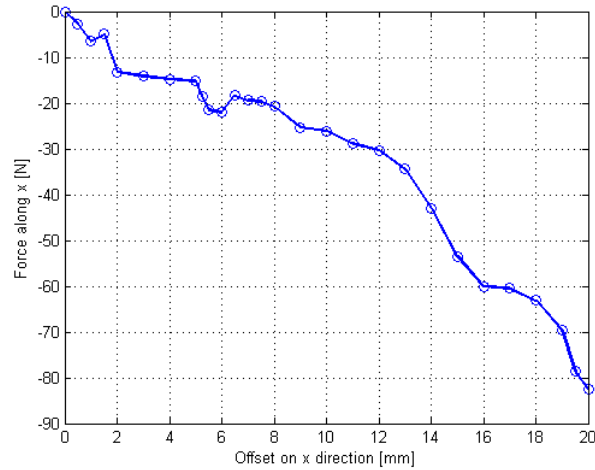


Figure 75: Stabilizing force in case of an offset across the x direction.

Due to the geometry symmetry, an offset along y would produce the same results and is thus not investigated. Fig. 75 shows the presence of irregularities in the stabilizing force, probably held by the armature slots presence.

Concerning rotations along T_x or T_y , the stability is in general not satisfied, but proper winding connection can provide artificial methods to ensure it anyway. Parallel connection of armature windings is adopted in many electrical machines, where an air gap regulation due to rotor out-of-center position is necessary. As soon as a rotation is verified, air gap asymmetry is the direct consequence, leading to the definition of two opposite zones, as described in fig. 76. For zone 1, the air gap is reduced and there is an increase in its magnetic flux density, leading to a higher voltage collected by the stator winding. The opposite is true for zone 2. If no corrective action is undertaken, this is a non stable configuration and the electromagnetic torque developed by the present configuration would act to magnify the effect, leading to a destructive contact between stators and tracks. However, in analogy to the treatise concerning parallel connection of transformers, a circulating current I_c is produced in light of the different voltages of the two windings. I_c is ruled by the magnitude of voltage difference, as well as by the machine parameters, summarized in the figure through an R-L branch. The magnetic effect of the circulating current is such to drive back the stator to the desired position: it enhances

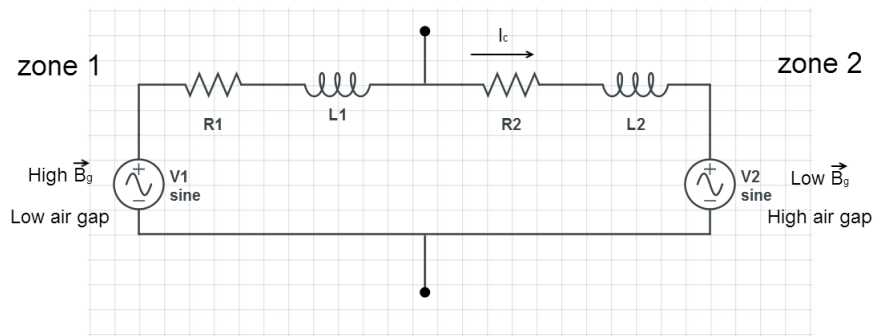


Figure 76: Circulation current caused by air gap asymmetry consequential to a rotation along T_x or T_y .

B_g in zone 2 and reduces it in zone 1, creating an electromagnetic torque acting in a stabilizing direction. In the specific design instance, the so called "number of parallel paths" can be raised up to 8, connecting all the stators in parallel.

6.4 Cogging Torque

For a single rotor track, the cogging torque in case of armature current absence is evaluated. For the electrical machines it is generally difficult to accurately evaluate the cogging torque evolution through FEA, being it a variable of limited magnitude with respect to other forces/torques involved. In order to cope with it, an accurate meshing of the domains is necessary, particularly concerning the air gap. A commonly used technique comprises the introduction of additional fictitious geometries (in-built with the stator) in the air gap, superimposing a constant mesh distribution along them. Consequently, the share of air gap that suffer numerical errors as the rotor shifts is lowered and a significant difference can be noticed in fig. 77.

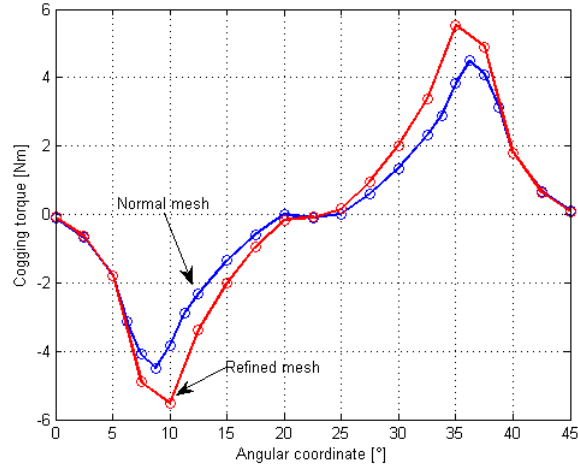


Figure 77: Cogging torque as a function of the angular coordinate, for different levels of mesh refinements.

6.5 Machines Angular Shift

The levitation force showed to be non constant, hence vibrations along z of the flywheel are expected. Contextually there is interest in the mitigation of cogging torque. A reduction of both can be made by mean of an angular shift between the three main machines. A parametric analysis is applied, evaluating multiple cases and considering one machine as reference, the other two are shifted of an angle α_d and $2 \cdot \alpha_d$ respectively, thus offering a degree of freedom where to act. As the single machine force waveform is periodical, the shift has no influence over the average force and torque, but only on their point-to-point evolution. Concerning the levitation force, its variation measure adopted is the standard deviation, defined as follows for a generic array of values:

$$\sigma_x = \sqrt{\frac{\sum_{i=1}^N (x_i - \bar{x})^2}{N}} \quad (6.3)$$

being N the number of array elements, x_i the i -th array element and \bar{x} the array arithmetic average. A better understanding of the uneven force magnitude is then obtained in terms of percentage standard deviation (fig. 78) with respect to the average levitation force. On the other hand, similar findings are related to the cogging torque: because of its zero mean value, another metric is introduced in order to quantify the torque magnitude,

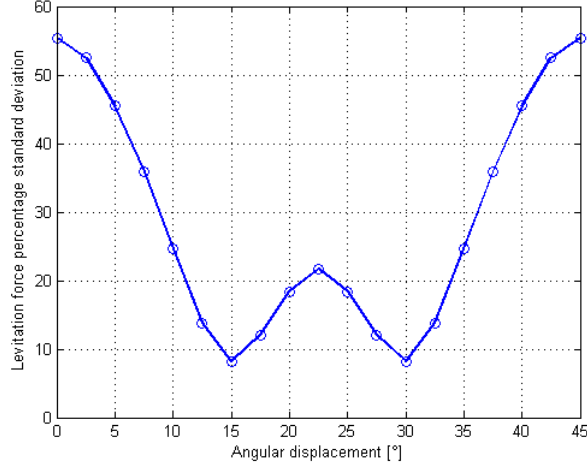


Figure 78: Percentage standard deviation of levitation force, as a function of the angular shift.

hence the absolute average is considered. Fig. 79 shows how two ideal positions arise also concerning the cogging torque reduction.

Two equivalent skewing configurations have been chosen as a compromise between the two goals:

- 2nd machine: 15° and 3rd machine: 30°
- 2nd machine: 30° and 3rd machine: 60°

Hence, once adopted one of the two it can be displayed the force distribution given by the sum of the three machines, which rules the flywheel movement along z direction, augmenting or decreasing the air gap.

Over 360° the sum of the three machines force contribution is presented in fig. 80. Indicating P_z the rotor coordinate, F_g the flywheel gravitational force and a_z the flywheel acceleration component, both along z, the dynamic condition is governed by the equation:

$$F_l + F_g = a_z \quad \frac{d^2 P_z}{dt^2} = a_z \quad (6.4)$$

and therefore, given a force distribution represented by fig. 80 and considering the worst case for what concerns vibrations, i.e. low rotational speed (the amplitude of rotor position deviation is increased if the flywheel spins slowly), at 8000 rpm a single turn is completed in

$$\frac{1}{\frac{8000}{60}} = \frac{60}{8000} = 7.5ms \quad (6.5)$$

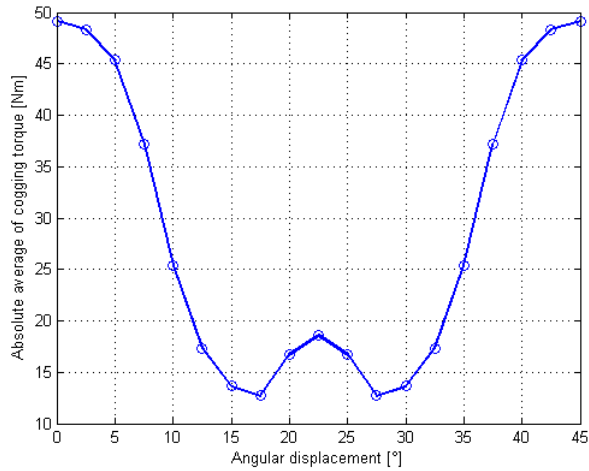


Figure 79: Absolute average of cogging torque, as a function of angular displacement.

and Simulink allows to simply elaborate the rotor deviation position, given the input array containing the force evolution as a function of time by mean of the scheme in fig. 81. The flywheel gravitational force is here assumed as the mean of the magnetic force, namely 9.108 kN, in order to estimate the air gap deviations produced by the levitation force ripple.

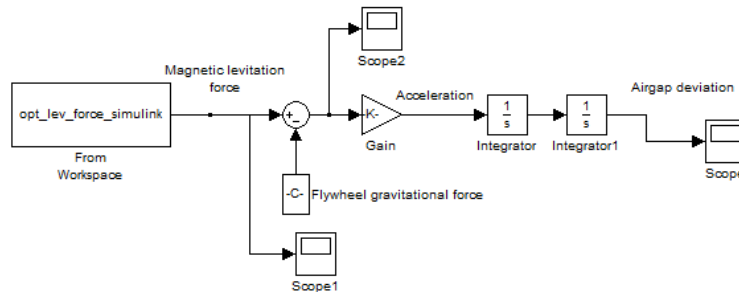


Figure 81: Simulink model developed to evaluate air gap deviations due to levitation force ripple.

For a single turn, air gap deviations of about 5 nm are obtained, meaning that flywheel inertia has a definitely predominant behavior on the dynamic evolution along z axis.

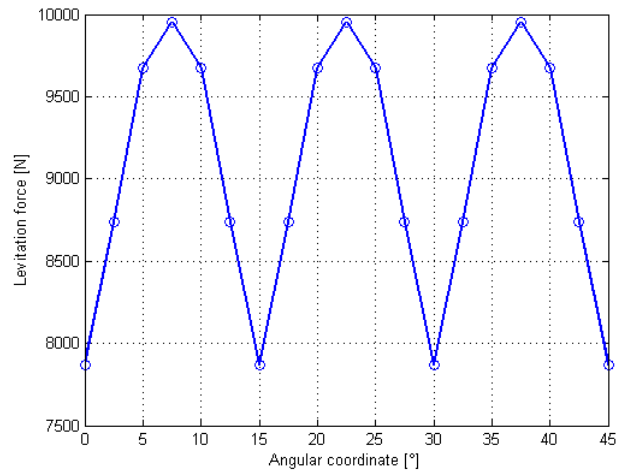


Figure 80: Optimal resulting force.

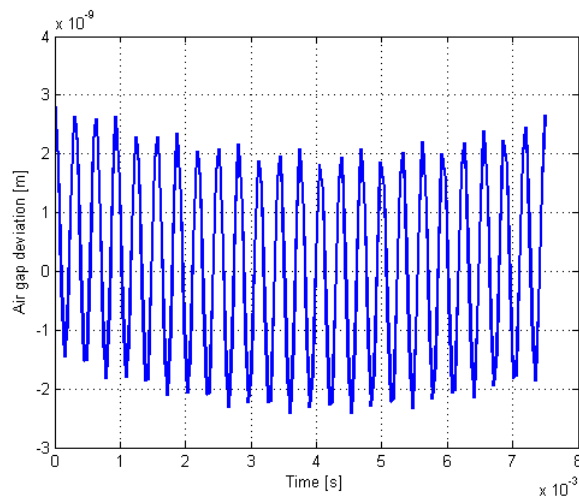


Figure 82: Rotor vertical position evolution, for a single turn while rotating at 8000 rpm.

Concerning the cogging torque, a comparable process is carried out leading to the following optimised torque evolution, comprehensive of the three shifted machines effect:

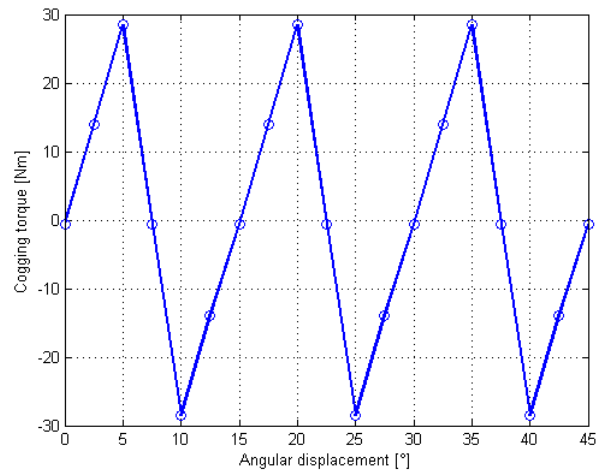


Figure 83: Optimal cogging torque.

Finally the cogging torque rotational speed effect can be evaluated (fig. 84) and it can be concluded that this aspect is considered to be non binding throughout the design process, given the high flywheel momentum of inertia.

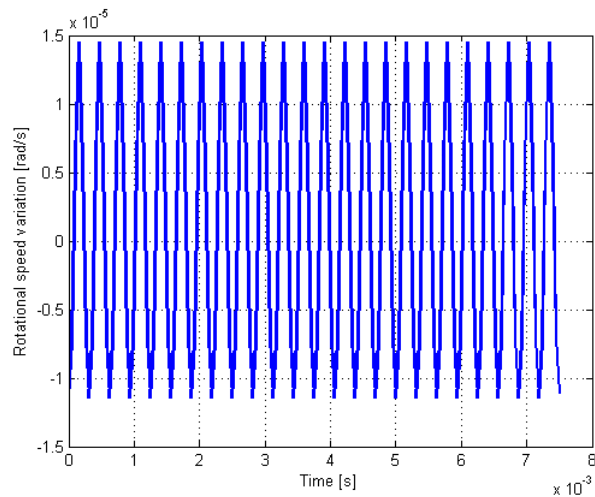


Figure 84: Rotational speed evolution, in case of no load and assuming an initial speed of 8000 rpm.

The major drawback of the angular shift design choice lays in the need of separated inverters to feed each of the three machines, resulting in increased costs and need of multiple controls.

6.6 On-load results

In order to correctly represent the on-load situation, a detailed armature winding modeling is introduced (fig. 85).

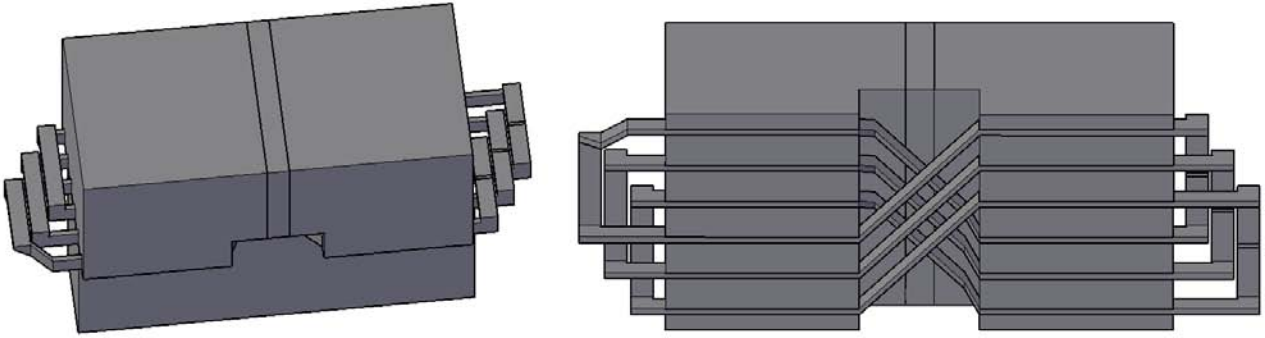


Figure 85: On-load 3D CAD representation. On the right, a view from the bottom, in absence of the rotor track.

Then, as done in the no-load case, periodicity boundary conditions are applied on the exterior box surrounding the geometry.

6.6.1 Parameters Evaluation

The resistance computation can be analytically expressed in a couple of equations: the length of an armature turn is

$$L_t = 2[2(lp + \tau \sqrt{2})] = 0.337m \quad (6.6)$$

hence, the phase resistance has value

$$R_1 = W_1 L_t r_l = 29.3m\Omega \quad (6.7)$$

Concerning the inductances calculations, a FEA approach is selected. First of all the permanent magnet residual magnetization is set to zero, then a set of currents is injected, whether of d-axis or q-axis. As in [37], in case of low saturation of magnetic core, the inductance of a three phase winding among an x-axis (being x correspondent to d or q) can be calculated through

$$L_x = \frac{4 E_m}{3 \hat{i}^2} \quad (6.8)$$

where E_m is the magnetic energy and \hat{i}^2 represents the squared peak value of the three phase system of currents injected. In the FEM software the

current value has to be multiplied by W_1 in order to get results accounting for the number of turns. As a way to prove the non excessive saturation of the magnetic circuit, the sum of magnetic energy E_m and coenergy C_m can be computed by mean of an integration throughout all the domains:

$$\iiint_V \mathbf{A} \cdot \mathbf{J} dv = E_m + C_m \quad (6.9)$$

in the linear case, $E_m = C_m$.

As in the computation are included also leakage fluxes, for the d-axis it is obtained:

$$L_s + L_d = \frac{4 E_{md}}{3 \hat{I}^2} = 11.2 \mu H \quad (6.10)$$

for the q-axis:

$$L_s + L_q = \frac{4 E_{mq}}{3 \hat{I}^2} = 26.9 \mu H \quad (6.11)$$

being L_s the leakage inductance. Different values concerning d and q inductances are in agreement with previous research [38, 39], and also the higher value of q inductance is confirmed.

The angular frequency of electrical voltages and currents, for the maximum and minimum rotating speed are:

$$\omega_{max} = 13400 \text{ rad/s} \quad \omega_{min} = 6700 \text{ rad/s} \quad (6.12)$$

hence by multiplying an inductance for an angular speed, it is obtained the reactance value for the given axis, for the specific rotation regime.

6.6.2 Induced Voltage

Concerning the induced voltage, an accurate evaluation can be achieved by mean of the flux linkage on a single phase of the armature winding, and its fundamental component (fig. 86). The magnet has the major contribution in terms of flux, hence the analysis conducted neglecting the effects on linked flux by the armature current has sufficient validity also in on-load situations.

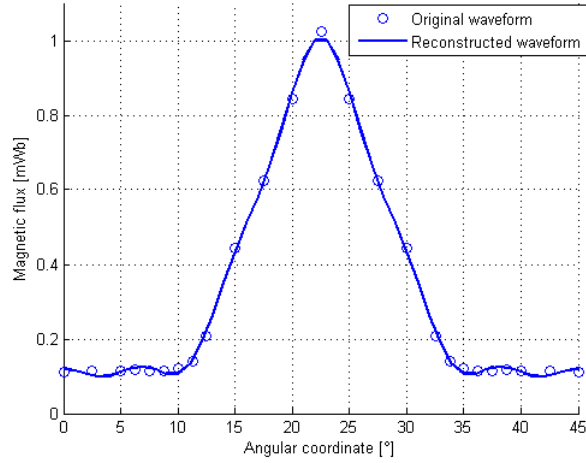


Figure 86: Flux linkage on an armature phase (only one turn is considered), and its reconstruction from Fourier's analysis.

Due to the homopolar configuration, a non zero mean value is found also in the flux linkage, and its associated Fourier harmonic spectrum is obtained in fig. 87.

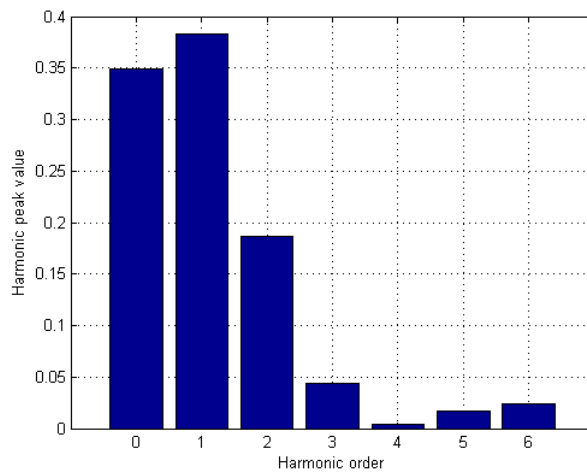


Figure 87: Harmonic spectrum of the magnetic flux.

the fundamental has peak value of $\hat{\Phi}_1 = 0.383mWb$, hence the fundamental rms induced voltage in case of maximum and minimum rotating

speed becomes respectively:

$$E_{1max} = 2\omega_{max}W_1 \frac{\hat{\Phi}_1}{\sqrt{2}} = 29V \quad E_{1min} = 2\omega_{min}W_1 \frac{\hat{\Phi}_1}{\sqrt{2}} = 14.5V \quad (6.13)$$

where the '2' factor arises from the fact that only a pole out of the two was considered in the flux computation.

The point-to-point evolution of the induced voltage can be calculated by mean of the magnetic flux derivative. In light of this operation, flux components with harmonic order higher than one are multiplied by their harmonic order. As a result an important share of the voltage waveform is composed by higher harmonic terms:

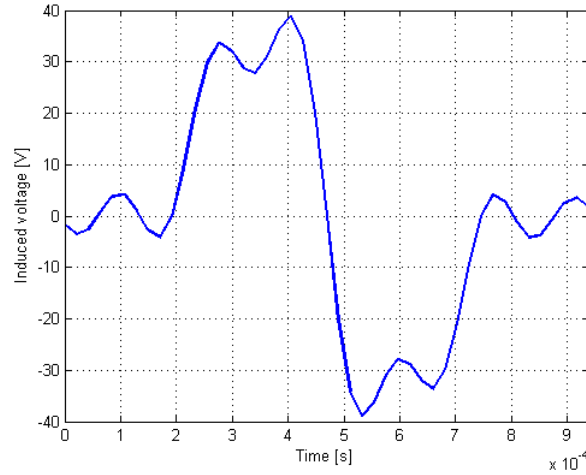


Figure 88: Induced voltage in case of a rotational speed equal to 8000 rpm.

6.6.3 Torque Calculation

In case of full load and minimum speed, the average torque expected to be produced by a single stator is $T = 0.208Nm$, whereas the cogging torque reaches values up to $4.5 Nm$, with a ratio between the two attaining 21.6. It is therefore very difficult to evaluate numerically the torque contribution given by the stator current, given the predominant cogging effect. A simplified analysis is therefore introduced. Considering only a rotor, the torque can be calculated through the energy conservation:

$$T = \frac{3E_{1min}I_1 \cos(\gamma)}{\Omega} \quad (6.14)$$

where Ω is the mechanical angular speed of the rotor. In case of minimum rotational speed, nominal current injected and $\gamma = 5^\circ$:

$$T = 0.188Nm \quad (6.15)$$

corresponding to a lack of 10% with respect to the rated torque.

Conclusions

In the first part, a literature review outlined the state of art concerning energy storage, together with the proposal of a new large scale kinetic energy storage (LSKES) configuration, which shows interesting cost savings and fosters the interest of deeper research in the subject.

On the latter part a new application of TFHSM is proposed and validated for the purpose of driving a magnetically suspended flywheel. An hybrid design approach that mixes 2D FEA analyses and analytical equations allowed to properly model flux leakages led by the presence of a permanent magnet, responsible for an important reduction in the flux reaching the air gap with respect to the one produced by the magnet. Deviations between the hybrid approach and 3D FEA validation models have been found to be lower than 15 % for most of the variables of interest.

An important limitation discovered consists of the presence of a cogging torque of high value (up to more than 20 times higher than the accelerating/decelerating torque), which poses concerns on machine start up and numerical FEA problems when dealing with accelerating/decelerating torque evaluation. This aspect is partially due to the expected high discharge time of the flywheel assumed, which implies a low power required from the armature winding, hence low accelerating/decelerating torque production. The presence of a cogging torque was foreseeable a priori, however it was not possible a detailed comparison with the armature torque until a detailed design is carried out.

Further work shall investigate ways to reduce the cogging torque: rotor track skewing, different stator layouts implying a higher number of poles (and therefore a reduced effect of curvature and a better utilization factor) or the introduction of a continuous, curved stator.

Moreover FEA outlined that low magnetic flux densities are present both in the stator and rotor track external edges. Savings of SMC material are therefore viable by mean of a rounded geometry, without affecting the magnetic performance significantly.

Losses calculation, particularly concerning the magnetic core, are not

simple to compute. It should be divided the share of eddy currents with respect to hysteresis losses, and a detailed description of the hysteresis cycle has to be introduced in order to keep into account the non symmetric behavior of homopolar machines.

Bibliography

- [1] P. Louka, G. Galanis, N. Siebert, G. Kariniotakis, P. Katsafados, I. Pytharoulis, G. Kallos, *Improvements in wind speed forecasts for wind power prediction purposes using Kalman filtering*, 2008
- [2] Nima Amjady, Farshid Keynia, Hamidreza Zareipour, *Short-term wind power forecasting using ridgelet neural network*, 2011
- [3] Changsong Chen, Shanxu Duan, Tao Cai, Bangyin Liu, *Online 24-h solar power forecasting based on weather type classification using artificial neural network*, 2011
- [4] Franco Bortot, *Variables identification in photovoltaic energy production forecast*, 2011
- [5] Benjamin K. Sovacool, *The intermittency of wind, solar, and renewable electricity generators: Technical barrier or rhetorical excuse?*, 2008
- [6] Brian Tarroja, Fabian Mueller, Joshua D. Eichman, Scott Samuelsen, *Metrics for evaluating the impacts of intermittent renewable generation on utility load-balancing*, 2012
- [7] Anna Stoppato, Alberto Benato, Alberto Mirandola, *Assessment of stresses and residual life of plant components in view of life-time extension of power plants*, 2012
- [8] ShIn-IchI Inage, *Prospects for Large-Scale Energy Storage in Decarbonised Power Grids*, IEA, 2011
- [9] Federico Santi, Davide Ghezzi, Romano Acri, *CAES: un'opzione per il bilanciamento delle rinnovabili e per le smart grid*, L'Energia Elettrica, gennaio/febbraio 2012
- [10] Luigi Mazzocchi, Massimo Meghella, Enrica Micolano, *Studi e sperimentazioni sulle tecnologie di accumulo elettrico*, L'Energia Elettrica, settembre/ottobre 2011

- [11] IEA, *Technology Roadmap: Hydropower*, 2012
- [12] Y. Suzuki, A. Koyanagi, M. Kobayashi, R. Shimada, *Novel applications of the flywheel energy storage system*, 2004
- [13] KEMA, *Cost Comparison for a 20 MW Flywheel-based Frequency Regulation Power Plant*, 2007
- [14] Giovanni Meneghetti, *Corso di Costruzioni Meccaniche*, Università degli Studi di Padova, 2010
- [15] S.M. Arnold, A.F. Saleeb, N.R. Al-Zoub, *Deformation and life analysis of composite flywheel disk systems*, 2002
- [16] Haichang Liu, Jihai Jiang, *Flywheel energy storage: An upswing technology for energy sustainability*, 2006
- [17] Björn Bolund, Hans Bernhoff, Mats Leijon, *Flywheel energy and power storage systems*, 2005
- [18] Giuseppe Buja, *Course of Electric Technologies for Vehicles*, Università degli Studi di Padova, 2012
- [19] Michael F. Ashby, *Materials Selection in Mechanical Design*, Elsevier, 2005
- [20] Tokyo Railway Technical Research Institute *Toward Sustainable Development of Railways*, 2012
- [21] I. Boldea, S.A. Nasar, *Linear Electric Motors*, Prentice Hall, 1987
- [22] W. Schuiscky, *Calcolo delle macchine Elettriche*, Casa editrice Ambrosiana, 1969
- [23] Beacon Power, *4th Generation Flywheels Datasheet*, 2012
- [24] Ryouichi Takahata, *Compact Flywheel Energy Storage System*, KOYO SEIKO CO. LTD, 2004
- [25] Sun Jinji, Ren Yuan, Fang Jiancheng, *Passive axial magnetic bearing with Halbach magnetized array in magnetically suspended control moment gyro application*, 2011
- [26] Lei Shi, Suyuan Yu, Guojun Yang, Zhengang Shi, YangXu, *Technical design and principle test of active magnetic bearings for the turbinecompressor of HTR-10GT*, 2011

- [27] W. H. Yeadon, A. W. Yeadon, *Handbook of Small Electric Motors*, McGraw Hill, 2001
- [28] J. F. Gieras, M. Wing, *Permanent Magnet Motor Technology*, CRC Press, 2002
- [29] Oliver Guteisch, Matthew A. Willard, Ekkes Brück, Christina H. Chen, S. G. Sankar, and J. Ping Liu, *Magnetic Materials and Devices for the 21st Century: Stronger, Lighter, and More Energy Efficient*, 2010
- [30] Bhim Singh, B. P. Singh, S. Dwivedi, *A State of Art on Different Configurations of Permanent Magnet Brushless Machines*, 2006
- [31] <http://www.stanfordmagnets.com/how-to-choose-permanent-magnet-materials.html>. Accessed 7/9/2013.
- [32] <http://www.mmcmagnetics.com/magdsgn/propcomp.htm>. Accessed 7/9/2013.
- [33] Marcello Zerbetto, *Analisi elettromagnetica di motore lineare omopolare*, Università degli Studi di Padova, 1999/2000
- [34] Piller, *Continuità del servizio elettrico ed efficienza energetica in utenze critiche*, Università Sapienza di Roma, 04/20/2009
- [35] IEA, *World Energy Outlook*, 2011
- [36] IEA-PVPS, *The Role of Energy Storage for Mini-Grid Stabilization*, 2011
- [37] Nicola Bianchi, *Calcolo delle macchine elettriche col metodo degli elementi finiti*, Cleup, 2001
- [38] G. E. Dawson, A.R. Eastham, R. Ong, *Computer-Aided Design Studies of the Homopolar Linear Synchronous Motor*, IEEE Transactions on Magnetics, Vol. MAG-20, No. 5, September 1984
- [39] M. J. Balchin, J. F. Eastham, *Characteristics of a heteropolar linear synchronous machine with passive secondary*, IEE Electric Power Applications, December 1979, Vol. 2, No. 6